Immiscible Liquid-Liquid Displacement in Microfluidic Channels: Effects of Wettability and Geometry

by

Hyundo Lee

B.S., Mechanical and Aerospace Engineering, Seoul National University, 2009
M.S., Mechanical Engineering, Massachusetts Institute of Technology, 2014

Submitted to the Department of Mechanical Engineering
in partial fulfillment of the requirements for the degree of

Doctor of Philosophy in Mechanical Engineering

at the

MASSACHUSETTS INSTITUTE OF TECHNOLOGY

September 2017

Author ..... Signature redacted
Department of Mechanical Engineering
August 14, 2017

Certified by ..... Signature redacted
Patrick S. Doyle
Robert T. Haslam (1911) Professor of Chemical Engineering
Thesis Supervisor

Certified by ..... Signature redacted .....
Rohit Karnik
Associate Professor of Mechanical Engineering
Chairman, Thesis Committee

Accepted by ..... Signature redacted
Rohan Abeyaratne
Chairman, Department Committee on Graduate Theses

Immiscible Liquid-Liquid Displacement in Microfluidic Channels: Effects of Wettability and Geometry

by

Hyundo Lee

Submitted to the Department of Mechanical Engineering
on August 25, 2017, in partial fulfillment of the
requirements for the degree of
Doctor of Philosophy in Mechanical Engineering

Abstract

Displacement of a fluid by an immiscible fluid occurs in various situations such as oil recovery in underground reservoirs, transport in the human body, and other interconnected network systems and porous media. We are motivated by oil recovery processes in geological porous media that take place at the micrometer scale, and focus in particular on the effects of wettability and geometry of microstructures on immiscible liquid-liquid displacements, that result from interactions in oil-water-rock systems.

Microfluidic devices, micromodels, have been proposed as experimental test beds for reproducing flows in oil reservoirs in laboratory environments since they offer fine control over geometry and chemistry, and therefore provide insights into their effects on the process. These microfluidic devices are usually two-dimensional and transparent, with a simplified porous network designed to visualize and study fluid behavior in porous media. In oil reservoir research, the microfluidic test beds reflect underground oil reservoir conditions, for example, porosity, permeability, and wettability.

The work in this thesis focuses on simple, additive micromodel fabrication techniques to build robust and reproducible structures in microfluidic channels and on the basic and fundamental understanding of immiscible displacement processes with simplified models and controlled flow conditions. We introduce two simple micromodel fabrication methods that can provide design flexibility with photopatterning, the ability to tailor wetting properties, and the calcium carbonate structure that is the most common constituent of oil reservoirs. We utilize a microscope projection

lithography to construct polymeric structures with pre-defined wetting properties using a UV-initiated copolymerization method, and we are also able to make real-rock carbonate micromodels by incorporating calcium carbonate seed particles into microstructures and growing them with a supersaturated calcium carbonate solution. Using the micromodel fabrication methods thus developed, we have systematically explored oil-water immiscible displacement processes in a controlled manner with respect to various geometric and wettability conditions. With the fact that our flow experiment is in a small capillary number regime, we formulate a mathematical model for the oil-water displacement process with photopatterned structures of simple geometry and periodic patterns, and verify our theoretical model by matching it with our experimental observations, and we also conduct oil recovery model studies with encapsulated oil pockets with aqueous surfactant solution flooding. Lastly, based on the experience of calcium carbonate/hydrogel composite structuring and calcium carbonate growth from the structure, we expand our work and develop a method of making drug-laden hydrogel particles.

By developing flexible methods to make microfluidic devices for immiscible fluids displacement study and investigation on the displacement process, we have been able to realize that microfluidic research with simplified conditions can enhance fundamental understanding of multiphase flow in natural, complex porous media.

Thesis Supervisor: Patrick S. Doyle
Title: Robert T. Haslam (1911) Professor of Chemical Engineering

Acknowledgments

First of all, I want to express my appreciation to Prof. Patrick Doyle for his kind advice during my PhD. I remember when I first joined the group, I was very naive at planning research and working on my idea. But, he advised me with patience, and I was able to improve my logical thinking process for doing research. Sometimes he gave me challenging problems, but at the same time he encouraged me, so I can focus on my research. I learned a lot from him and really enjoyed working with him. Thank you Prof. Doyle.

And I thank my thesis committee, Prof. Rohit Karnik, and Prof. Nicholas Fang. Through three times committee meetings with them, they guided my research work with careful consideration. They gave different perspectives on my research and that was very helpful for me, because sometimes I missed some important questions that I should not have missed. Thank you Prof. Karnik and Prof. Fang.

I think I was lucky to be a member of the Doyle group. Especially I thank the same year graduate students, Ankur and Jae Jung, for sharing research work and outside of work for 5 years together. All group members are very kind, warmhearted, and I thank for knowing and working with such nice people, and it was always great pleasure being here. I thank Ankur Gupta, Jae Jung Kim, Lynna Chen, Li-Chiun Cheng, Sarah Shapiro, Beatrice Soh, Max Nagarajan, Abu Zayed Md Badruddoza, Alex Klotz, Augusto Tentori, Pravien Parthiban, Doug Godfrin, Vivek Narsimhan, Gwen Wilcox, Seung Goo Lee, Jane Lee and former group members.

Other part of my life at MIT, I really had a great time with great friends. As everyone else, my life is always in between good and bad, and friends gave a lot of energy to me afterwork and I came back to work with that energy. I think getting to know these friends is another great part of my PhD and I think I was able to complete my PhD thanks to them. I thank Kyungsuk, Kitae, Taekeun, Keunwhan, Sungkwan, Hyunho, Byungjin, Jeonyoon, Youngsuk, Ahhyun, Yongchul, Minkyun, Jaehyun, Jinwon, friends of KGSAME and KSA soccer team.

For the last, I want to express my gratitude to my family with this chance. For me,

my family is the biggest part of my life, and they have been the greatest support to me as always. I thank my parents(Hongjun Lee and Sookyoung Kang), sister(Kyungmi Lee), brother-in-law(Hee Han), and my lovely nephew(Siheon Han) and nice(Siyoon Han).

Contents

List of Figures

List of Tables

Chapter 1

Introduction

According to estimates, a huge amount of oil and natural gas unrecoverable with current technology is still held in reservoirs, an amount corresponding to more than 200 years of the world's oil supply at current consumption rates, after conventional production methods are exhausted. Because of this, the petroleum industry is interested in better understanding of multiphase flow in oil reservoirs [2].

It is a common practice to use core samples from oil reservoir sites to understand oil-gas-water multiphase flow occurring in underground oil reservoirs [3–6]. However, the disadvantages of core-flooding experiments (e.g., opacity, site specificity, ambiguities of experimental parameters) have impeded fundamental investigations of oil reservoirs in the laboratory environment. Because of such limitations of core-flooding experiments, researchers have recently developed synthetic micromodels using microfabrication techniques. Micromodels are usually two-dimensional and transparent microchannels with a simplified porous network designed to visualize and study fluid behavior in porous media [7–11]. In oil reservoir research, micromodels reflect underground oil reservoir conditions, for example, porosity, permeability, and wettability [8, 11–13]. These reservoir properties are designed and built into micromodels for further understanding of fundamental fluid behavior and interactions among oil-water-rock phases. Micromodel studies in the laboratory environment are required for various field applications, such as operational practices for oil production, enhanced oil recovery with various materials (surfactant [14–16], polymer [17–19], foam [20,21],

steam [22]), and reservoir network mapping [23].

Previous microfluidic research has broadened our understanding of multi-phase flow in porous media and has provided solutions for practical engineering issues by visualizing phenomena occurring in subsurface oil reservoirs. However, most previous studies have not incorporated the above factors that affect multi-phase flow behavior, yet have analyzed the statistics of transport on a global scale, for example, getting input-output relationships (e.g., input pressure vs. saturated level of oil after flooding). As a result, multi-phase flow mechanisms at the pore scale are still not clearly explainable. From this perspective we thought it is more desirable to start with a micromodel that has simple and prescribed structures rather than injecting immiscible fluids into a black-box micromodel that has complex geometries and undefined wettability, and as a result there was lack of local constitutive understanding that can be generalized for a global system.

In this thesis, we introduce two microfluidic test bed fabrication methods in Chapter 2 and Chapter 5, and we investigate and analyze liquid compartmentalization after liquid-liquid displacement and propose theoretical models to explain the displacement process in Chapter 3 and Chapter 4. We believe that understanding of interaction between the fluids and the patterned structures can provide physical insights into the oil/water displacement and enhanced oil recovery processes. We further explore making drug/hydrogel composite particles in Chapter 6 based on our experience with calcium carbonate/hydrogel composite structures for mimicking the carbonate oil reservoir environment. This thesis combines five published papers, and the following chapters are based on each of the papers.

1.1 Single-step Ultraviolet Lithography Process for Microstructuring and Wettability Control

In Chapter 2, we present a new method to fabricate reservoir micromodels with controlled wetting properties. Photopatterned, copolymerized polymeric microstructures

are fabricated in a bottom-up manner in microchannels. The use of rationally designed copolymers allows us to tailor the wetting behavior (hydrophilic/oleophilic) of the structures without requiring additional surface modifications. Using this approach, two separate techniques of constructing microstructures and tailoring their wetting behavior are combined in a simple, single-step ultraviolet lithography process. This microstructuring method is fast, economical, and versatile compared with previous fabrication methods used for multi-phase micromodel experiments. The wetting behaviors of the copolymerized microstructures are quantified, and demonstrative oil/water immiscible displacement experiments are conducted. Most of Chapter 2 is published as Lee, H., Lee, S.G., and Doyle, P.S. "Photopatterned oil- reservoir micromodels with tailored wetting properties," Lab Chip, 15, 3047-3055, 2015.

1.2 Understand the Immiscible Oil/Water Displacement as the Interface Passing Obstacles in Microchannels

In Chapter 3, we present a simple geometric model to understand the oil/water liquid-liquid displacement process around an obstacle in a microchannel, and predict the evolution of the water/oil interface over an obstacle as its wettability and geometry are varied. The compartmentalization of liquids within small channels using microstructures has been a topic of much interest to microfluidics starting from the studies of droplet-based microfluidics in the early 2000s. We use shape and wettability as variables to compartmentalize small oil or water pockets in arrays within microfluidic channels, and also demonstrate other more exotic trapping modes, such as bridge trapping across two posts. The experiments are supported by a simple, minimal model based on static, geometric considerations that captures the essential physics, and which is well justified given the low capillary numbers used. The approach is applicable to a diverse array of applications, mainly it enables model geometries for porous reservoirs to be studied for enhanced oil/gas recovery applications. Most of

Chapter 3 is published as Lee, H., Gupta, A., Hatton, T.A. and Doyle, P.S. "Creating Isolated Liquid Compartments Using Photopatterned Obstacles in Microfluidics," Physical Review Applied, 7(4), p.044013, 2017.

1.3 Controlled Parallel Liquid Compartments with Periodic Patterns using Liquid-Liquid Displacement

In Chapter 4, we study the process of oil displacement upon sequential injection of water over a photopatterned periodic structure in a confined geometry of microchannels. By varying the amplitude and frequency of triangular and sinusoidal patterns, we are able to completely remove oil or trap oil in varying amounts. We present a theoretical model based on geometrical arguments that successfully predicts the criterion for liquid entrapment and provides insights into the parameters that govern the physical process. Using the periodic patterns and the captured oil compartments with the patterns, we also demonstrate the enhanced oil recovery process and have analysis of the process. Most of Chapter 4 is based on Gupta, A., Lee, H. and Doyle, P.S. "Controlled Liquid Entrapment over Patterned Sidewalls in Confined Geometries" (submitted).

1.4 Site-Selective In Situ Grown Calcium Carbonate Micromodels with Tunable Geometry, Porosity, and Wettability

In Chapter 5, we introduce a simple method to create calcium carbonate ($CaCO_3$) micromodels composed of in situ grown $CaCO_3$ to replicate the length scales and geochemistry of carbonate oil reservoir condition. $CaCO_3$ nanoparticles/polymer composite microstructures are built in microfluidic channels by photopatterning, and

$CaCO_3$ nanoparticles are selectively grown in situ from these microstructures by supplying Ca^{2+}, CO_3^{2-} ions rich, supersaturated solutions. This approach enables us to fabricate synthetic $CaCO_3$ reservoir micromodels having dynamically tunable geometries with submicrometer pore length scales and controlled wettability. Using this new method, we demonstrate an immiscible fluids displacement process and acid stimulation process to visualize pore-scale fluid-carbonate interactions in real time that is frequently used in oil production sites to increase the permeability of the oil reservoirs. Most of Chapter 5 is published as Lee, S.G., Lee, H., Gupta, A., Chang, S. and Doyle, P.S. "Site-Selective In Situ Grown Calcium Carbonate Micromodels with Tunable Geometry, Porosity, and Wettability," Advanced Functional Materials, 26(27), pp.4896-4905, 2016.

1.5 Micelle-laden Hydrogels as Templates and Delivery Vehicles for Nanocrystals of Hydrophobic Drugs

In Chapter 6, based on our research experience with hydrogel/$CaCO_3$ composite structures introduced in the previous chapter, we extend our study to the pharmaceutical research area of nanocrystal drug formation in hydrogel particles. Having drugs in nanocrystalline size has many benefits, and a proper way to delivery the nanocrystallized drugs into the human body is important. In this work, we introduce our new method to synthesize hydrophobic drugs in hydrogel particles. We use biocompatible hydro- gels as both templates for nanocrystal synthesis and carriers for stable drug delivery. We also incorporate acrylated-surfactants into the hydrogel matrix, and we are able to make drugs of even smaller size. Most of Chapter 6 is based on Godfrin, D.P., Lee, H. and Doyle, P.S. "Micelle laden hydrogels as templates and delivery vehicles for nanocrystals of hydrophobic drugs" (in preparation).

Chapter 2

Photo-patterning Polymeric Structures in Microchannels with Tailored Wettability

2.1 Microstructuring – Microscope Projection Lithography

Various fabrication techniques have been employed to build microfluidic devices [9,24], including plasma etching of silicon [25], deep reactive ion etching of glass [26,27], and soft lithography with polymeric materials [21, 28–36]. These fabrication methods are often time consuming and involve access to cleanroom microfabrication facilities which can result in high unit costs for a single microfluidic test bed. Moreover, once the design of features or patterns are fabricated, it is nearly impossible to make geometric modifications on-the-fly and quickly iterate on designs. In this chapter, we introduce a simple and rapid microstructuring method that can be applicable for various microfluidic experiment studies.

2.1.1 Free Radical Photopolymerization

Free radical photopolymerization is a successive cross-linking process of free radicals and monomer molecules initiated by ultraviolet irradiation. When a homogeneous mixture of monomers, photoinitiator, and additional functional chemicals is exposed to ultraviolet radiation for a few millisecond or seconds, free radicals are generated by photolysis of light-sensitive photoinitiator molecules. UV radiation cleaves a bond of a photoinitiator molecule, generating highly reactive free radials. The free radicals created from the initiating molecules transfer to the monomer units, attack double bond groups in monomer molecules, convert monomer molecules to a polymer. Monomer molecules are successively added to these cross-linking chains, and solid networks of polymers are created. This photopolymerization process is terminated if two free radicals join together, a hydrogen atom from one end is abstracted to another, or a radical abstracts a hydrogen atom from a neighboring molecule.

Photopolymerization is simple, rapid and versatile than other polymerization processes, and the application of free radical photopolymerization process can be controlled by exposure time, intensity of ultraviolet light, concentration of photoinitiator, and selective exposure by using an impenetrable layer.

2.1.2 Stop-Flow-Lithography Technique

In this work, we utilized the Stop-Flow-Lithography(SFL) technique that has been developed in the Doyle Group, MIT [37–39]. SFL uses the free radical photopolymerzation with microscope projection lithography. It introduces streams of precursor with a controlled-pressure pump, holds the flow, irradiates UV to induce free radical photopolymerization with specific geometrical features through pre-defined transparent masks, and finally releases microparticles with supplying pressure again. This stop-polymerization-flow sequence is repeated and SFL produces high-resolution microparticles at high-throughput. Instead of producing functional microparticles, we utilize this photo-patterning technique to build polymeric structures in initially blank microchannels.

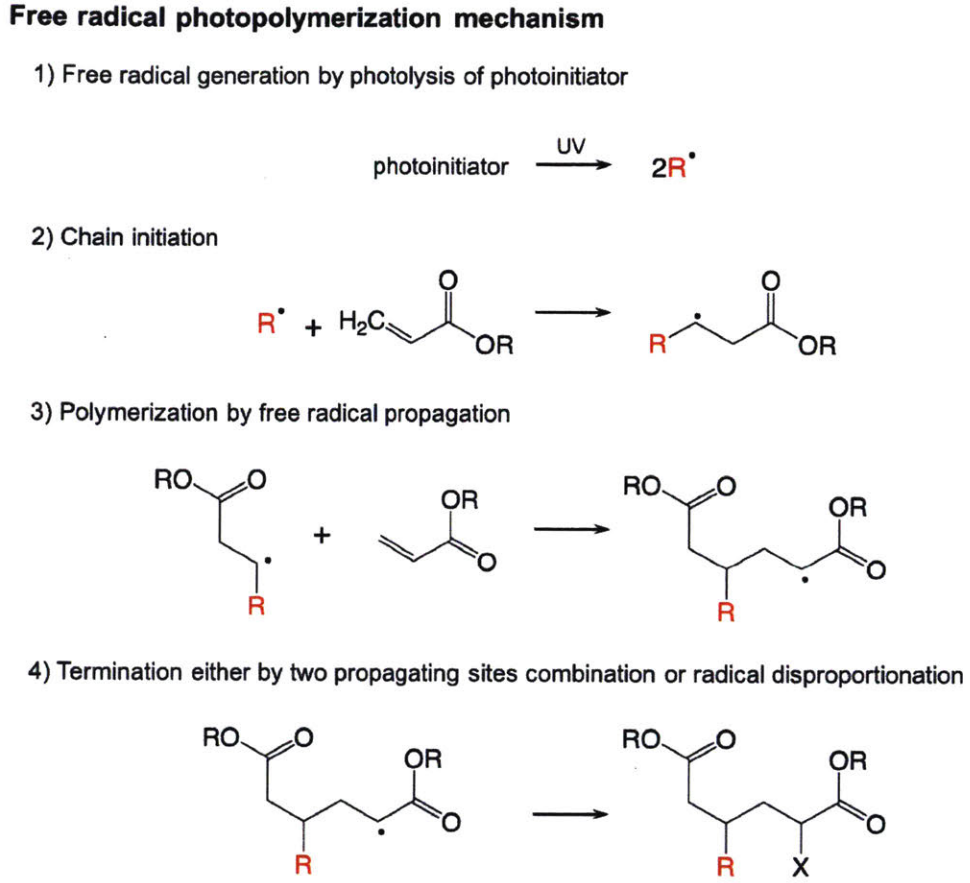

Figure 2-1: Mechanism of free radical polymerization.

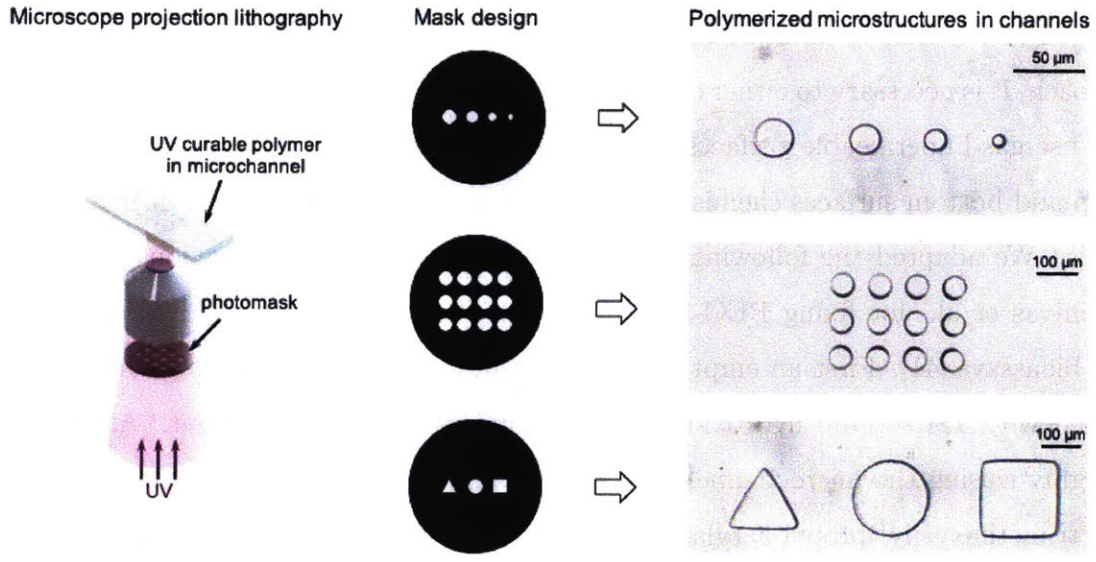

Figure 2-2: Schematic showing the concept of microscope projection lithography.

2.1.3 Polymer Structure Fixation with Surface Acrylation in Glass Microchannels

The only difference between the polymerization process of the previous Stop-Flow-Lithography and the process of the building fixed structures is whether polymerized particles are floating particles, or fixed structures in microchannels. During the SFL process, polymerized particles are not bound to the top and bottom surfaces due to the oxygen permeability of PDMS(Polydimethylsiloxane) (Fig.2-3). A thin oxygen layer prevents the polymerization of precursor solutions near top and bottom surfaces by forming inhibition layers [40].

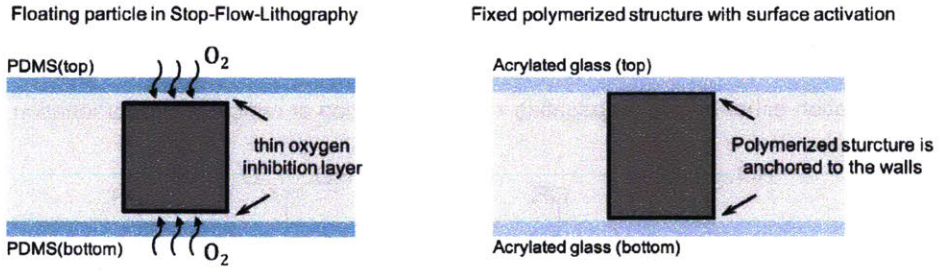

Figure 2-3: Side view of the polymerization process in an oxygen permeable PDMS channel and in a surface activated glass channel for comparison.

Since we want to build desired structures in microchannels with a bottom-up approach, it is necessary to either control the oxygen environment during polymerization or use gas-impermeable surfaces; we chose the latter. It is also necessary to modify top and bottom surfaces chemistry to hold the polymerized structures in microchannels. We adapted the following surface activation procedure as previously done by Srinivas et al. for fixing PEG-DA (poly(ethylene glycol)diacrylate) hydrogel posts in bioassays [41]. First an empty glass microfluidic channel (Hilgenberg GmbH) was filled with 1M sodium hydroxide (NaOH) aqueous solution for 1 hour. After thoroughly rinsing the microchannel with ethanol and water, the channel was filled with 3-(trimethoxysilyl)propyl acrylate (Sigma-Aldrich) for 5 minutes.

The microchannel was thoroughly rinsed with ethanol and water again, and cured at 80 °C for 15 minutes for sufficient reaction. Later, when ultraviolet polymerization

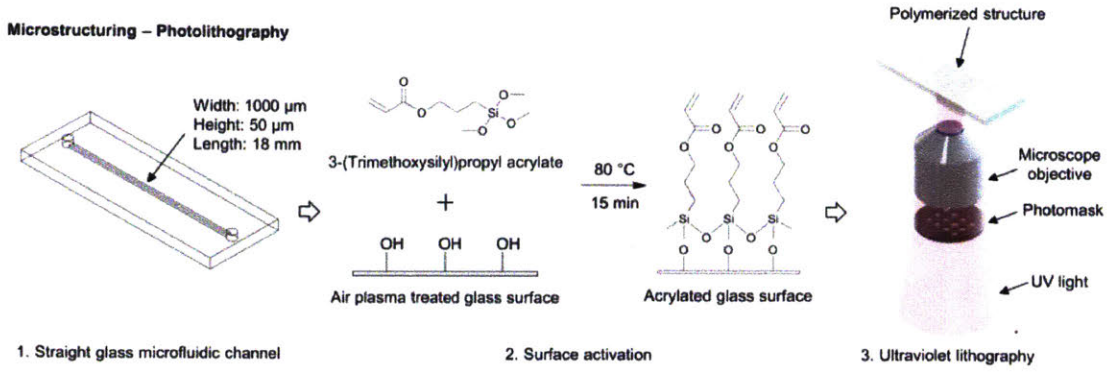

Figure 2-4: Schematic showing the photolithography process. Surfaces of an initially empty microchannel are activated with 3-(trimethoxysilyl)propyl acrylate for fixing polymerized structures, and then the channel is filled with a UV-curable precursor solution. A microstructure is synthesized with photomask-defined geometry by UV exposure. The uncured precursor solution is removed by flushing with acetone. Reprinted with permission from Hyundo Lee, Seung Goo Lee and Patrick S. Doyle. "Photopatterned oil-reservoir micromodels with tailored wetting properties." Lab Chip 15 (2015): 3047. Copyright The Royal Society of Chemistry 2015.

reaction occurred, the top and bottom glass surfaces modified with acrylate functional group promoted polymer structure fixation on the surfaces. When the glass microchannel acrylation is done, with proper ratios of crosslinkers, monomers, and a photoinitiator, hydrophilic and oleophilic structures were built in the microchannel. A thoroughly mixed precursor solution was injected into the activated glass microchannel and UV-polymerization was done on the stage of an inverted microscope (Zeiss Axio Observer A1). A photomask of desired geometric shape was inserted into the field stop of the microscope, and the microchannel was then placed and aligned properly. UV exposure time was controlled by switching a LED light source on and off with LabView. After building microstructures, any uncured precursor solution was washed out of the device with acetone (Fig.2-4).

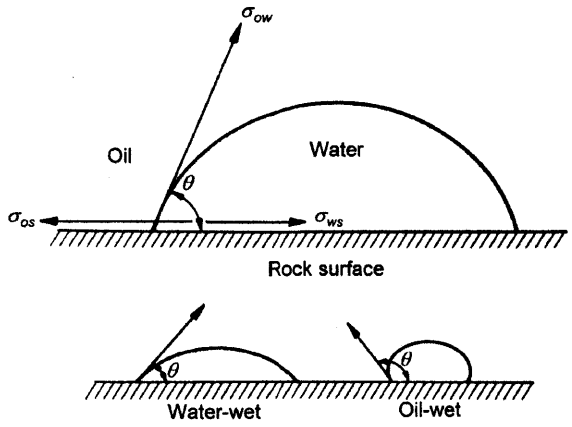

Figure 2-5: Young's equation for wettability, water-wet and oil-wet surfaces. [1]

2.2 Tailoring Wettability of Microstructures – Hydrophilic/Oleophilic Monomer Copolymerization

2.2.1 Wettability

Wettability describes a relationship between liquids and solid surface and explains the spreading preference of liquids on solid surfaces. For the same amount of liquid, the more a liquid drop tends to spread out on a surface, the more liquid and solid molecules like each other and we consider that the wettability of the liquid on the solid surface is good. The wettability is conventionally measured by contact angle. This contact angle is formed by the balance of adhesion force; force between liquid and solid surface and cohesion force; the intermolecular force of liquid and this force balance is expressed by Young's equation.

$$\gamma_{os} - \gamma_{ws} = \gamma_{wo} \cos\theta_{wo} \tag{2.1}$$

where,

γ_{os} = the interfacial tension between the oil and solid phases,

γ_{ws} = the interfacial tension between the water and solid phases,

γ_{wo} = the interfacial tension between the oil and water

At pore level fluid displacements in oil reservoir, oil interacts with other phases,

gas, brine, or water with surfactant. When this displacement phenomena occurs in porous oil reservoir, wettability and geometrical feature are important factors have to be considered.

In this study, we are interested in oil-water flows around geometrical structures with a tuned wetting property. Most prior researches only investigated the wettability of micromodels in solid-liquid-air systems, hydro-philicity/phobicity in air or oleo-philicity/phobicity in air.

However, as mentioned above, since the wettability is a relative preference of a solid surface, we need to define wetting property of oil-wet(oleophilic) and water-wet(hydrophilic) depends on the configuration of water contact angle in oil. In other words, both hydrophilic and hydrophobic surfaces might be oleophilic (or oleophobic) in water [42], it is necessary to investigate the micromodel's wetting preference in the presence of both water and oil.

There is no clear boundary for distinction of water-wet, intermediate-wet, or oil-wet. However, generally a surface is considered water-wet when a water contact angle in oil phase is less than 75°, intermediate-wet when the contact angle is 75° $\sim$ 105°, and oil-wet when the contact angle is greater than 105°.

The water contact angle in oil can be also described by the relationship between water contact angle in air (hydrophilic/hydrophobic) and oil contact angle in air (oleophilic/oleophobic) as Jung et al. derived below equation [42] (eqn. 2.2).

$$cos\theta_{wo} = \frac{\gamma_{wa}cos\theta_{wa} - \gamma_{oa}cos\theta_{oa}}{\gamma_{wo}} \tag{2.2}$$

where,

$cos\theta_{wo}$ = water contact angle in oil,

$cos\theta_{wa}$ = water contact angle in air,

$cos\theta_{oa}$ = oil contact angle in air,

γ_{wa} = the surface tension of water,

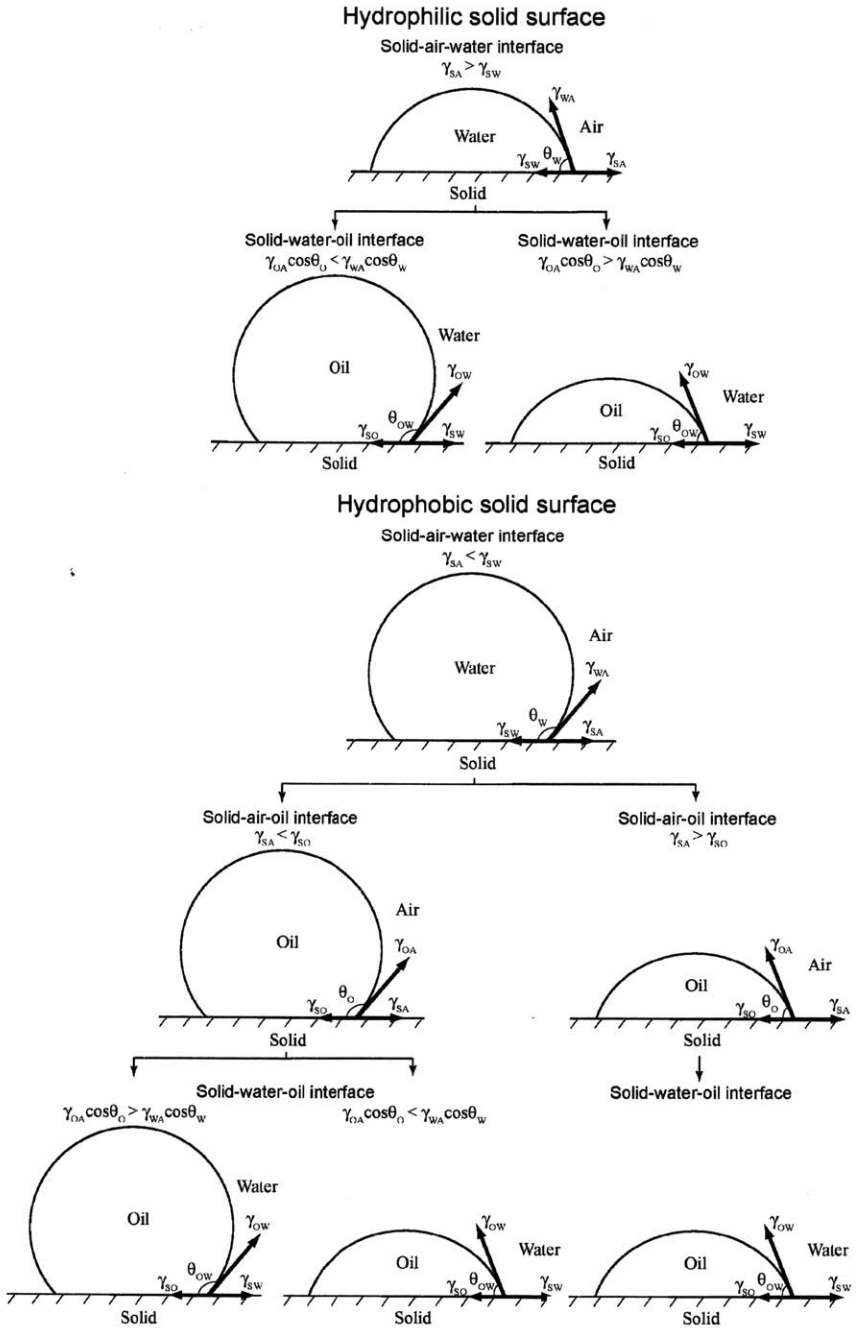

Figure 2-6: The relationship between water contact angle in air, oil contact angle in air, and oil contact angle in water describing hydro-philicity/phobicity and oleo-philicity/phobicity. Reprinted with permission from Jung, Yong Chae, and Bharat Bhushan. "Wetting behavior of water and oil droplets in three-phase interfaces for hydro-phobicity/philicity and oleo-phobicity/philicity." Langmuir 25.24 (2009): 14165-14173. Copyright (2009) American Chemical Society.

γ_{oa} = the surface tension of oil,

γ_{wo} = the interfacial tension between the oil and water

Because we are mainly interested in a water-oil liquid-liquid displacement in microchannels and the effect of the relative preference of the solid wall between water and oil, we measure and characterize water contact angle in oil for substrates rather than measuring oil contact angle in air and water contact angle in air separately.

2.2.2 Limitation of Wettability Control in Previous Micromodels

It is common practice to use core samples from oil reservoir sites to understand oil–gas–water multiphase flow occurring in underground oil reservoirs [43–49]. However, the disadvantages of core-flooding experiments (e.g. opacity, site specificity, ambiguities of experimental parameters) have impeded fundamental investigations of oil reservoirs in the laboratory environment. Due to such limitations of core-flooding experiments, researchers have recently developed synthetic micromodels using microfabrication techniques. Micromodels are usually two-dimensional and transparent microchannels with a simplified porous network designed to visualize and study fluid behavior in porous media [9, 24, 50]. In oil reservoir research, micromodels reflect underground oil reservoir conditions, for example, porosity, permeability, and wettability [51–54]. These reservoir properties are designed and built into micromodels for further understanding of fundamental fluid behavior and interactions among oil–water–rock phases. Micromodel studies in the laboratory environment are required for various real field applications, such as operational practices for oil production, enhanced oil recovery with various materials (surfactant [55], polymer [19], foam [21,56], steam [22]), and reservoir network mapping [23].

It is estimated that more than 60% of the world's oil and 40% of the world's gas reserves are held in carbonate reservoirs. For example, the Middle East is dominated by carbonate rocks, with around 70% of oil and 90% of gas reserves held within these reservoirs. When it comes to carbonate reservoirs, even though their main

component, calcite, inherently shows water-wet behavior, the surface wetting property of carbonate oil reservoir rocks is known to be mostly oil-wet [57]. Treiber et al. investigated 50 samples and showed that only 8% of the carbonate reservoir rocks were water-wet, 8% intermediate-wet, and 84% oil-wet [58]. That being said, the pertinent wetting properties of micromodels were not measured or controlled in previous studies. Most prior research only investigated the wettability of microfluidic test beds in solid-liquid-air systems, hydro-philicity/phobicity in air or oleo-philicity/phobicity in air. Since both hydrophilic and hydrophobic surfaces might be oleophilic (or oleophobic) in water [42], it is necessary to investigate the wetting preference of microfluidic test beds in the presence of both water and oil [42, 59, 60].

There have been significant advances in methods to modify wetting properties within microchannels for various applications including patterning hydrophilic regions for bioengineering applications, mimicking an oil reservoir's heterogeneous wetting features. These approaches include silanization [61], UV-ozone treatment [21,62], and UV-initiated polymer grafting [30,63]. However, these approaches to tune wettability also have some limitations. They all require additional post processing of a device. Furthermore it is well known that an UV-ozone treated PDMS (polydimethylsiloxane) surface recovers its native hydrophobicity by the oligomer migration from the bulk PDMS to the surface [64, 65]. Moreover, due to the lack of ability to tune wetting over a continuous range, it is hard to reproduce the complex wetting properties of an oil reservoir having locally different and more than two surface properties.

2.2.3 UV-initiated Copolymerization for Tailoring Wetting Preference of Photo-patterned Structures

Our approach to tailoring the wetting property of polymeric structures is through tuning the ratio of hydrophilic and oleophilic components. Here, we use polymeric crosslinkers that have reactive vinyl groups, which can polymerize with photoinitiator, 2-hydroxy-2-methylpropiophenon (Darocur 1173, Sigma-Aldrich), upon exposure to the ultraviolet light. We choose hydrophilic and oleophilic crosslinking agents,

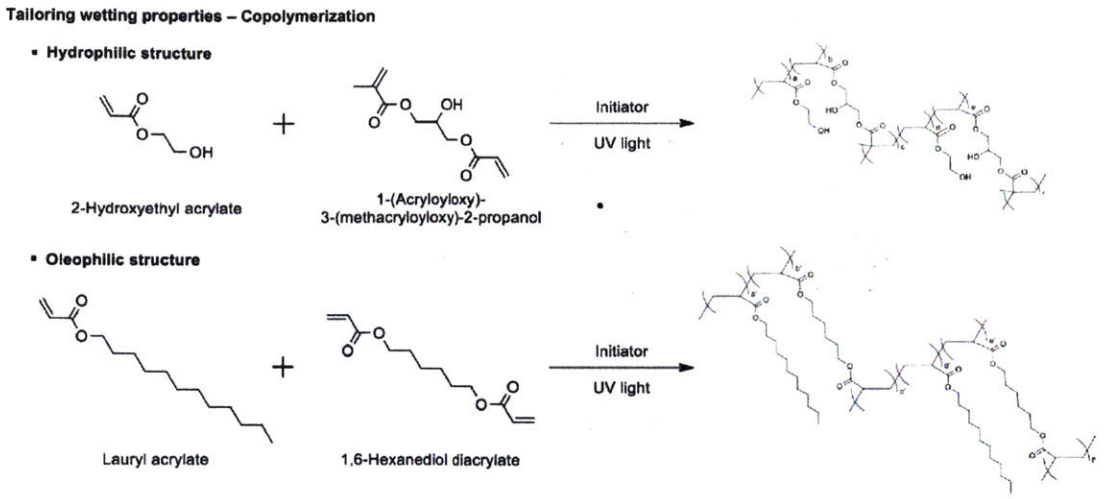

Figure 2-7: Hydrophilic and oleophilic microstructures are designed and built by UV-initiated copolymerization. The degree of hydrophilicity and oleophilicity is tailored by adjusting the composition of crosslinker and monomer. 3-(acryloyloxy)-2-hydroxypropyl methacrylate (AHM) and 1,6-hexanediol diacrylate (HDDA) are used as crosslinkers, and 2-hydroxyethyl acrylate (HEA) and lauryl acrylate (LA) are used as additive monomers for hydrophilic and oleophilic structures, respectively. Precursor solutions have the same concentration of photoinitiator, Darocur 1173 (2-hydroxy-2-methylpropiophenon). Reprinted with permission from Hyundo Lee, Seung Goo Lee and Patrick S. Doyle. "Photopatterned oil-reservoir micromodels with tailored wetting properties." Lab Chip 15 (2015): 3047. Copyright The Royal Society of Chemistry 2015.

1-(acryloyloxy)-3-(methacryloyloxy)-2-propanol (AMP) (Polysciences, Inc.) and 1,6-hexanediol diacrylate (HDDA) (Sigma-Aldrich), respectively, that can confer chemical and physical robustness. The desired wetting property is further increased by copolymerization with additives, hydrophilic and oleophilic monomers, 2-hydroxyethyl acrylate (HEA) (Sigma-Aldrich) and lauryl acrylate (LA) (Sigma-Aldrich) (Fig. 2-7, Table 2.1).

Polymeric substrates were prepared with precursor solutions of tabulated concentrations, cured under the UV lamp (wavelength 365 nm) for 3 minutes, and thoroughly rinsed with acetone to remove any uncured precursor (Fig.2-8-B). A quartz container filled with decane (Sigma-Aldrich) was located on the measurement stage of the contact angle goniometer (ramè-hart). The prepared substrate was immersed in the decane-filled quartz container, and the needle was set on the above of the substrate

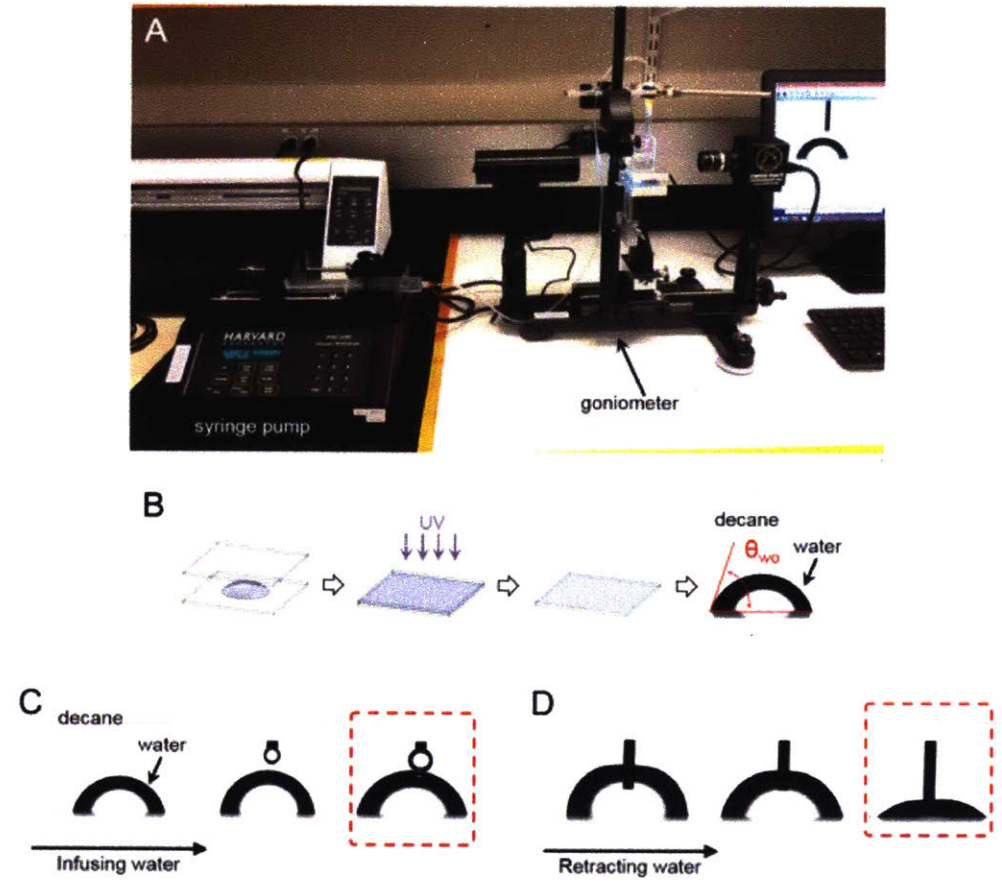

Figure 2-8: (A) Contact angle measurement setup with a syringe pump (Harvard Apparatus) and a goniometer (ramè-hart). (B) Substrates were prepared by pressing a drop of the precursor solution on acrylated glasses. (C) Advancing contact angles were measured when the droplet showed constant contact angle while the volume and the diameter of the droplet is increasing. (D) Receding contact angles were measured when the movement of the contact line was detected. Infusing/retracting rates were 5 ml/hr, and the maximum volume of the droplet was 20 μl. Reprinted with permission from Hyundo Lee, Seung Goo Lee and Patrick S. Doyle. "Photopatterned oil-reservoir micromodels with tailored wetting properties." Lab Chip 15 (2015): 3047. Copyright The Royal Society of Chemistry 2015.

Table 2.1: Chemical compositions of the copolymerized hydrophilic and oleophilic structures (v/v%).

Hydrophilic						Oleophilic					
	H-1	H-2	H-3	H-4	H-5		O-1	O-2	O-3	O-4	O-5
1-(Acryloyloxy)-3-(methacryloyloxy) -2-propanol	15%	35%	55%	75%	95%	1,6-Hexanediol diacrylate	15%	35%	55%	75%	95%
2-Hydroxyethyl acrylate	80%	60%	40%	20%	0	Lauryl acrylate	80%	60%	40%	20%	0
Darocur 1173	5%	5%	5%	5%	5%	Darocur 1173	5%	5%	5%	5%	5%

surface. Water was infused and withdrawn at a constant injecting/retracting rate (5 ml/hr) by a syringe pump (Harvard Apparatus), and the maximum volume of the droplet was 20 μl. The advancing and receding contact angles were measured with an image software (DROPimage Advanced, ramè-hart) when there was an evident contact line change, advanced or retreated, approximately 1 minute after infusion or withdrawal of water was stopped.

Fig.2-9 shows the trend of water contact angles in decane with respect to crosslinker-monomer volume-volume percent concentration of hydrophilic and oleophilic precursors (Table 2.1). We modulated the wetting properties of substrates from hydrophilic to oleophilic in a continuous range ($\theta_{adv_{water\ in\ oil}}$ from 60° to 144°) by tuning the ratio of components. As the portion of the hydrophilic or oleophilic additive (HEA or LA) increased, the hydroxyl or hydrocarbon of content of the polymer surfaces showed stronger interactions with polar (water) and nonpolar (decane) phases, that decreased and increased the water contact angle, respectively.

As the ratio of hydrophilic or oleophilic functionalities increase, contact angle hysteresis, the difference between advancing and receding contact angles, is also increased (H-5→H-1, O-5→O-1). This contact angle hysteresis increase is most likely due to the change of crosslinking density, as mentioned in as previous studies that investigated contact angles on polymer surfaces [66-68]. Less crosslinked polymeric surfaces are facile to rearrange their chemical structure upon the wetting of solvent, and thus allow the solvent penetration. However, highly crosslinked surfaces inhibit this restructuring by constrained chain mobility, and the solvent is unable to penetrate. As a result, the surfaces of lower crosslinking density have the larger difference

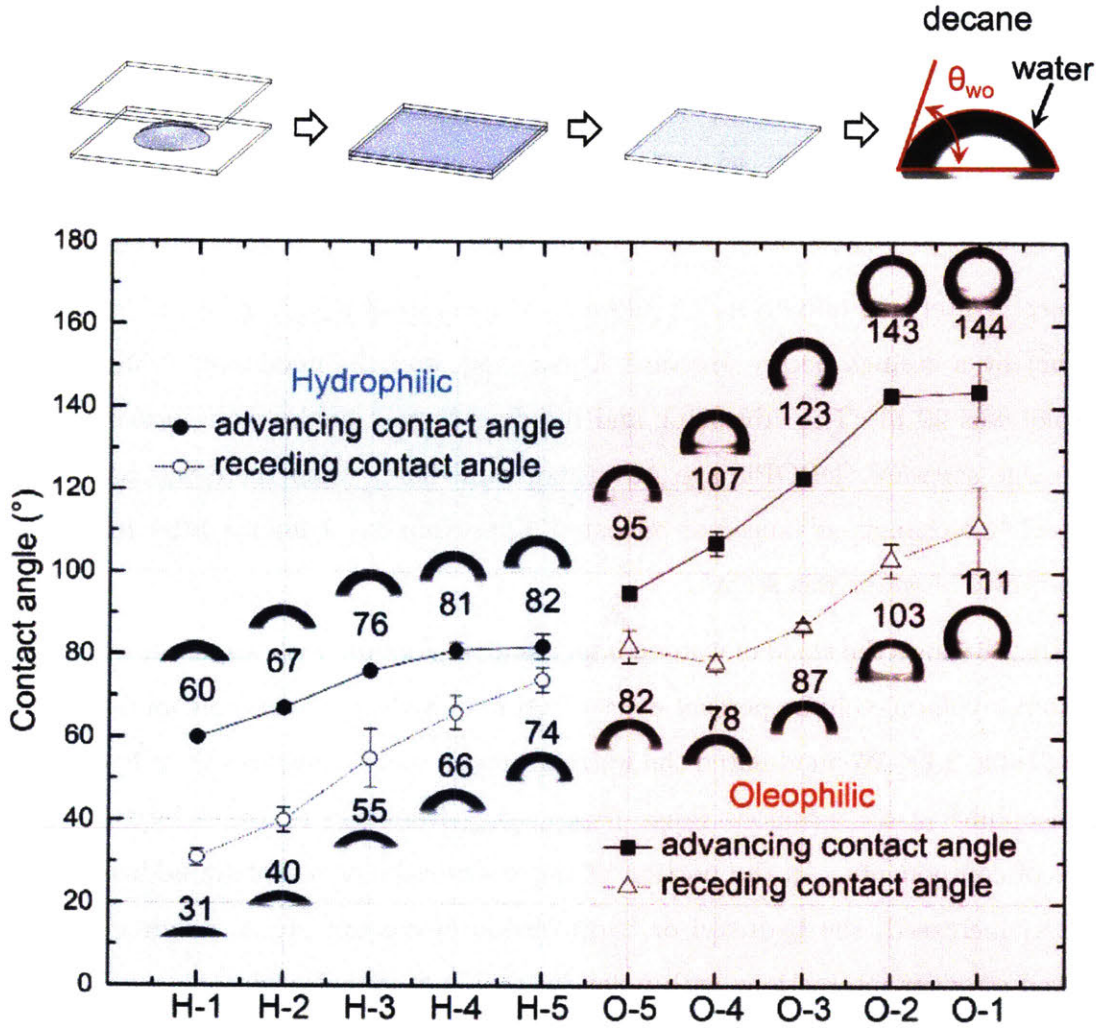

Figure 2-9: Water contact angles in decane. Hydrophilic (H–1-5) and oleophilic (O–1-5) substrates with controlled composition are prepared, and the substrates are immersed in decane to measure advancing and receding water contact angles. As the ratio of hydrophilic and oleophilic additive monomers in precursor solution increases, hydrophilicity and oleophilicity increases (H–5→H–1 and O–5→O–1), and the contact angle hysteresis increases as well due to the decrease in crosslinking density. Water contact angles in decane on pure glass ($\theta_{adv} = 19°$, $\theta_{rec} = 0°$) and acrylate treated glass ($\theta_{adv} = 58°$, $\theta_{rec} = 35°$) are also measured for reference. Reprinted with permission from Hyundo Lee, Seung Goo Lee and Patrick S. Doyle. "Photopatterned oil-reservoir micromodels with tailored wetting properties." Lab Chip 15 (2015): 3047. Copyright The Royal Society of Chemistry 2015.

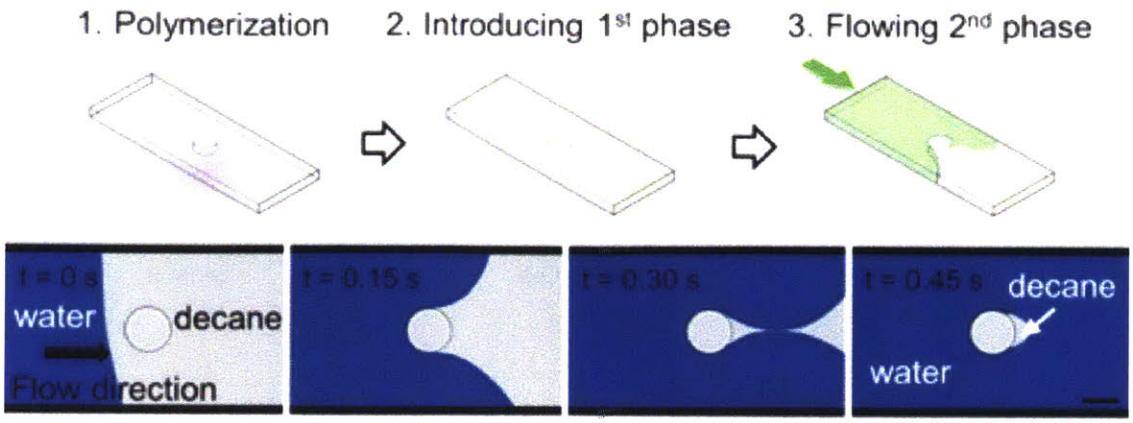

Figure 2-10: Single post oil-water displacement experiments. After building a single post in a microchannel and rinsing the channel with acetone to remove any uncured precursor solution, two immiscible fluids, water and oil, are serially introduced into the channel (decane followed by water). Scale bar is 100 μm. Reprinted with permission from Hyundo Lee, Seung Goo Lee and Patrick S. Doyle. "Photopatterned oil-reservoir micromodels with tailored wetting properties." Lab Chip 15 (2015): 3047. Copyright The Royal Society of Chemistry 2015.

of the surface energy for the polar and nonpolar solvents wetting, consequently show higher contact angle hysteresis [67].

2.3 Oil and Water Immiscible Liquid-Liquid Displacement with Cylindrical Posts of Different Wetting Properties

After polymerization of microstructures in empty microchannels and thoroughly rinsing uncured precursor solutions with acetone, subsequent flow experiments were conducted. The micromodel was then filled with decane, and water displaced decane under constant applied pressure (Fig.2-10, 2-11–A). Experiments with a reversed flow sequence were also performed (Fig. 2-11–B). Since the oleophilic posts (O–1, O–5) prefer oil to water, the oleophilic post formed a thin oil layer between the posts and water. The most oleophilic post (O–1) was eventually encapsulated by oil in

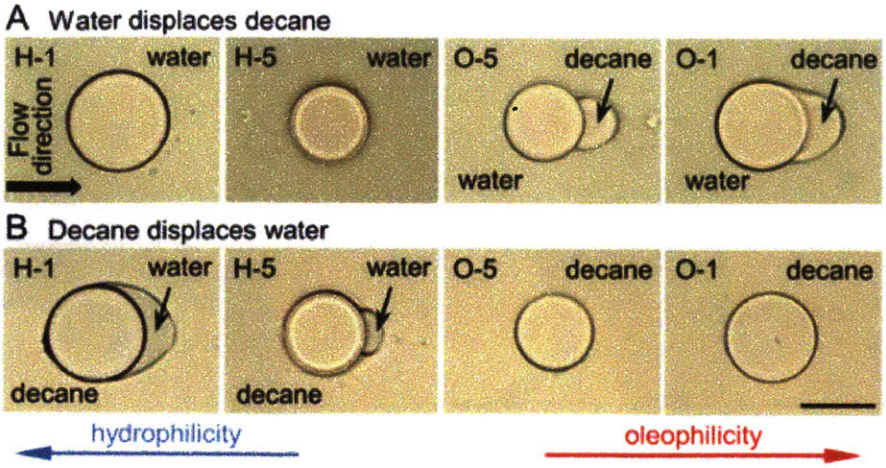

Figure 2-11: Water→oil displacement and oil→water displacement. (A) Microchannels are first filled with decane, and then water is introduced into the channels (flow direction from the left to the right). The alphanumeric code refers to the copolymer compositions listed in Table 1, H-1 being the most hydropholic and O-1 the most oleophilic.Water can completely displace decane for the hydropholic post systems (H-1, H-5), while decane remains entrained by the oleophlic posts (O–5, O–1). The most oleophilic post (O–1) is completely encapsulated by decane, while the less oleophilic post (O–5) has a well-defined droplet adhered to the downstream side. (B) Flow sequence is reversed relative to (A): the channels are filled with water, and then water is displaced by decane. Similar to the previous displacement, the most hydrophilic post (H–1) is entirely surrounded by water, H–5 is partially covered with water, and no water reamain around the oleophilic posts. Scale bar is 100 μm. Reprinted with permission from Hyundo Lee, Seung Goo Lee and Patrick S. Doyle. "Photopatterned oil-reservoir micromodels with tailored wetting properties." Lab Chip 15 (2015): 3047. Copyright The Royal Society of Chemistry 2015.

the case of oil→water flow, while the hydrophilic posts (H–1, H–5) left water at the posterior area in the case of water→oil flow. In the opposite flow sequence for each post, water/oil was repelled by oleophilic/hydrophilic posts since the posts prefer the displacing phase to displaced phase.

Based on these initial experiment sets, we can construct a set of eight possible experimental combinations: four posts of different wetting preferences and two flow sequences (oil→water, water→oil) (Fig.2-11). These eight combinations can be used to represent typical underground reservoir scenarios: the drainage process (when a non-wetting entering fluid displaces a wetting fluid) and the imbibition process (when a wetting fluid displaces a non-wetting fluid).

Four posts in Fig. 2-11 are photopatterned with the same photomask, thus right after polymerization all four posts have the same diameters. However, there are slight size changes at different solvent conditions. There is no significant size changes with homogeneous hydrophilic (H–5, AMP 95%, photoinitiator 5%) and oleophilic (O–5, HDDA 95%, photoinitiator 5%) posts. On the other hand, the most hydrophilic (H–1, AMP 15%, HEA 80%, photoinitiator 5%) and oleophilic (O–1, HDDA 15%, LA 80%, photoinitiator 5%) posts show different sizes at different solvent conditions (acetone, water, and decane). This different swelling behavior can be explained with the same reason of previous contact angle hysteresis trend, the crosslinking density and the affinity of hydrophilic/oleophilic posts for polar/nonpolar solvents [67–71]. In comparison with H–5 or O–5, H–1 and O–1 have relatively lower crosslinker and higher hydrophilc/oleophilic monomer concentrations. As a result, the higher molecular chain mobility and the larger mesh size increase restructuring ability and allowed polar/nonpolar solvent penetration, thus the posts swell more.

2.4 Summary

In this chapter, we have introduced a new on-demand micromodel fabrication technique with tailored wetting properties. Unlike conventional soft lithography, our approach does not require a master silicon wafer to be prepared in a clean room, nor does it require significant time and effort to fabricate different porous geometries and to modify wetting properties of the micromodels. Geometric features, such as the shape, size, and distance between microstructures can be controlled for micromodel design optimization or systematical study of their effects. At the same time, each structure can have a different wetting property over a continuous range that is preformulated, without additional surface modification steps. This is the first method which can simultaneously create and tailor the wettability of a microstructure in a fluidic device. We demonstrated experiments on immiscible fluid displacement with single posts. We also demonstrated oil-water displacement studies in devices with spatially varying wetting properties. Like real reservoir formations, we can mimic

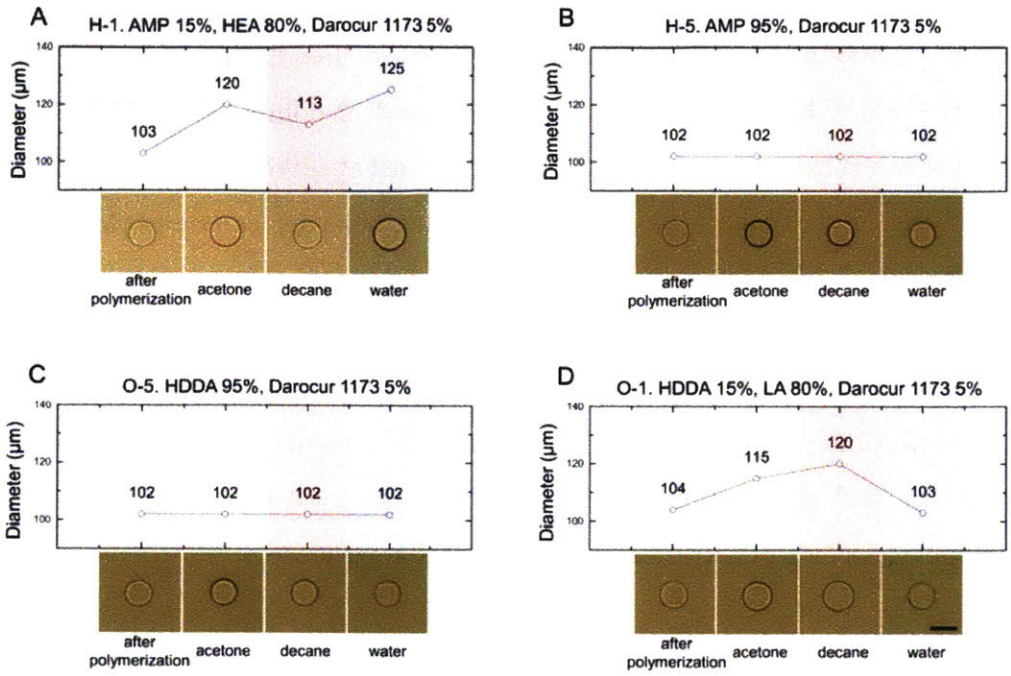

Figure 2-12: The diameters of single posts with different chemical compositions were investigated after polymerization, in acetone, in decane, and in water. Since the diameter of a circle in the photomask used for UV lithography was 790 μm, the diameters of posts have to be 101 μm with a 20x microscope objective lens (projection factor = 7.8). Right after polymerization, all 4 posts showed the same diameters, approximately 103 μm. (A) The most hydrophilic post, H-1, was swelled, and its diameter was increased around 25% in water (B, C) The intermediate posts, H-5 and O-5, without hydrophilic and oleophilic monomers maintained their sizes in different solutions. (D) The most oleophilic post, O-1, was swelled in decane, and its diameter was increased around 20%. Scale bar is 100 μm. (AMP: 1-(acryloyloxy)-3-(methacryloyloxy)-2-propanol, HEA: 2-hydroxyethyl acrylate, HDDA: 1,6-hexanediol diacrylate, LA: lauryl acrylate) Reprinted with permission from Hyundo Lee, Seung Goo Lee and Patrick S. Doyle. "Photopatterned oil-reservoir micromodels with tailored wetting properties." Lab Chip 15 (2015): 3047. Copyright The Royal Society of Chemistry 2015.

locally oleophilic niches within an otherwise hydrophilic channel. To the best of our knowledge, this is also the first micromodel that has more than a binary wettability within it. In addition to the oil-reservoir studies, this fabrication method can be utilized for other applications in microfluidics. For example, one can use our method to rapidly prototype pillar arrangements within a flow device that can then be used to sculpt complex chemical patterns [72]. The controlled wetting within a device can be useful to stabilize fluid-fluid interfaces as particles are pulled across them by magnetic forces for separations [73]. Internal features with controlled wetting will also be useful in capillary guided wetting processes [74] for assembly of cells and organ on chip devices. From the technical side, the microfluidic device production can be improved by a stand-alone, photopatterning setup which has a broader UV lithography area or by a microscope with an automated positioning stage for a precisely controlled configuration of microstructures.

Chapter 3

Understand the Immiscible Oil/Water Displacement as the Interface Passing Obstacles in Microchannels

A method to create liquid chambers at small length scales can enable a large number of parallel experiments to be conducted in a small device. For instance, isolated nanoliter water pockets in a microchannel, much like a multiwell plate system, can be used for applications in diagnostics, drug discovery, and hydrogel synthesis [75–79]. Similarly, entrapped oil pockets can be used to study reaction engineering and to screen chemicals for enhanced oil recovery [80].

In the previous chapter, we proposed a method to trap liquid (both oil and water) in a microchannel by sequentially injecting oil and water (or vice versa) over photopatterned obstacles with controlled wetting properties. The simplicity of the proposed method allows us to control the amount and shape of entrapped liquid by using size, shape, and wettability of the obstacles as design parameters.

In this chapter, we present a method to trap isolated liquid regions in a fluidic device, and we propose a simple geometrical model to understand the liquid-entrapment process and predict the evolution of the water/oil interface over an obstacle. Our analysis provides an analytic solution that can successfully predict useful properties such as angular position of pinch-off and the amount of captured liquid. The model is

able to give insights into the importance of wetting and geometry in controlling the entrapment process that can have broad implications in multiphase flows.

A schematic of our experimental setup to trap oil is presented in Fig.3-1 (a). Following the photopatterning technique introduced in the previous chapter, we photopattern a post with controlled wetting properties within a glass microchannel with height = 50 μm, width = 1 mm, length = 18 mm (Hilgenberg GmbH). We tailor the wetting properties of the post by varying the ratio of monomer and crosslinker in the photopolymer mixture. By using different proportions of lauryl acrylate (monomer, Sigma-Aldrich) and 1,6-hexanediol diacrylate (crosslinker, Sigma-Aldrich), we created posts with 5 different wetting properties (details of photopolymer composition and contact angle measurements are provided in the Appendix). For the most oil-wet case, the post has $\theta_{a,wo} = 144\,^\circ$ (advancing contact angle of water in oil) and $\theta_{r,wo} = 111\,^\circ$ (receding contact angle of water in oil). On the other hand, for the least oil-wet case, the post has $\theta_{a,wo} = 95\,^\circ$ and $\theta_{r,wo} = 82\,^\circ$.

After photopattering the post, the channel is sequentially filled with decane (Sigma-Aldrich) and water by a syringe pump (Harvard Apparatus) at a constant flow rate of 9 μL/min. The encapsulation of oil behind the obstacle involves: (1) decrease in interfacial curvature when water reaches the obstacle (2) oleophilic wetting leading to bending of the interface as it moves over the obstacle and (3) pinch-off when two sides of the interface meet each other (Fig.3-1 (b)).

The procedure to trap water is the same except that it involves creating a water-wet post and sequentially injecting water and decane (*i.e.* inverse of oil case). We photopatterned a water-wet post with $\theta_{a,wo}$=67°, $\theta_{r,wo}$=40° using a specific composition of hydrophilic monomer additive 2-hydroxyethyl acrylate (Sigma-Aldrich) and hydrophilic crosslinker 1-(acryloyloxy)-3-(methacryloyloxy)-2-propanol (Sigma-Aldrich).

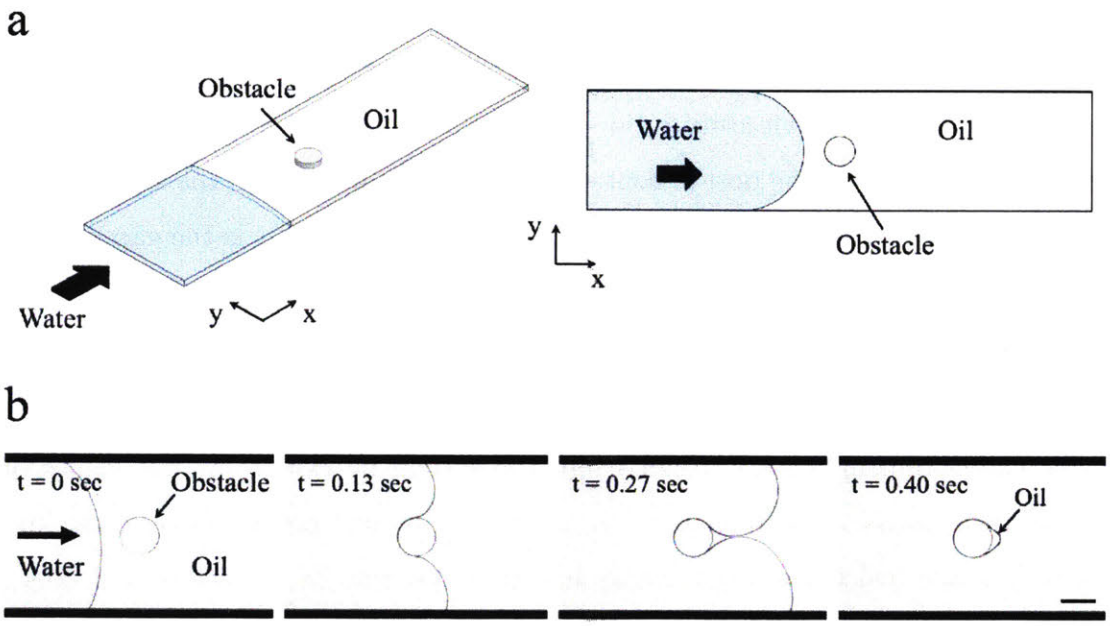

Figure 3-1: Schematics of experimental and theoretical setup. (a) Schematic of immiscible liquid-liquid displacement in a microchannel with an obstacle. For oil entrapment, an oil-wet circular post is first patterned in a flat glass microchannel, and the channel is filled with decane (oil), and water is introduced into the channel. For water entrapment, we create a water-wet post and sequentially flow water and decane (oil). (b) Time series microscope images through the immiscible displacement process for oil entrapment. As displacing water meets the obstacle, water/oil interface starts to bend and encapsulates the obstacle, the interface pinches off when the upper and lower interfaces touch each other at the center-line of the channel. As a result, an oil pocket is left at the posterior region of the obstacle. Scale bar is 200 μm. Reprinted with permission from Hyundo Lee, Ankur Gupta, T. Alan Hatton, and Patrick S. Doyle. "Creating Isolated Liquid Compartments Using Photopatterned Obstacles in Microfluidics." Phys. Rev. Applied 7 (2017): 044013. Copyright 2017 American Physical Society.

3.1 One Circular Post: Theory and Experiments

3.1.1 A Simple Geometric Model under Low Reynolds Number and Low Capillary Number Flow Condition

There are several important dimensionless numbers for the given system: Reynolds number $Re = \frac{\rho_w u_{\text{avg}} H}{\mu_w}$, viscosity ratio $\frac{\mu_o}{\mu_w}$, Capillary number $Ca = \frac{\mu_w u_{\text{avg}}}{\sigma}$, contact angle of oil in water on the post θ, contact angle of oil in water with the side-walls β, and geometric ratio $\frac{R}{W}$, where ρ_w is the density of the water, u_{avg} is the gap-average velocity of water, μ_w is the viscosity of the water, H is the half-height of the channel, μ_o is the viscosity of decane, σ is the interfacial tension between water and decane, R is the radius of the post, and W is the half-width of the channel.

We can obtain important insights into the system by estimating the values of some of the dimensionless numbers. By using the physical properties of water and $u_{\text{avg}} \approx 3$ mm/s (calculated by dividing injection flow rate by cross-sectional area), we calculate $Re \sim O(10^{-1})$. This implies that the flow around the post is laminar and symmetric. $\frac{\mu_o}{\mu_w}$ for decane and water is close to unity and thus we can neglect any viscosity contrast effects. Lastly, by assuming $\sigma \approx 50 \times 10^{-3}$ N/m, we estimate $Ca \sim O(10^{-4})$. Low values of Ca signify that the interface between oil and water is not perturbed by the shear forces, and that we can use a pseudo-static assumption for the interface at each instant in time. Upon varying the input flow rate by three orders of magnitude (0.1 mm/s $\leq u_{\text{avg}} \leq$ 100 mm/s), we did not observe any significant change in oil encapsulation (see Appendix for more details), since the pseudo-static assumption holds for the entire velocity range. For the purpose of this work, we kept the u_{avg} to be constant with $u_{\text{avg}} \approx 3$ mm/s. Based on the above discussion, we assume the interface to be a circular arc in the projected 2-D plane such that it satisfies the static contact angle conditions at the solid boundaries (Fig.3-2). We verify our assumption by fitting the experimental images of interfaces with a circular arc and observe a reasonably good agreement. A circular interface assumption implies a constant curvature and a constant Laplace pressure drop across the interface. Since

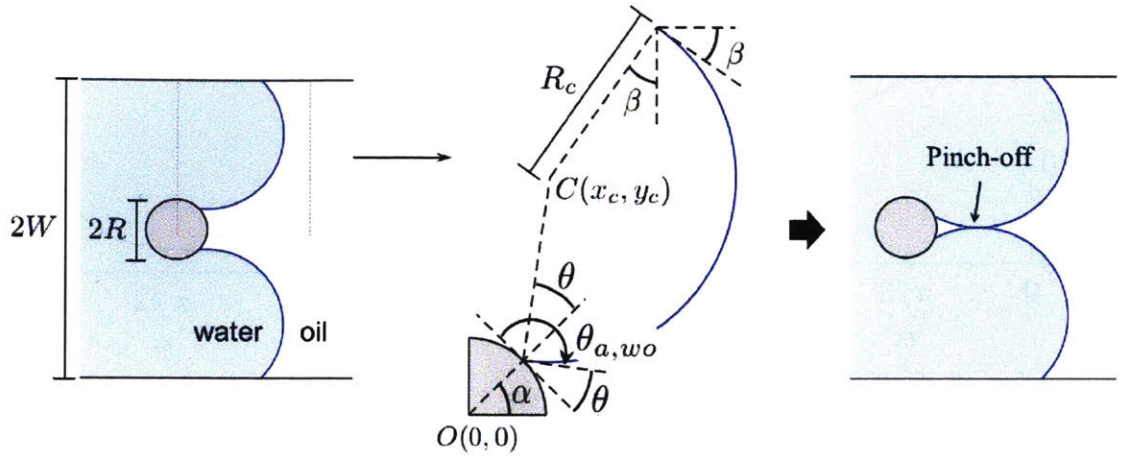

Figure 3-2: Schematic of theoretical setup. Because of the low capillary number of the outer water flow, $O(10^{-5})$, the water/oil interface can be approximated as a circular arc with boundary conditions specified by the contact angles with the two solid surfaces – the obstacle and the channel side wall. Reprinted with permission from Hyundo Lee, Ankur Gupta, T. Alan Hatton, and Patrick S. Doyle. "Creating Isolated Liquid Compartments Using Photopatterned Obstacles in Microfluidics." Phys. Rev. Applied 7 (2017): 044013. Copyright 2017 American Physical Society.

the physical process here involves displacement of oil by water, the relevant contact angle is the advancing contact angle of water-in-oil $\theta_{a,wo}$. However, as shown in Fig.3-2, for simplicity of calculations, we will define θ as the angle subtended by the oil phase with the contact line *i.e.* $\theta = \pi - \theta_{a,wo}$. We assume the center of the post as the origin. The radius of the post is R, the half-width of the channel is W, α is the angle at which the interface touches the post, x_c and y_c are the x and y coordinates of the center of the circular arc, R_c is the radius of the circular arc, and θ and β are the contact angles subtended by oil in water with contact lines of post and side walls. Through geometrical equations and their simplification, we obtain:

$$R\sin(\alpha) + R_c\sin(\alpha+\theta) + R_c\cos(\beta) = W \tag{3.1}$$

$$R\sin(\alpha) + R_c\sin(\alpha+\theta) = y_c \tag{3.2}$$

$$R\cos(\alpha) + R_c\cos(\alpha+\theta) = x_c \tag{3.3}$$

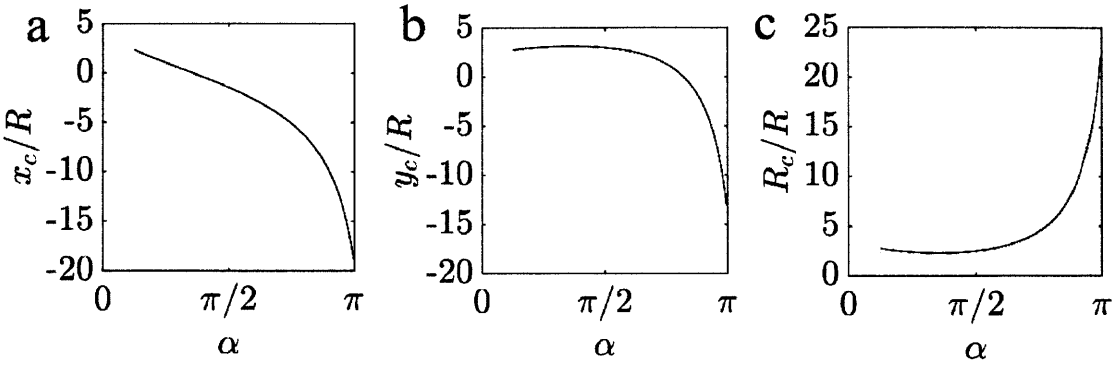

Figure 3-3: Variation of (a) $\frac{x_c}{R}$ (b) $\frac{y_c}{R}$ and (c) $\frac{R_c}{R}$ with α for for $\theta = \frac{37\pi}{180}$, $\beta = \frac{7\pi}{36}$ and $\frac{W}{R} = 5$. Reprinted with permission from Hyundo Lee, Ankur Gupta, T. Alan Hatton, and Patrick S. Doyle. "Creating Isolated Liquid Compartments Using Photopatterned Obstacles in Microfluidics." Phys. Rev. Applied 7 (2017): 044013. Copyright 2017 American Physical Society.

Solving for y_c, x_c and R_c, we get:

$$y_c = \frac{W\sin(\alpha+\theta) + R\sin\alpha\cos\beta}{\sin(\alpha+\theta) + \cos\beta} \tag{3.4}$$

$$x_c = R\cos\alpha + (y_c - R\sin\alpha)/\tan(\alpha+\theta) \tag{3.5}$$

$$R_c = (W - y_c)/\cos\beta \tag{3.6}$$

The above relations define the arc for a general value of α. In Fig.3-3, we plot the variation of $\frac{x_c}{R}$, $\frac{y_c}{R}$, $\frac{R_c}{R}$ with α for $\theta = \frac{37\pi}{180}$, $\beta = \frac{7\pi}{36}$ and $\frac{W}{R} = 5$. When the interface meets the posts *i.e.* $\alpha = \pi$, the 2-D projected interface has very low curvature (or high R_c) as it only has to satisfy the contact angle condition with side-walls and hasn't been confined to flow through a smaller area. The curvature sharply increases as the interface moves over the obstacle until $\alpha \approx \frac{\pi}{2}$, where the flow area is minimum. As the interface continues to move (x_c increases with decrease in α), there is a relatively gradual change in y_c and R_c for $\alpha > \frac{\pi}{2}$, since interface is forced to satisfy wetting conditions with the two solid surfaces, until pinch-off (Fig.3-4 (a)).

For a fixed value of α (a time instant in a real experiment), the pressure disconti-

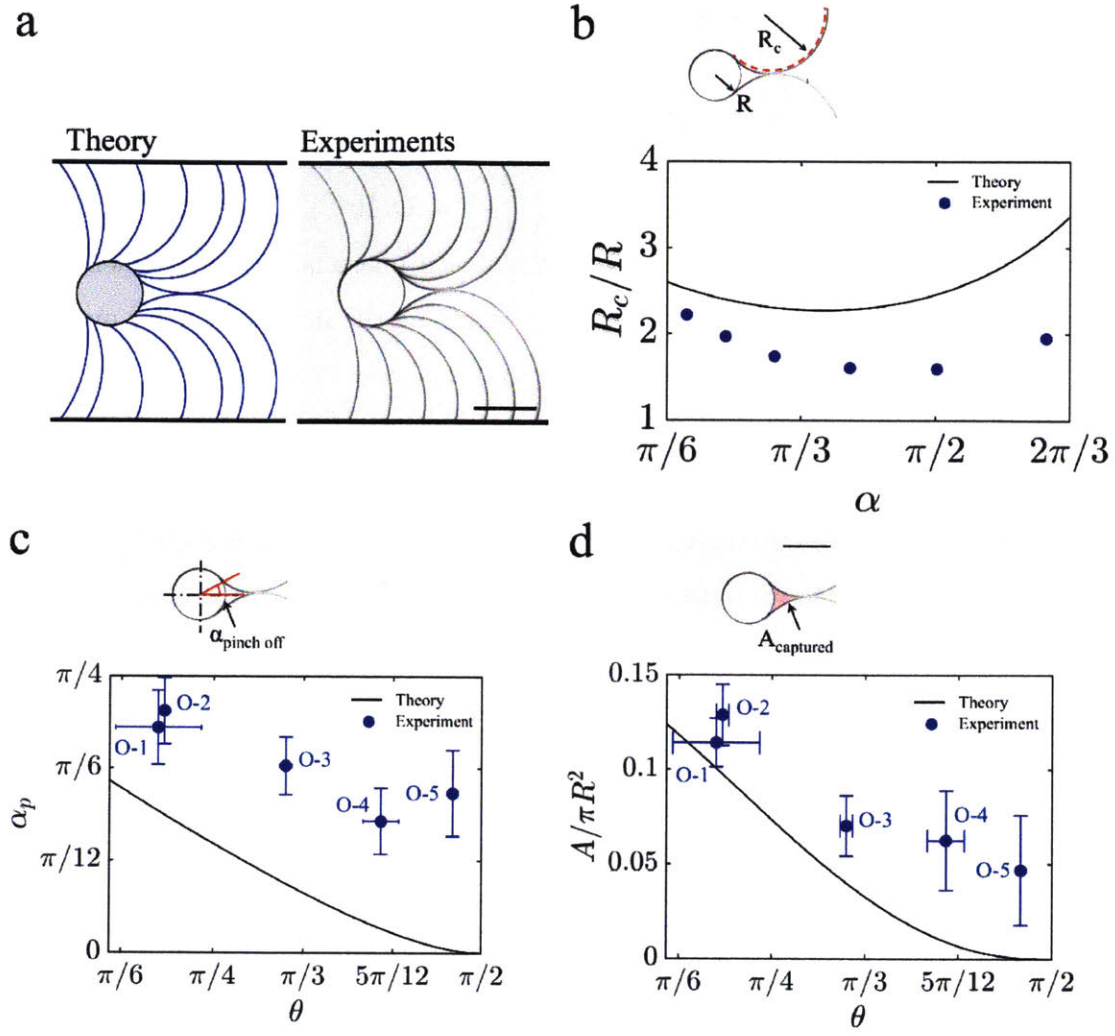

Figure 3-4: (a) Comparison of theory and experiment of oil-water interface evolution for a representative post to verify the hypothesis that the water/oil interface forms a circular arc at low capillary number regime. (b) Evolution of R_c with α and the comparison between theory and experiments. (c) Pinch-off position (α_p) vs. wettability of the circular obstacle (θ = water-oil-solid contact angle) from theory and experiments (d) Amount of captured oil vs. wettability of the circular obstacle. The amount of captured oil is quantified from projected area of oil right before pinching off, and normalized by projected area of circular obstacle for each cases. O–1 to O–5 represent different oil-wet posts having different wetting preference (θ_{O-1}=36°, θ_{O-2}=37°, θ_{O-3}=57°, θ_{O-4}=73°, and θ_{O-5}=85°, estimated by $\theta = \pi - \theta_{a,wo}$, where $\theta_{a,wo}$ is the experimentally measured advancing contact angle of water-in-oil). Scale bars are 200 μm. Reprinted with permission from Hyundo Lee, Ankur Gupta, T. Alan Hatton, and Patrick S. Doyle. "Creating Isolated Liquid Compartments Using Photopatterned Obstacles in Microfluidics." Phys. Rev. Applied 7 (2017): 044013. Copyright 2017 American Physical Society.

nuity is uniform across the interface and is given by the Laplace pressure, Π_L. We can estimate $\Pi_L \approx \sigma\left(\frac{1}{R_c}+\frac{1}{H}\right)$. Moreover, upon comparing the pressure variation in individual phases over a length equal to the half-width of the channel $\Delta P \sim \frac{12\mu_w u_{\text{avg}} W}{H^2}$ to Laplace pressure Π_L, we get $\frac{\Delta P}{\Pi_L} \sim Ca\left(\frac{W}{H}\right) \sim O(10^{-3})$. Therefore a pseudo-static assumption, *i.e.* pressure variation within each phase is negligible when compared to pressure drop across the interface, is valid. As the interface moves over the post, the interfaces from the two sides of the post eventually touch each other (defined to be $\alpha = \alpha_p$) when $y_c = R_c$ (Fig.3-2 (c)), leading to a pinch-off, and subsequent encapsulation of oil. During pinch-off, we sometimes also observe formation of satellite drops [81]. However, we currently ignore such secondary effects in our model. Using the condition of $y_c = R_c$, we obtain the following relation for α_p upon simplification of Equations (3.4-3.6):

$$\frac{R}{W}(1+\cos\beta)\sin\alpha_p + \sin(\alpha_p+\theta) = 1 \tag{3.7}$$

Equation (3.7) can be solved analytically to give the following expression for α_p:

$$\alpha_p = 2\tan^{-1}\left(\frac{a' - \sqrt{a'^2+b'^2-1}}{b'+1}\right) \tag{3.8}$$

where $a' = \frac{R}{W}(1+\cos\beta)+\cos\theta$ and $b' = \sin\theta$.

Let us analyze Equation (3.7) in a limiting case of a very wide channel. For $R/W \approx 0$, we obtain, $\sin(\alpha+\theta) = 1$ or, $\alpha_p = \pi/2 - \theta$. This is an intuitive relation that shows for a more oil-wet post (lower θ), α_p would be higher. In other words, a more oil-wet post can entrap a larger amount of oil. This relation also shows that for neutral ($\theta = \pi/2$) and water-wet posts ($\theta > \pi/2$), $\alpha_p = 0$ and $\alpha_p < 0$ respectively, there will be no oil left on the post. Thus the model is able to capture key features of the entrapment process.

To calculate the projected area of the trapped liquid pocket, we can solve for the

following expression:

$$A = 2\left(\int_{R\cos\alpha_p}^{x_c} f(x)dx - \int_{R\cos\alpha_p}^{R} g(x)dx\right) \tag{3.9}$$

where $f(x) = y_c - \sqrt{R_c^2 - (x - x_c)^2}$ and $g(x) = \sqrt{R^2 - x^2}$. An analytical solution can be obtained for Equation (3.9) as follows:

$$\begin{aligned} A = {} & 2R_c^2\cos(\alpha_p + \theta) - R_c^2\sin(\alpha_p + \theta)\cos(\alpha_p + \theta) - \\ & R_c^2\left(\frac{\pi}{2} - (\alpha_p + \theta)\right) - R^2\alpha_p + R^2\cos\alpha_p\sin\alpha_p \end{aligned} \tag{3.10}$$

3.1.2 Comparison Between Experiment Results and Predictions Based on the Proposed Theoretical Model

We now compare experiment results and theoretical predictions for posts over a wide range of obstacle contact angles (θ). For theoretical predictions, since we are investigating the advancement of the water interface over a surface, we use $\theta = \pi - \theta_{a,wo}$ (since θ is defined as angle subtended by oil with the contact line), where the values of $\theta_{a,wo}$ were measured experimentally. Also, we use $\beta = 7\pi/36$ which was estimated from image analysis of the interface in contact with the side walls.

Fig.3-4 (a) shows the comparison of theory and experiment of interface evolution for a representative post. The predicted evolution of the interfacial curvature (R_c) (Equation (3.6)) and the experimental results obtained by fitting images of the interface with a circle given in Fig.3-4 (b) show similar trends in R_c with α where R_c has a local minimum around $\alpha = \pi/2$, *i.e.* when the gap between the post and the wall is smallest. In addition, the microscopy images from experiments allow us to calculate the angular position of the interface on the post when pinch-off occurs, α_p, and the projected area of the trapped oil, A (Fig.3-4 (c),(d)). The change of α_p and A with respect to θ shows that for a higher value of θ (less oil-wet), lower values of α_p and A are obtained. This is consistent with our expectations since as the post becomes less oleophilic, the water/oil interfaces from the two sides touch further downstream, leav-

ing a smaller amount of entrapped oil. While our model correctly predicts trends in the experimental data, we underpredict the values of both α_p and A (Fig.3-4 (c), (d)). We attribute the disagreement to: (1) the effect of top and bottom walls, currently ignored in our 2-D model, (2) deposition of a thin film of oil on the post that might alter the wetting properties, (3) the difference between measured contact angles on flat surfaces and actual contact angles in small microchannels [82], and (4) change in wetting behavior due to surface roughness and contact angle hysteresis [83, 84].

3.2 Two Circular Posts: Theory and Experiments

We investigate the case of two circular posts separated by a center-to-center distance d (Fig.3-5 (a)). There are two possibilities that arise in such a case: 1) for $d < d_{\text{crit}}$, formation of a liquid bridge connecting two posts (Fig.3-5 (c) i,ii), and 2) for $d \geq d_{\text{crit}}$, formation of two independent oil pockets (Fig.3-5 (c) iii,iv). This is particularly interesting since the liquid bridge has a concave shape unlike a typical isolated droplet. Building on the analysis of the single post case, we develop a theory for two posts to predict the condition for bridging (Fig.3-5 (a)).

$$d = R\cos\alpha + R_c\cos(\alpha+\theta) + (R_c+R)\cos\gamma \tag{3.11}$$

$$y_c = (R_c+R)\sin\gamma \tag{3.12}$$

For a given d, θ, R, W, β, we can solve for x_c, y_c, R_c, α and γ by numerically solving equations retained from geometric relationship. Therefore, for a given spacing between two circular posts, we can predict whether the liquid bridge will form. Further, for a known θ, R, W, β, $\alpha = \alpha_p$ (Equation 3.8), we can also solve for $x_c, y_c, R_c, \gamma, d_{\text{crit}}$. Thus, we can also predict the critical distance (d_{crit}) below which a liquid bridge connecting the two posts will form.

For the wetting conditions used in the experiment (θ_{O-2}=37°), we theoretically

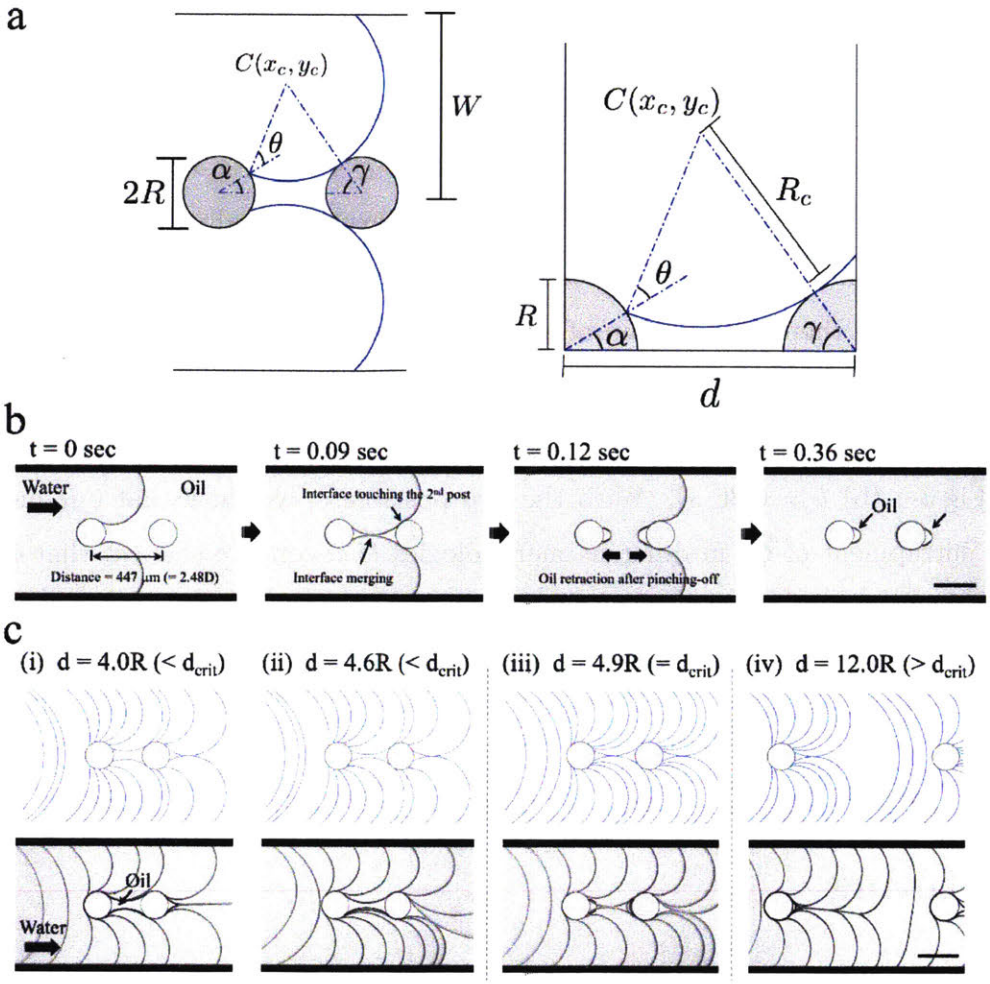

Figure 3-5: Two circular posts case. (a) Theoretical setup for two circular posts case. From the geometrical relationship, we can predict a critical inter-posts distance, d_{crit}. (b) Sequential oil/water displacement images for two circular posts when two posts are placed with the critical distance d_{crit}. Water/oil interface meets the first post and the interface starts to curve around the post. For the critical distance case ($d = d_{\text{crit}}$), the water/oil interface simultaneously touches the center line of the channel and the second post. The liquid bridge connecting two posts is disconnected when the top and bottom interfaces merge together, and the water/oil interface creates the second oil pocket on the second post as the interface moves downstream direction. (c) For a given condition, when the inter-post distance is closer than the critical distance ($d < d_{\text{crit}}$), oil bridge is formed, and connecting the two posts, while when the inter-post distance is farther than the critical distance ($d > d_{\text{crit}}$), two separate oil pockets are formed. Scale bars are 200 μm. Reprinted with permission from Hyundo Lee, Ankur Gupta, T. Alan Hatton, and Patrick S. Doyle. "Creating Isolated Liquid Compartments Using Photopatterned Obstacles in Microfluidics." Phys. Rev. Applied 7 (2017): 044013. Copyright 2017 American Physical Society.

predicted a critical distance of $d_{\text{crit}} \approx 4.9R$, in good agreement with experimental results. We built 4 sets of two circular posts in microchannels having 4 different center-to-center distances (Fig.3-5 (c)). Liquid bridges are formed for $d < 4.9R$ (Fig.3-5 (c) i,ii), and two oil-pockets are left for $d \geq 4.9R$ (Fig.3-5 (c) iv). For the critical case of $d \approx 4.9R$ (Fig.3-5 (c) iii), we observe experimentally that the interfaces meet the center line and touch the second post almost at the same instant (Fig.3-5 (b) $t = 0.09\ s$), and there is formation of an oil pocket on both sides of the second post (Fig.3-5 (b) $t = 0.12\ s$). The oil pocket formed at the upstream region of the second post ultimately moves with the advancing interface and is located at the posterior area (Fig.3-5 (b) $t = 0.36\ s$). With the two posts case, we show that our method allows entrapment of oil in different morphologies (*i.e.* concave shapes) that is not possible in typical techniques. Moreover, the liquid bridges formed in our system are stable against flow instabilities due to geometric confinement where $\frac{R}{H} > 1$ [85–87].

3.3 Different Shapes, Multiple Posts, and Water Capturing

3.3.1 Square, Half-moon and Raindrop Shape Obstacles

Another way to control liquid entrapment is to exploit the shape of the obstacle. Based on the equation of an obstacle perimeter in the x-y plane, we can define the gradient $\frac{dy}{dx}$. We propose that if the liquid-liquid interface encounters a sudden change in gradient when moving along the obstacle (i.e. the contact line), the interface attempts to readjust such that it can satisfy the new contact angle condition. However, during the process of readjustment, the interfaces from the two sides of the obstacle can touch and pinch-off can occur. Hence, we can effectively use the change in slope to suppress the effect of wetting and trap more oil. Here, we choose three additional shapes of posts: square, half-moon and raindrop. A qualitative comparison of predicted and experimental behavior is provided in Fig.3-6 (a). We also have good agreement between theory and experiment for the amount of oil trapped with differ-

ent shapes (Fig.3-6 (b)). The evolution of the interface as predicted by theory shows that, unlike with a circular shape, the interface "pins" at the point of sudden gradient change of square and half-moon shape, and entraps a large amount of oil. When the interface reaches the corner of square and half-moon obstacle, two scenarios are possible: (1) during readjustment, the interface touches the center line and pinches-off, and (2) the interface readjusts to a contact angle of θ with the post, moves inwards, and then pinches-off. We show that for a half-moon shape, scenario (1) is valid even for a neutral wet post. In other words, a neutral wet post effectively traps the same amount of oil as that of an oleophilic post. For a square shape, since the change in gradient is lower as compared to half-moon shape, scenario (1) is valid for a limited range of wetting conditions. We can also design shapes with no gradient change that will effectively trap no oil. For instance, due to the constant gradient along the sides of the raindrop obstacle, the interface "slides" smoothly on the post, and an insignificant amount of oil is left behind at the end. In Appendix, we show that the contact angle θ has to be less than the half-angle of the triangle to get oil entrapment. Hence, the geometry of the obstacle is another useful design parameter to control the shape and amount of oil entrapment.

3.3.2 Multiple Posts for Various Configuration of Oil Capturing

Based on our understanding of oil entrapment developed with circular and other shaped posts, we can envisage several ways to trap different morphologies of oil pockets (Fig.3-6 (c)): (1) a series of posts trap concave-shaped oil pockets by using $d < d_{\text{crit}}$; (2) a throat created by placing multiple posts near the side walls to force the interface to stay away from the wall; and (3) compartmentalized oil entrapment to allow for parallel experimentation using a diamond configuration.

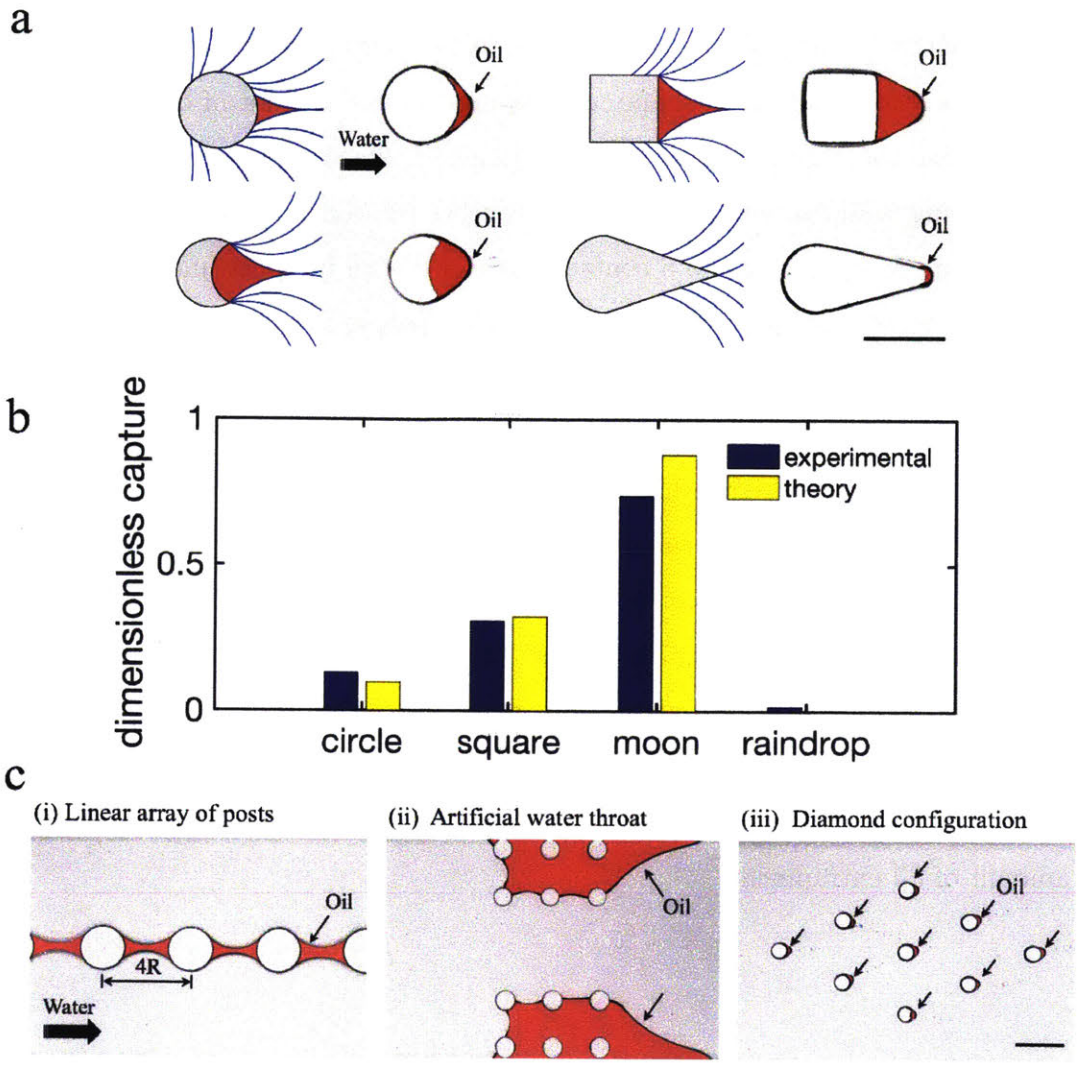

Figure 3-6: (a) Predicted interface evolution by theory and experimental result of oil entrapment with different shapes: circle, square, half-moon, and raindrop shapes (b) Comparison of normalized amount of capture between theory and experimental data with different shapes of obstacle. Projected area of oil is normalized by the area of the posts. (c) Demonstration of different configuration of multiple post cases (i) Linear array. Linear array of posts (equally distanced with 4R) are connected with an oil bridge (ii) Artificial throat. Six posts near the both side of walls create an artificial throat by isolating oil pockets on both sides, from that water flow is passively guided by the oil pockets (iii) Diamond configuration. Circular posts distanced further than their critical distance independently capture oil pockets on each of them. Images are taken in monochrome, and processed to highlight interested area of oil with red color. Scale bars are 200 μm. Reprinted with permission from Hyundo Lee, Ankur Gupta, T. Alan Hatton, and Patrick S. Doyle. "Creating Isolated Liquid Compartments Using Photopatterned Obstacles in Microfluidics." Phys. Rev. Applied 7 (2017): 044013. Copyright 2017 American Physical Society.

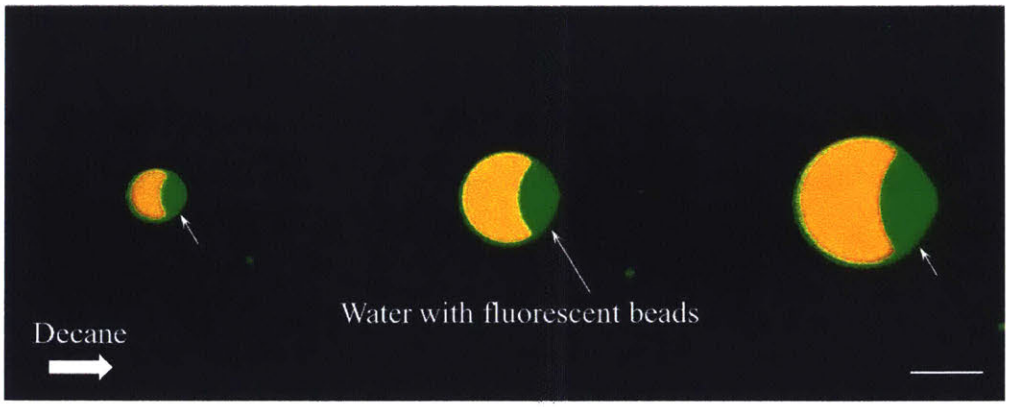

Figure 3-7: Water-encapsulation experiment where water and decane were sequentially injected over water-wet posts. For fluorescent imaging, 4% v/v of 0.1 mg/mL rhodamine acrylate (orange) dissolved in poly(ethylene) glycol (PEG) was added to the prepolymer solution, and 100 nm fluorescent polystyrene microspheres (green) were added in water (10% v/v) in water/oil displacement. Scale bar is 200 μm. Reprinted with permission from Hyundo Lee, Ankur Gupta, T. Alan Hatton, and Patrick S. Doyle. "Creating Isolated Liquid Compartments Using Photopatterned Obstacles in Microfluidics." Phys. Rev. Applied 7 (2017): 044013. Copyright 2017 American Physical Society.

3.3.3 Water Capturing with Hydrophilic Posts by Inversed Flow Sequence

As mentioned previously, our method also allows us to trap water pockets which we have imaged fluorescently in three different sized polymerized half-moon shapes (Fig.3-7). Further, because we use half-moon shaped obstacles, we reliably trap a significant amount water behind the post, a feature particularly useful for potential studies in diagnostics and drug discovery.

3.4 Summary

In this chapter, we present a method to trap oil and water pockets in a single step by sequential injection of oil and water (or vice versa) over photopatterned obstacles with controlled wetting properties. We demonstrate that we can control the amount of trapped liquid by tuning the contact angle as well as the shape of the obstacle. By

exploiting the property of wetting, we show the ability to generate concave-shaped pockets and isolated pockets for parallel experimentation. Our platform can be used to create isolated aqueous pockets containing biological entities that can be further probed through subsequent reactions [78]. which can be useful in applications such as drug discovery and diagnostics where parallel experimentation is required. The approach can be easily coupled with existing methods to create isolated alginate-based hydrogels [88]. Also, by entrapping controlled amounts of oil, our technique can be used for the screening of chemicals for enhanced oil recovery (EOR). Our work highlights the role of obstacle shape in affecting the amount of oil trapped in a reservoir, an effect that is usually ignored since researchers generally use arrays of cylinders to mimic porous media in microfluidic devices. We hope this work will motivate two phase flow studies in porous media in which shape effects of obstacles are considered. Further, unlike traditional oil-recovery techniques such as core flooding, our platform is compatible with advanced microscopy techniques to provide useful insights into the mechanism of oil release during EOR. Our work can also have implications in fiber coating where one can envision an obstacle as representing the cross section of a fiber. Prior work on fiber wetting or coating is limited to circular cross sections [89, 90]. Similarly, the understanding of noncircular shapes can be applied to the coating of nonspherical magnetic particles that are typically synthesized using microfluidic techniques [91, 92]. Finally, since our method can be modeled through geometric calculations, it can be a good model system for fundamental studies of multiphase flows and wetting.

Chapter 4

Controlled Parallel Liquid Compartments with Periodic Patterns using Liquid-Liquid Displacement

In oil recovery and soil remediation, displacement of liquids such as oils and liquid pollutants from the pores is typically achieved by injecting another liquid [22, 25, 56, 93–95]. The geometric morphology of the pores naturally plays an important role in liquid recovery where surface roughness creates challenges in displacing the trapped liquid. Roughness often plays a detrimental role for the above applications. In contrast, several applications prefer a liquid layer over a rough surface. In diagnostic research, for instance, there is an increasing interest in building microfluidic platforms that create isolated aqueous microreactors. Such isolation of aqueous environment is achieved by introducing an artificial defect on the surface such as an obstacle or a depression [74, 78, 96–98]. Similarly, extensive research on liquid-infused surfaces demonstrate that a trapped liquid layer over a patterned surface lends remarkable surface properties [99–106]. Thus depending on the application, it maybe desirable to either remove or trap a liquid layer over a surface.

There have been a series of studies on liquid infused surfaces with geometric features on the order $\sim$ 10 μm where the authors show how the pre-existing layer of oil in a groove (a model for liquid infused surface) can be drained by injecting wa-

ter [103–106]. They also examined the effect of aspect ratio of the groove, presence of obstacles, viscosity ratio of the two phases, and presence of surfactant in the aqueous phase on the oil drainage. Though these studies are very useful for fundamental understanding of the oil drainage process, the investigators did not consider the effect of groove shape. In the previous chapter, we introduce our study of oil entrapment over isolated obstacles and demonstrated the importance of obstacle shape in controlling the entrapment process [107].

In this chapter, we systematically examine the displacement of a pre-existing layer of oil over a photopatterned wavy surface to understand the effect of surface roughness on displacement of oil. Specifically, we study the effect of oil displacement by water over triangular and sinusoidal patterned sidewalls in a microchannel. The variations in amplitude and frequency allow us to control the surface roughness. We describe a simple geometrical model to explain the evolution of the interface and validate it with our experimental results. The model provides useful physical insights about the process and specifically helps identify relative importance of dimensionless length scales that govern the system. We experimentally validate the criterion to remove or trap the pre-existing oil inside the pattern. In addition to the analysis on liquid encapsulation in the troughs, we also present demonstration of oil recovery model study with surfactant flooding experiment and anlysis of the recovery process. We believe our results will be useful for research in oil recovery, soil remediation, diagnostics and liquid-infused surfaces. Our study can also be useful in fiber coating and printing applications where the shape of fibers and printing grooves can influence the physical process [89,90,108–110]. Lastly, we hope our results will help researchers building models for porous media flows to incorporate the effect of surface shape.

4.1 Setup for Experiments and Proposed Theoretical Model

A schematic of our experimental setup to study immiscible liquid displacement is presented in Fig.4-1 (a). We use an acrylated glass microchannel (Hilgenberg GmbH) with length $L = 18$ mm (x-direction), width $W = 1$ mm (y-direction), and height $H = 50$ μm ($z-$direction). We first fill the channel with a mixture of photocurable polyurethane acrylate precursor (MINS 311RM, Minuta Tech.) with 5% (volume/volume) photoinitiator 2-hydroxy-2-methylpropiophenone (Sigma Aldrich). Using microscope-projection lithography, we photopattern a repetitive structure at one of the sidewalls [78,107,111–115]. In this study, we pattern triangular and sinusoidal structures with 30 different combinations of wavelength (λ) and amplitude (A_0). We use 6 different wavelengths $\lambda = [250, 350, 400, 500, 750, 1000]$ μm and 5 different amplitudes $2A_0 = [75, 100, 200, 300, 400]$ μm. For a distance of 250 μm before and after the pattern, we create a flat structure with amplitude $2A_0$ to ensure smooth displacement at the entrance and exit. After the photopatterning step, we sequentially fill the channel with oil (decane, Sigma-Aldrich) and water by a syringe pump (Harvard Apparatus) at a constant flow rate $Q = 5$ μL/min.

To model our physical system, we define the following variables: density of water ρ_w, density of oil ρ_o, viscosity of water μ_w, viscosity of oil μ_o, interfacial tension between oil and water σ, oil-in-water contact angle with patterned sidewall θ, and oil-in-water contact angle with un-modified sidewall β. Physical variables combined with geometrical parameters yield several dimensionless groups such as Reynolds number Re= $\frac{\rho_w Q}{W\mu_w}$, capillary number Ca= $\frac{\mu_w Q}{WH\sigma}$, aspect ratio $\frac{H}{W}$, dimensionless amplitude $m = \frac{A_0}{W}$, dimensionless frequency $n = \frac{W}{\lambda}$, viscosity ratio $N = \frac{\mu_o}{\mu_w}$, and contact angles θ and β. We also define angle α such that $\tan(\alpha) = 4mn$.

As we demonstrated in the previous chapter, significant simplifications are possible under certain physical conditions for an immiscible liquid displacement process [107]. We can neglect effects due to viscosity contrast since we use decane and water in our system for which $N \approx 1$. For the operating conditions we used in our system,

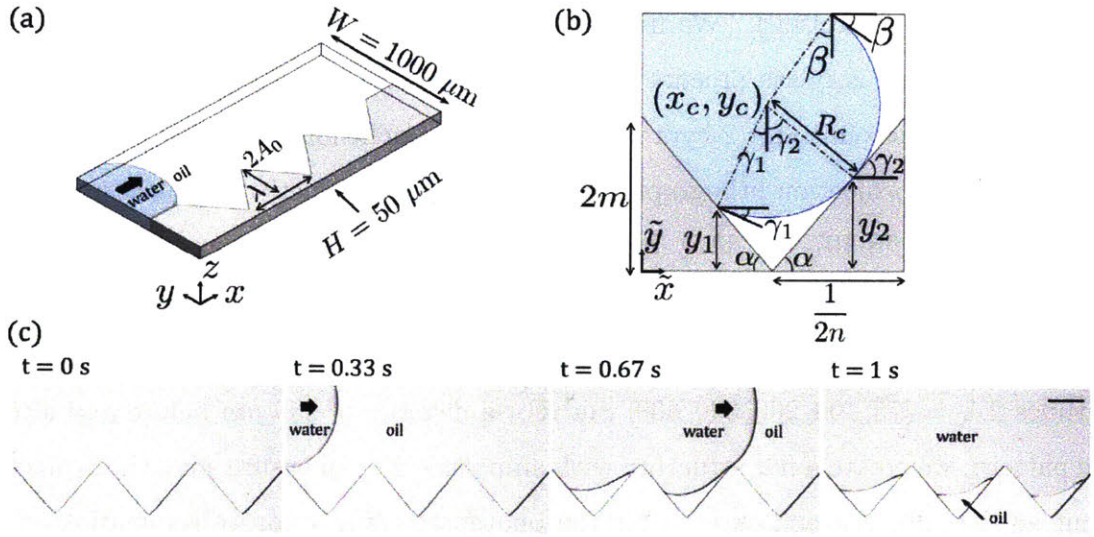

Figure 4-1: (a) Schematic of the experimental setup. Immiscible liquid-liquid displacement in a glass microchannel over a triangular patterned sidewall. The channel is first filled with oil (decane) and then water is introduced into the channel. (b) Schematic of the theoretical setup. The triangular geometry can be represented by two dimensionless length scales: amplitude $m = \frac{A_0}{W}$ and frequency $n = \frac{W}{\lambda}$. We also define angle α such that $\tan(\alpha) = 4mn$. For low capillary and Reynolds numbers, we approximate the interface between oil and water as a circular arc that satisfies static contact angle conditions at fluid-solid interfaces. We describe the circular arc in terms of angle of intersection with horizontal at left-triangular wall (γ_1), angle of intersection with horizontal at right-triangular wall (γ_2), and angle of intersection with horizontal at top sidewall (β). (c) Time-series microscope images from experiments during the immiscible displacement process. Scale bar is 200 μm.

Re $\approx$ 0.08 and Ca $\approx 3 \times 10^{-5}$. Low values of Re and Ca imply that interfacial stress significantly dominates over viscous and inertial stresses, and so the interface is not perturbed by the flow. Therefore, we neglect the pressure drop over a length scale of W within the water phase $\Delta P \sim \frac{12\mu_w Q}{H^3}$ relative to pressure drop across the interface $\Pi \sim 4\sigma\left(\frac{1}{W}+\frac{1}{H}\right)$ as $\frac{\Delta P}{\Pi} \approx 3\text{Ca}\left(\frac{W}{H}\right) \approx 6 \times 10^{-4}$. A similar analysis is also possible for the oil phase. Therefore we assume quasi-static flow conditions and model the interface between oil and water phase in the $x-y$ plane as a circular arc that satisfies the static contact angle conditions at the fluid-solid boundaries.

Fig.4-1 (b) is a schematic of our theoretical setup for a triangular patterned sidewall. We assume the origin to be at the bottom left corner and scale the coordinates with W to define $\tilde{x} = \frac{x}{W}$ and $\tilde{y} = \frac{y}{W}$. In rest of the chapter, all the discussion is in a dimensionless coordinate system and for simplicity, we drop the $\tilde{}$ from the dimensionless coordinates. To construct a circular arc, we need to find three quantities: x-coordinate of the center of the arc x_c, y-coordinate of the center of the arc y_c, and the radius of the arc R_c. In particular, we are interested in the arc that subtends an angle γ_1 with horizontal at the left triangular-wall, γ_2 with horizontal at the right triangular-wall, and β with horizontal at the top sidewall. We note that the height of intersection at left and right triangular walls need to be such that $0 \leq y_1, y_2 \leq 2m$. Though it might appear that the arc should always intersect the left triangular wall at angle θ or $\gamma_1 = \alpha - \theta$, and should touch the right triangular wall or $\gamma_2 = \alpha$, we show later that since y_1 and y_2 are bounded, γ_1 and γ_2 are not always $\alpha - \theta$ and α respectively.

Fig.4-1 (c) shows representative time-series of microscope images during the immiscible displacement process. As the water displaces the oil phase in a triangular trough, the interface moves downward on the left triangular wall until the interface touches the right triangular wall (see $t = 0.67$ s). The interface then pinches off and breaks into two parts where one part stays behind with the trapped oil and the other progresses to the next triangular trough. The microscope images suggest that after the breakup of the interface, the interface with the trapped oil readjusts its curvature to satisfy the contact angle condition. We note that our geometrical model is a

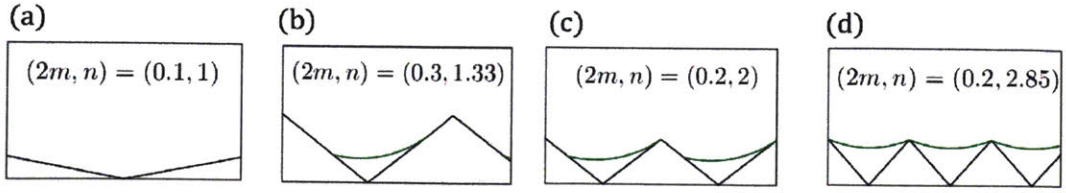

Figure 4-2: Four representative cases for oil capture in a triangular pattern obtained from theory: (a) $y_1 = 0, y_2 = 0$, (b) $0 < y_1 < 2m, 0 < y_2 < 2m$, (c) $0 < y_1 < 2m, y_2 = 2m$, and (d) $y_1 = 2m, y_2 = 2m$.

first-order approximation of the actual experiments and only captures the interface evolution until the interface meets the right triangular wall.

We now discuss how to evaluate x_c, y_c and R_c. From Fig.4-1 (b), we write the following equations using geometry:

$$y_c = y_1 + R_c \cos\gamma_1 \tag{4.1}$$

$$y_c = y_2 + R_c \cos\gamma_2 \tag{4.2}$$

$$1 = y_c + R_c \cos\beta \tag{4.3}$$

$$x_c = \frac{1}{2n} - \frac{y_1}{\tan\alpha} + R_c \sin\gamma_1 \tag{4.4}$$

$$x_c = \frac{1}{2n} + \frac{y_2}{\tan\alpha} - R_c \sin\gamma_2 \tag{4.5}$$

Equations (4.1-4.5) are also subjected to the constraints $0 \leq y_1 \leq 2m$ and $0 \leq y_2 \leq 2m$. Therefore, we divide the entrapment process for a triangular pattern into 4 cases, as shown in Fig.4-2.

1. $y_1 = 0$, $y_2 = 0$. This is the case of no-entrapment, as shown in Fig.4-2 (a). Here, $\gamma_1 = \alpha - \theta$ and $\gamma_2 = \alpha$. We subtract Equation (4.4) from Equation (4.5) to obtain $y_1 + y_2 = R_c \tan\alpha(\sin\alpha + \sin(\alpha - \theta))$. Upon simplification we obtain $y_1 + y_2 \leq 0$ when:

$$\tan\alpha = 4mn \leq \tan\frac{\theta}{2} \tag{4.6}$$

ence, there is no capture when $4mn \leq \tan\frac{\theta}{2}$. This is consistent with qualitative expectation, *i.e.* for higher values of m and n, or larger amplitudes and frequencies, we are more likely to get oil entrapment.

2. $0 < y_1 < 2m$, $0 < y_2 < 2m$. This is the case of entrapment when both y_1 and y_2 are not at the end of left and right triangular walls, as shown in Fig.4-2 (b). As discussed, for this case, we require that $4mn > \tan\frac{\theta}{2}$. In this case too, $\gamma_1 = \alpha - \theta$ and $\gamma_2 = \alpha$. Therefore, we solve Equations (4.1-4.5) to get x_c, y_c, R_c, y_1 and y_2. Here we give the solutions of y_1 and y_2 after simplifications (rest of the variables can be evaluated from Equations (4.1-4.5)):

$$y_2 = \frac{\cos^2\frac{\theta}{2} - \cos^2\alpha}{\cos^2\frac{\theta}{2} + \cos\alpha\cos\beta} \tag{4.7}$$

$$y_1 = y_2\left(\frac{1 - \frac{\tan\frac{\theta}{2}}{\tan\alpha}}{1 + \frac{\tan\frac{\theta}{2}}{\tan\alpha}}\right) \tag{4.8}$$

Equations (4.7-4.8) show that $y_1 \leq y_2$. Since above equations are only valid when $0 \leq y_2 \leq 2m$, we can also evaluate the condition for α when $y_2 = 2m$ from Equation (4.7). Moreover, we also recover back Equation (4.6), *i.e.* $y_1, y_2 = 0$ when $\tan\alpha = \tan\frac{\theta}{2}$.

3. $0 < y_1 < 2m$, $y_2 = 2m$. This is the case of entrapment when y_2 is at the end of right triangular wall but y_1 is still in the middle, as shown in Fig.4-2 (c). In such a case, the interface intersects the right triangular wall at an angle and is no longer tangential. We solve for $x_c, y_c, R_c, y_1, \gamma_2$ from Equations (4.1-4.5) by substituting $y_2 = 2m$, $\gamma_1 = \alpha - \theta$ and keeping γ_2 as a variable. Below we provide a solution for γ_2 after appropriately rearranging the equations (rest of the variables can be calculated from Equations (4.1-4.5)):

$$\cos\gamma_2+\left(\frac{4m}{2m+1}\right)\cos\beta+\left(\frac{2m-1}{2m+1}\right)\frac{\cos\theta}{\cos\alpha}+\left(\frac{2m-1}{2m+1}\right)\tan\alpha\sin\gamma_2=0 \quad (4.9)$$

Equation (4.9) has an analytical solution for $\cos\gamma_2 = \dfrac{-c_1+\sqrt{b_1^4+b_1^2(1-c_1^2)}}{1+b_1^2}$ where $b_1 = \left(\dfrac{2m-1}{2m+1}\right)\tan\alpha$, $c_1 = \left(\dfrac{4m}{2m+1}\right)\cos\beta + \left(\dfrac{2m-1}{2m+1}\right)\dfrac{\cos\theta}{\cos\alpha}$. Thus we can evaluate the complete solution for the case when the interface reaches top of the right triangular wall.

4. $y_1 = 2m$, $y_2 = 2m$. This is the case of entrapment when both y_1 and y_2 are at the end of left and right triangular walls, as shown in Fig.4-2 (d). We solve Equation (4.1-4.5) by using $y_1 = 2m$, $y_2 = 2m$ and substituting γ_1 and γ_2 as variables. We observe that the system is now symmetric or $\gamma_1 = \gamma_2 = \gamma$. Here we provide an equation to solve for γ (rest of the variables can be calculated from Equations (4.1-4.5)):

$$\cos\gamma+\cos\beta+\tan\alpha\left(\frac{2m-1}{2m}\right)\sin\gamma=0 \quad (4.10)$$

Equation (4.10) also has an analytical solution for $\cos\gamma = \dfrac{-c_1+\sqrt{b_1^4+b_1^2(1-c_1^2)}}{1+b_1^2}$ where $b_1 = \left(\dfrac{2m-1}{2m}\right)\tan\alpha$, $c_1 = \cos\beta$. Equation (4.10) is independent of θ which is expected since the interface at the left triangular wall is not subtending the contact angle. Also, for the extreme case of $\alpha = \pi/2$, the equation yields $\gamma = 0$, or the interface becomes a straight line connecting the extreme points of the triangular pattern. This result is also consistent with expectation. Lastly, the condition for $y_1 = 2m$ also captures the effect of pinning *i.e.*, for large values of $\tan\alpha$ or larger slopes of triangular pattern, the interface is pinned at the extreme point at the left triangular wall, and traps a large amount of oil.

Once we obtain the solution for y_1, y_2, R_c, γ_1, γ_2, we can find the amount of oil trapped by calculating the area between the interface and the patterned surface.

$$\tilde{a} = \frac{\frac{y_1 y_2}{\tan\alpha} + \frac{R_c^2}{2}\left(\sin\left(\gamma_1+\gamma_2\right) - \gamma_1 - \gamma_2\right)}{\frac{4m^2}{\tan\alpha}} \tag{4.11}$$

However, we can approximate the amount of oil trapped by finding the area of triangle formed by y_1, y_2 and the lowest point of the trough. The dimensionless amount of oil entrapped $\tilde{a}$ is defined as the ratio of the area between the interface and the pattern relative to the area of the pattern:

$$\tilde{a} \approx \frac{\frac{1}{2}\frac{y_1}{\sin\alpha}\frac{y_2}{\sin\alpha}\sin\left(\pi - 2\alpha\right)}{\frac{4m^2}{\tan\alpha}} \approx \frac{y_1 y_2}{4m^2} \tag{4.12}$$

For a constant value of mn (or α) and θ, Equation (4.12) predicts:

$$y_1 = 0, y_2 = 0 \implies \tilde{a} = 0 \tag{4.13}$$

$$y_1 < 2m, y_2 < 2m \implies \tilde{a} \sim m^{-2} \tag{4.14}$$

$$y_1 < 2m, y_2 = 2m \implies \tilde{a} \sim m^{-1} \tag{4.15}$$

$$y_1 = 2m, y_2 = 2m \implies \tilde{a} \sim 1 \tag{4.16}$$

4.2 Results – Comparison between Experiment and Theoretical Prediction

4.2.1 Triangular Pattern

A summary of our experimental and theoretical results for a range of m and n are provided in Fig. 4-3. Values of $\theta = \frac{25\pi}{180}$ and $\beta = \frac{35\pi}{180}$ are used for theoretical calculations. Overall our experimental and theoretical results are consistent with expectation since the amount of trapped oil increases with increase in both m and n. A qualitative comparison between amount of oil trapped in images from experiments and predicted from theory suggests good agreement. We note that the higher the

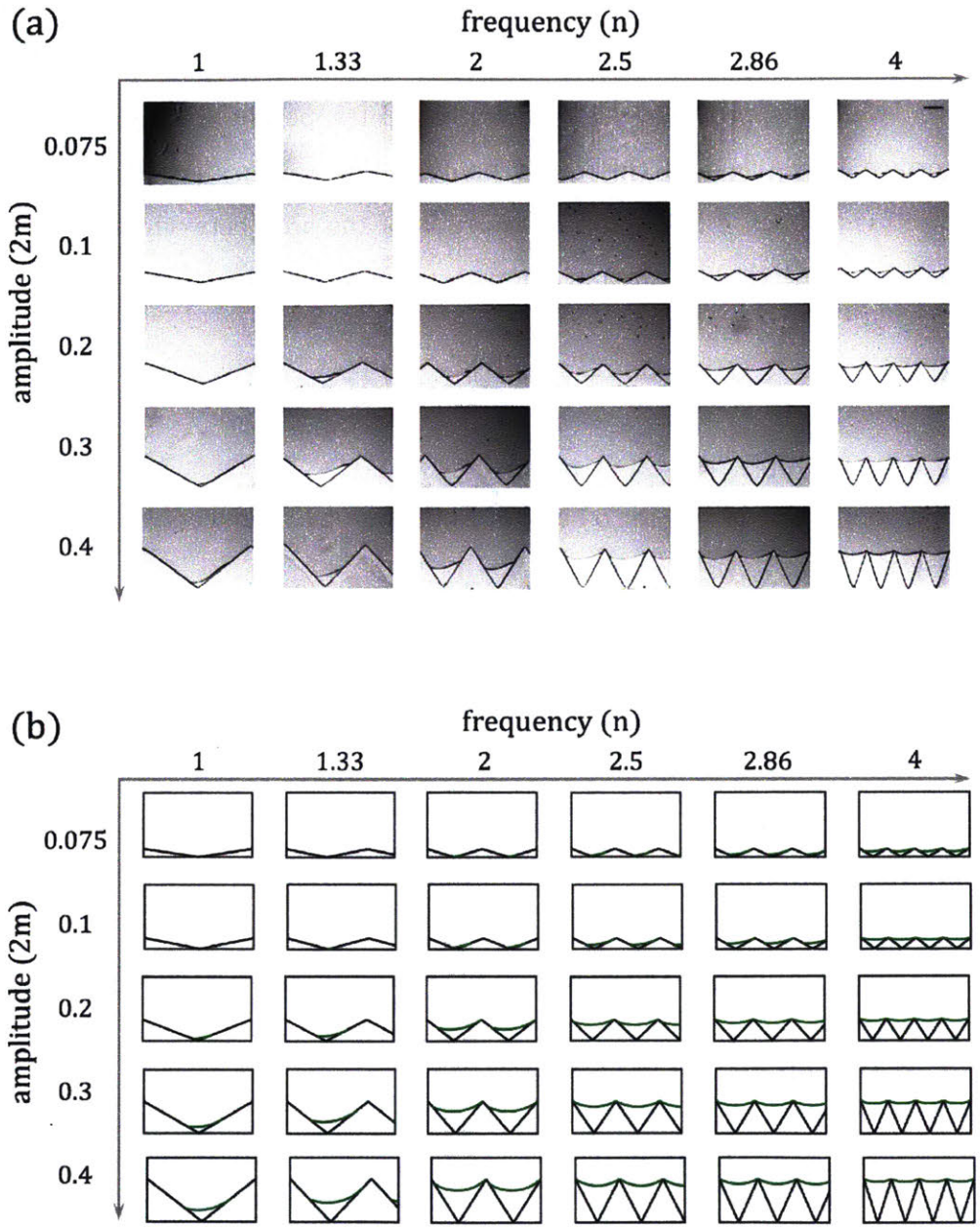

Figure 4-3: (a) Experiment results and (b) theoretical map of entrapped oil for triangular pattern with different values of frequency (n) and amplitude ($2m$). The amount of oil trapped increases with increase in amplitude and frequency. Scale bar in experimental images is 200 μm. Values of $\theta = \frac{25\pi}{180}$ and $\beta = \frac{35\pi}{180}$ were used for theoretical calculations.

value of m, the critical value of n at which there is non-zero oil capture is lower. We predict this trend in Equation (4.6) that for a non-zero oil capture the frequency should be greater than $n_{\text{crit, theory}} = \frac{1}{4m}\tan\left(\frac{\theta}{2}\right)$. For $2m = [0.075, 0.1, 0.2, 0.3, 0.4]$, our model predicts $n_{\text{crit, theory}} = [2.7, 2.0, 1.0, 0.59, 0.51]$. The experiments show non-zero capture for $n \geq [2.8, 2.5, 1.33, 1.0, 1.0]$ which is in accordance with our prediction. Equation (4.6) shows we can combine the effect of amplitude and frequency to predict the transition from no capture to capture in the parameter mn, a measure of slope of the triangle.

4.2.2 Sinusoidal Pattern

Since the slope stays constant in a triangular pattern, we photopolymerized a sinusoidal structure with equation $y = m\,(1 + \cos(2\pi n x))$ to explore the effect of variation in local slope. We created structures with the same ranges of m and n to do a direct comparison with the results from the triangular patterns. We also modified the theoretical calculations for sinusoidal patterns.

A schematic of the theoretical setup for a sinusoidal pattern is provide in Fig.4-4. Similar to the triangular pattern, we write the following equations from geometrical balances:

$$y_c = y_1 + R_c \cos\gamma_1 \tag{4.17}$$

$$y_c = y_2 + R_c \cos\gamma_2 \tag{4.18}$$

$$1 = y_c + R_c \cos\beta \tag{4.19}$$

$$x_c = x_1 + R_c \sin\gamma_1 \tag{4.20}$$

$$x_2 = x_c + R_c \sin\gamma_2 \tag{4.21}$$

where:

$$y_1 = f(x_1) = m(1 + \cos(2\pi n x_1)) \tag{4.22}$$

$$y_2 = f(x_2) = m(1 + \cos(2\pi n x_2)) \tag{4.23}$$

$$\tan\alpha = -f'(x_1) = 2\pi mn \sin(2\pi n x_1) \tag{4.24}$$

$$\cos\gamma_1 = \cos\alpha\cos\theta + \sin\alpha\sin\theta \tag{4.25}$$

$$\sin\gamma_1 = \sin\alpha\cos\theta - \sin\theta\cos\alpha \tag{4.26}$$

$$\tan\gamma_2 = f'(x_2) = -2\pi mn \sin(2\pi n x_2) \tag{4.27}$$

Equation (4.17 - 4.21) are combined with Equation (4.22 - 4.27) and are numerically solved for x_1, x_2, x_c, y_c, and R_c under the constraint $0 \leq y_1, y_2 \leq 2m$. We note that the sinusoidal pattern only has one regime where $\gamma_1 = \alpha - \theta$ is always true, unlike triangular pattern. Also, due to range of slope available in the sinusoidal pattern, the interface is always able to touch the right side of the pattern.

The results from sinusoidal patterns are summarized in Fig.4-5. Fig.4-5 shows that similar to triangular structures, the oil capture increases with m and n, and experimental trends are shown in the theoretical prediction. For $2m = [0.075, 0.1, 0.2, 0.3, 0.4]$, we observe that the experiments show non-zero capture in a sinusoidal pattern for $n \geq [2.5, 2.0, 1.33, 1.0, 1.0]$ and the theory predicts $n_{\text{crit, theory}} = [2.3, 1.9, 1.2, 0.95, 0.8]$. Thus experiments and theory are in agreement for the transition from no-capture to capture. However, we note that for a sinusoidal pattern, the relationship $n_{\text{crit, theory}} \sim m^{-1}$ is no longer valid since the local slope continuously changes with position. Therefore, a comparison of $n_{\text{crit, theory}}$ between triangular and sinusoidal patterns shows that at low values of m, $n_{\text{theory, crit}}$ is lower for sinusoidal patterns, and the trend reverses for higher values of m. To understand these results, we can envision sinusoidal pattern as piece-wise linear segments with varying slopes. At low values of m, the interface is less curved due to lack of confinement. As the interface moves down the left sidewall of the sinusoidal pattern, it meets with regions of large local slope in right side of the pattern, otherwise not possible in a triangular pattern. In contrast, at high values of m, the interface is forced to bend more and misses the region of large local slope.

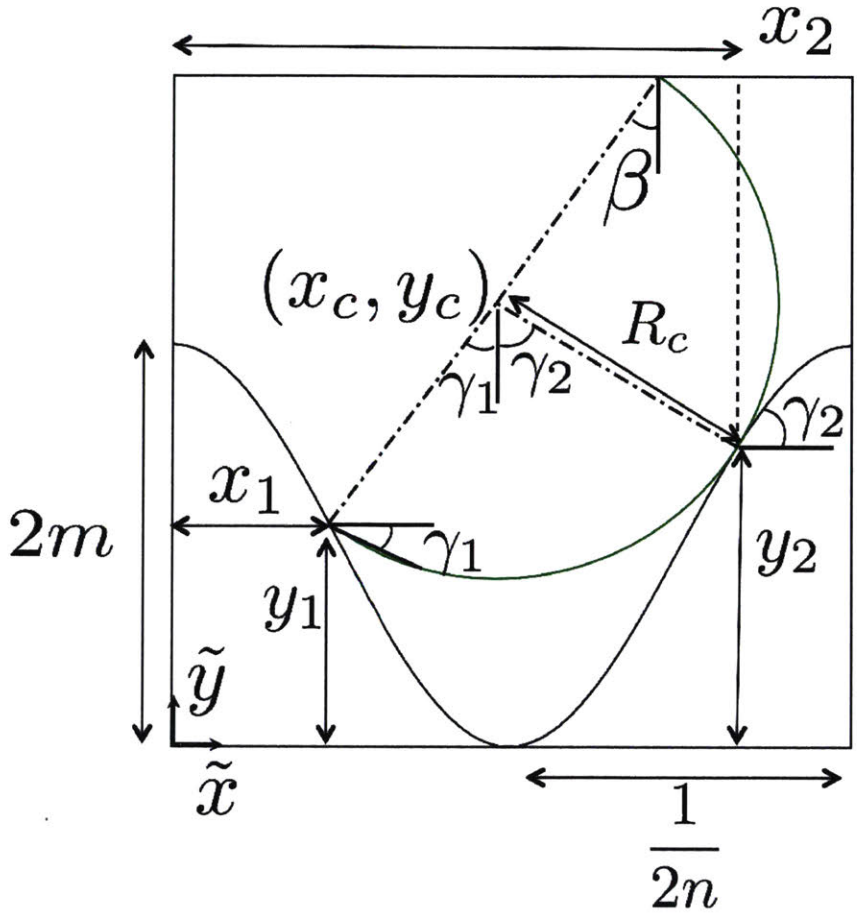

Figure 4-4: Schematic of the theoretical setup. The sinusoidal geometry here is mathematically describe as $y = m(1 + \cos(2\pi n x))$ where m and n are two dimensionless length scales given by: amplitude $m = \frac{A_0}{W}$ and frequency $n = \frac{W}{\lambda}$. For low capillary and Reynolds numbers, we approximate the interface between oil and water as a circular arc that satisfies static contact angle conditions at fluid-solid interfaces. We describe the circular arc in terms of angle of intersection with horizontal at the left wall (γ_1) where $0 \leq x \leq \frac{1}{2n}$, angle of intersection with horizontal at right wall (γ_2) where $\frac{1}{2n} \leq x \leq \frac{1}{n}$, and angle of intersection with horizontal at top sidewall (β).

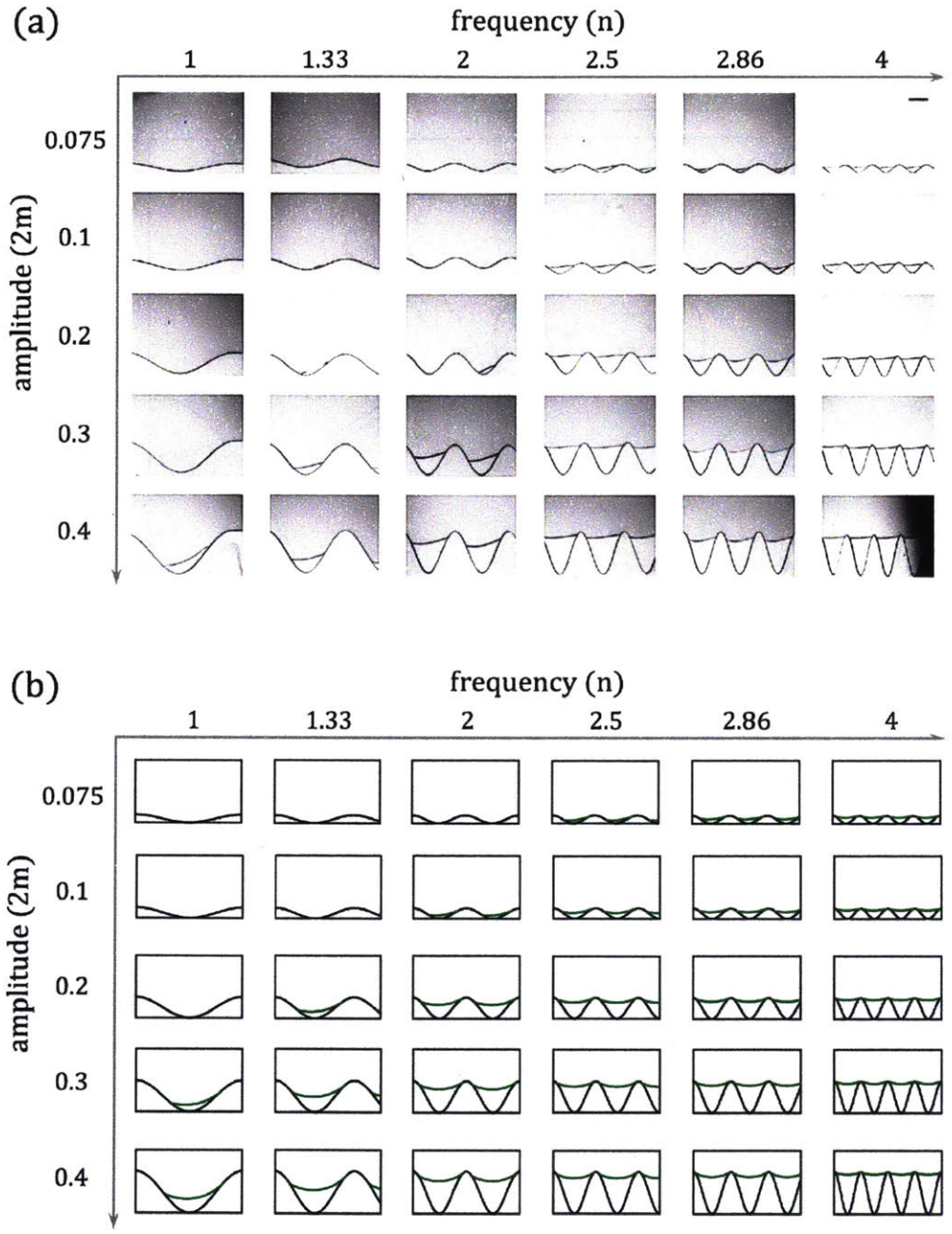

Figure 4-5: (a) Experiment and (b) theoretical results of entrapped oil for a sinusoidal pattern with different values of frequency (n) and amplitude ($2m$). The amount of oil trapped increases with increasing amplitude and frequency. Scale bar in experimental images is 200 μm. Values of $\theta = \frac{25\pi}{180}$ and $\beta = \frac{35\pi}{180}$ were used for theoretical calculations.

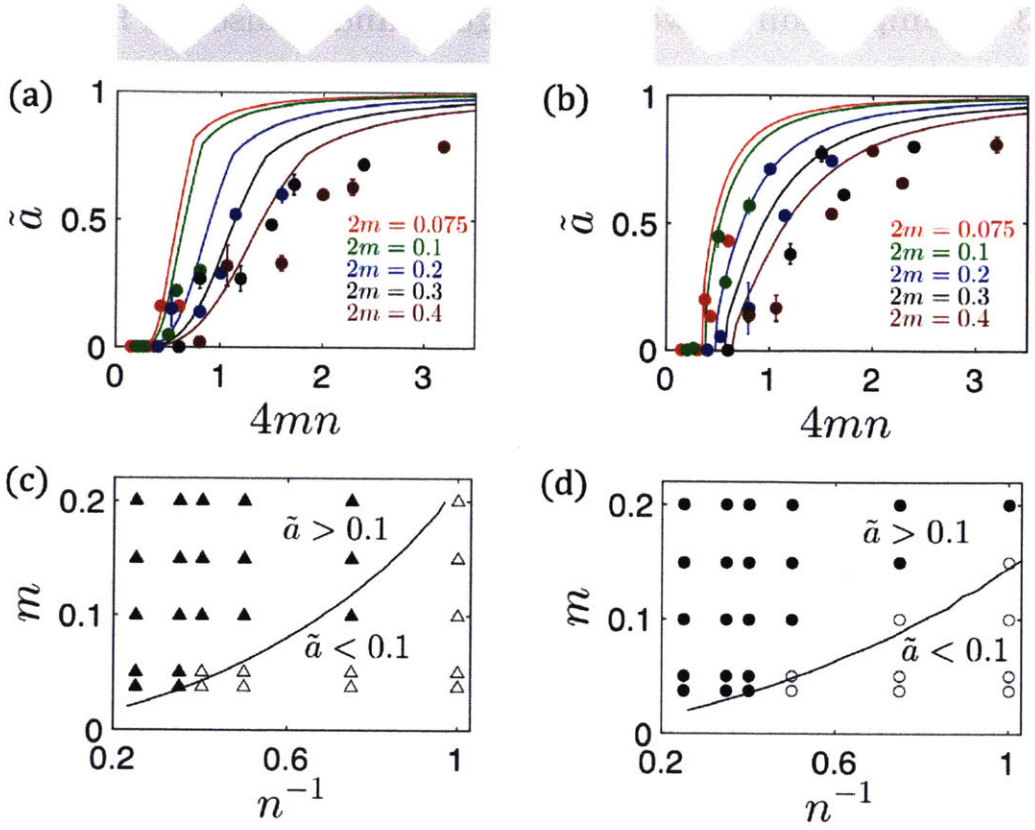

Figure 4-6: Dimensionless amount of oil entrapped for (a) triangular pattern and (b) sinusoidal pattern. The symbols represent experimental data and solid lines represent theoretical calculations. Phase diagram of transition from $\tilde{a} < 0.1$ to $\tilde{a} > 0.1$ for (c) triangular pattern and (d) sinusoidal pattern. Closed symbols represent $\tilde{a} > 0.1$ and open symbols represent $\tilde{a} < 0.1$. The solid line is constructed from numerical calculations.

The above result might appear to be counter-intuitive since it suggests that for higher values of m, a sinusoidal pattern needs larger frequencies to trap oil. However, the transition from no-capture to capture is not a complete metric to compare the entrapment from the two patterns. We thus compare in Fig.4-6 results from experiment and theoretical calculations of dimensionless amount of oil entrapped $\tilde{a}$ for different values of m and n.

4.2.3 Comparison between Triangular and Sinusoidal Patterns

Fig.4-6 (a) summarizes results of $\tilde{a}$ for triangular patterns. The theoretical predictions can be understood from the analysis discussed in Equations (4.13-4.16). $\tilde{a}$ has 4 regimes when plotted with $\tan\alpha = 4mn$, *i.e.* $\tilde{a} \sim 0$, $\tilde{a} \sim m^{-2}$, $\tilde{a} \sim m^{-1}$ and $\tilde{a} \sim 1$. Therefore, once $\tilde{a} > 0$, the amount of oil entrapped is different for different values of m. However, as $4mn$ increases, the difference between different profiles decrease as all of them approach $\tilde{a} \sim 1$. The experimental data qualitatively agrees with our theoretical predictions. Nonetheless there are some quantitative differences for several possible reasons. We ignore the effect of third dimension that plays a role in the shape of interface. As we show in the Appendix, the contact angle observed from the microscope images is dependent on the position inside the triangular pattern, probably because of the curvature effects in the third dimension [116,117]. However, such effects have been currently ignored in the model since we assume θ to be independent of the third dimension. We also assume the system to be quasi-static and ignore the effect of contact angle hysteresis that might alter the evolution of the interface. For instance, in Fig.4-1 (c), during the pinch-off process, the interface readjusts near the point of contact ($t = 0.67s$). We do not account for any preferred values of γ_2 based on surface energies in our model. Lastly, a thin layer of oil that may be deposited in the photopatterned structure can alter the contact angle and surface properties of the structure [107].

Fig.4-6 (b) summarizes results of $\tilde{a}$ for the sinusoidal patterns. There are some similarities and some differences when compared to the triangular pattern. Like the triangular pattern, theoretical profiles $\tilde{a}$ are 0 for low values of $4mn$ (a measure of average slope) but the curves for different values of m do not become non-zero at the same value of $4mn$. This is expected since $n_{\text{crit, theory}} \sim m^{-1}$ doesn't hold for a sinusoidal pattern, as previously discussed. Similar to triangular patterns, for moderate values of $4mn$, different m values yield different $\tilde{a}$ profiles, and for high values of $4mn$ all curves start to approach a limiting value. The experimental data also agrees qualitatively with the theoretical predictions. However, a major difference

in the predicted profiles of the two patterns is that once $\tilde{a} > 0$, sinusoidal patterns display a steep rise in $\tilde{a}$ whereas triangular patterns show a rather gradual rise in $\tilde{a}$. This happens because once the critical condition is reached, the entrapment is significant due to a concave shape in the middle portion of the sinusoidal pattern. This is visually supported upon comparing Fig.4-3 and Fig.4-5 where entrapment is larger for the sinusoidal pattern. This result underscores the need to include the effect of pattern shape to predict the process of entrapment. Moreover, it also shows that looking at the transition from no capture to capture doesn't provide a complete picture.

Fig.4-6 (c, d) show the transition from $\tilde{a} < 0.1$ to $\tilde{a} > 0.1$ for both the patterns. The solid lines in phase diagrams show the minimum value of m for a given n at which the $\tilde{a} = 0.1$. We note that the sinusoidal patterns are able to trap $\tilde{a} = 0.1$ at smaller values of m as compared to triangular patterns. This is consistent with analysis from Fig.4-6 (a, b). Moreover, the value of $a = 0.1$ is just an example and similar phase diagrams can be constructed for other values of $\tilde{a}$. Overall the results from experiments agree with predicted phase diagram.

Our analysis suggests some useful design principles. For applications where one wants to trap a large amount of oil, higher values of mn, lower values of m, and large variations in local slope would be preferred. Though $mn \geq \frac{1}{4}\tan\frac{\theta}{2}$ is derived for a triangular pattern, it may be a good starting point to estimate the overall global slope. Similarly, depending on the desired value of $\tilde{a}$, different values of m can be used. For instance in applications where width is not defined, dynamic length scales controlled by process parameters can provide flexibility to tune the value of m. On the other hand, if we wish to first deposit and then remove a layer of liquid from a patterned surface, the pattern should have lower values of mn, higher values of m, and small variations in local slope.

4.3 Recovery of the Captured Oil as a Potential Application of the Microfluidic Test Platform

It is estimated that more than two third of the initial amount of oil and natural gas in underground reservoirs is not recoverable with current technologies and remained in the reservoirs after the water flooding recovery process. There are many Enhanced Oil Recovery (EOR) processes under development with functional materials and other practices to recover this substantial amount of unrecovered natural resources. Using the periodic patterns in microfludic channels, we demonstrate a model study where we utilize this system as a test platform for EOR research. We present our analysis of the experiment results parallel to computational simulation model and they show good agreement in qualitative trend in their recovery process. This computational model can provide extended insights into the recovery process with parametric study for the cases that are practically difficult to be realized or verified with experiments.

4.3.1 Experiment Setup and Results

After the oil entrapment step, we flood the channel with 5wt% sodium dodecyl sulfate(SDS) aqueous solution with flow speed varying from U = $9 \sim 700$ mm/s (Fig.4-7). The flooding process of water corresponds to the secondary oil recovery process and the SDS flooding corresponds to the enhanced oil recovery(EOR) process that is used in oil recovery sites, respectively.

Except amplitude m and frequency n, dimensionless groups that govern the process are capillary number $\mathrm{Ca} = \frac{\mu_w U}{\sigma}$, Reynolds number $\mathrm{Re} = \frac{\rho_w U H}{\mu_w}$, and viscosity ratio $\lambda = \frac{\mu_o}{\mu_w}$. Based on our experimental conditions, Ca changes from $1.5 \times 10^{-3} - 1.16 \times 10^{-1}$, Re varies between $0.45 - 35$, and λ is constant at unity ($\rho_w = 10^3$ kg/m^3, $\mu_w = 10^{-3}$ Pa.s, $\mu_o = 10^{-3}$ Pa.s, $\sigma \approx 6 \times 10^{-3}$ N/m).

The experimental results for Ca=0.116, Re=35, $m = 0.2$ and $n = 4$ are provided in Fig.4-8. We define dimensionless volume $\tilde{V}$ as the ratio of oil volume inside the trough to the volume of a trough. The $\tilde{V}$ prior to surfactant flood is taken to be $\tilde{V}_i$.

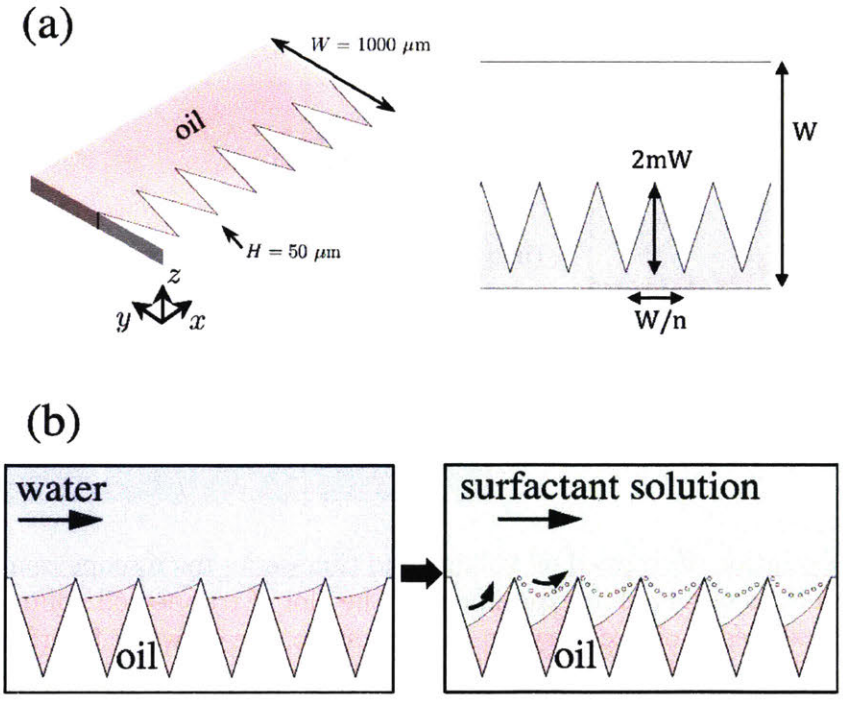

Figure 4-7: Schematic of the setup. (a) A glass microchannel with triangular patterned sidewall, width (W) 1000 μm, and height (H) 50 μm is filled with oil (decane). The triangular pattern is characterized by amplitude $2mW$ and wavelength $\frac{W}{n}$. (b) The oil is displaced with water to trap oil in triangular troughs. Post oil entrapment, the channel is flooded with 5 wt% SDS aqueous solution at different flow rates to recover the oil.

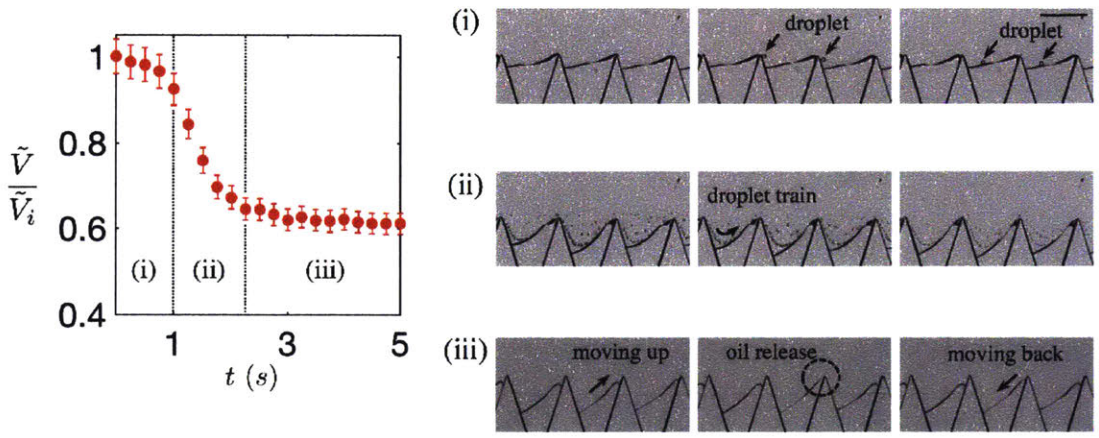

Figure 4-8: Evolution of trapped oil volume and time-series microscope images during surfactant flood, as observed in experiments. The plot of trapped oil volume suggests three different stages of oil recovery. In the first stage, the oil-water interface deforms and moves to the top-right corner. Here, intermittent oil droplets are formed leading to modest recovery. During the second stage, the interface moves downwards at the left edge, rapidly draining the oil in form of a droplet train. In the third stage, interface at right corner slides down and releases oil droplets in a pulsating mode. The pulsating cycle involves the interface moving upwards to the corner followed by oil release and interface moving downwards. Scale bar is 200 μm. Ca= 0.116, Re= 45, $\tilde{V}_i = 0.66$, $m = 0.2$, and $n = 4$.

We find $\tilde{V}_i = 0.66$ from image analysis. The evolution of $\frac{\tilde{V}}{\tilde{V}_i}$ with surfactant flood duration suggests that oil recovery occurs in three phases. During the first phase, the recovery is relatively mild as few droplets of oil are released intermittently while the interface deforms and travels upwards to the top right corner of the triangular trough. The first phase is followed by a period of rapid recovery. We note that the movement of the interface to top right corner is necessary for the second phase to occur. During the second phase, a continuous train of droplets is generated that does not coalesce with the oil trapped downstream. We believe that this occurs due to the repulsive interaction between the surfactant molecules. Microscopic images suggest that the droplet size in the second phase is on the order of $d \sim 10$ μm. Assuming a critical capillary number for $\lambda = 1$ between $\mathrm{Ca_{crit}} = 0.1 - 0.2$ [118], we estimate the droplet size by balancing interfacial stress $\left(\frac{\sigma}{d}\right)$ and shear stress $\left(\frac{3\mu_w U}{H}\right)$, or $d = \frac{\mathrm{Ca_{crit}}\sigma}{\left(\frac{3\mu_w U}{H}\right)} = 14 - 28$ μm, which is in reasonable agreement with the experimental values. The final phase of the process starts when the interface slides down from the top right corner of the trough. In the third phase, we observe a pulsating mode of recovery where some droplets are released periodically. We believe this process is reminiscent to the tip streaming where the surfactant is swept to the tip of the interface, thereby reducing the interfacial tension and creating droplets [119]. Droplet generation in turn decreases the surfactant concentration on the interface and the process repeats once enough surfactant accumulates onto the fresh interface.

4.3.2 Computational Simulation Model and Results

We have a multiphase Volume of Fluid (VOF) model to analyze our system. We assume oil as the first phase with properties ρ_o (density of oil), μ_o (viscosity of oil) and surfactant solution as the second phase with the physical properties similar to water ρ_w (density of water), μ_w (viscosity of water). The interfacial tension between the two phases is defined as σ. The VOF model introduces a new variable ϕ, volume fraction of the oil phase. Volume fraction is the probability of finding the oil phase at

a specific location and thus $0 \leq \phi \leq 1$. A value of $\phi = 1$ would mean the the location is occupied by oil and a value of $\phi = 0$ implies the location is occupied by the aqueous phase. Since the model assumes ϕ as a continuous variable, values between 0 and 1 are also possible, leading to a diffuse interface. Based on ϕ, the model defines the global ρ and μ as follows:

$$\rho = \rho_o \phi + \rho_w (1 - \phi) \tag{4.28}$$

$$\mu = \mu_o \phi + \mu_w (1 - \phi) \tag{4.29}$$

The model solves for $\rho, \mu, \vec{u}, P$ using the following equations:

$$\nabla . \vec{u} = 0 \tag{4.30}$$

$$\frac{\partial \phi}{\partial t} + \vec{u} . \nabla \phi = 0 \tag{4.31}$$

$$\rho \left(\frac{\partial \vec{u}}{\partial t} + (\vec{u} . \nabla) \vec{u} \right) = -\nabla P + \nabla . (\mu S) + f \tag{4.32}$$

$$f = \sigma k \frac{2\rho}{\rho_o + \rho_w} \nabla \phi \tag{4.33}$$

$$k = -\nabla . \hat{n} \tag{4.34}$$

$$\hat{n} = \frac{\nabla \phi}{|\nabla \phi|} \tag{4.35}$$

$$S_{ij} = \frac{1}{2} \left(\frac{\partial u_j}{\partial x_i} + \frac{\partial u_i}{\partial x_j} \right) \tag{4.36}$$

Equation(4.30, 4.31) are equations for overall mass balance and phase mass balance respectively. Equation (4.32) is the momentum conservation equation with an additional force f that takes into account the interfacial force. f is calculated through Equation(4.33) that depends on the curvature k, which in turn depends on ϕ, as shown in Equation (4.34, 4.35). Finite volume software openFoam is used for all computational calculations. The utility *blockMesh* is used to construct and mesh a 3-D geometry that comprises of three triangular troughs in a channel with length $W\left(0.5 + \frac{3}{n}\right)$ (some space is left before and after the troughs). A uniform meshing grid is used with a typical cell size of 12.5 μm. Velocity inlet and pressure outlet conditions are used for inlet and outlet faces, and no-slip condition is used for the walls.

A neutral wetting condition is implemented at walls by assuming a zero gradient for ϕ (see Equation (4.34, 4.35)). We note that in experiments the modified sidewalls show a water-wet behavior after the surfactant flood. However, to simplify boundary conditions, we assume a neutral wetting condition. The VOF equations are solved in an unsteady and laminar environment using the utility *interFoam*.

We present results from our model for the same conditions as experiments *i.e.* Ca=0.116, Re=35, $m = 0.2$, and $n = 4$ in Fig.4-9. For consistency with experiments, we set the initial condition such that $\tilde{V}_i = 0.66$. We also define dimensionless time $\tilde{t} = \frac{tU}{W}$. The results from model display qualitative similarities with experiments. There is an initial period of no recovery where the interface attempts to reach the top right corner. The model also predicts a period of rapid recovery that is characterized by formation of droplets and downward movement of interface at the left edge of the triangle ($\tilde{t} = 0.5$). Lastly, the recovery slows down when the interface slides down from the top right corner ($\tilde{t} = 4.5$). However, there are also some important differences between the results from model and experiments. In the model, we find that the released oil coalesces with the oil trapped in downstream troughs ($\tilde{t} = 1.14, 1.65$), mainly because we do not consider the repulsive interactions between the surfactant molecules (the results of $\frac{\tilde{V}}{\tilde{V}_i}$ in Fig.4-9 are thus plotted only for the left-most trough to exclude the effect of coalescence). Also, though the kinetic variation of $\frac{V}{V_i}$ is qualitatively similar, the time scales differ by almost two to three orders of magnitude. $\tilde{t} = 10$ corresponds to $t = 0.014$ s whereas we observe changes on the order of a few seconds in experiments. We also do not observe intermittent or pulsating droplet generation. We attribute the above discrepancies to the lack of surfactant transport in our model. In the actual experiments, the interface is initially free of surfactants, and thus there is a time scale associated with surfactant transport and eventual decrease in interfacial tension. In contrast, in the model, we set the Ca by the equilibrium interfacial tension, thereby predicting a much shorter time scale of droplet breakup. Several studies have theoretically discussed the effect of surfactant transport during droplet deformation [119–121]. Unfortunately, the theoretical equations discussed in these reports aren't compatible with the VOF framework and are thus beyond

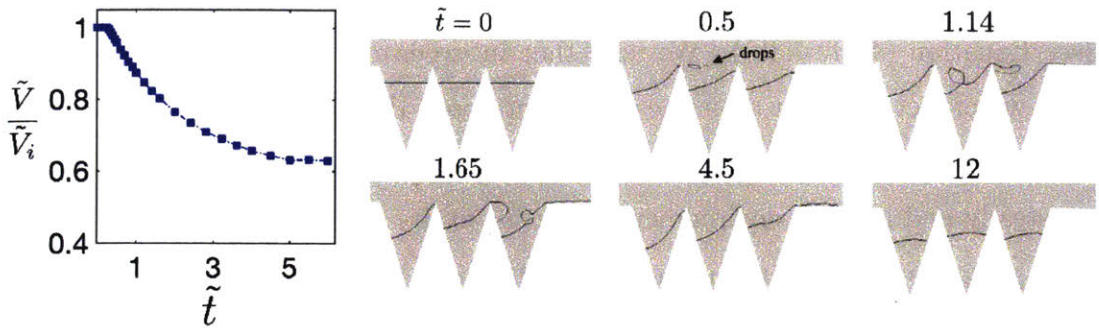

Figure 4-9: Evolution of trapped oil volume (values taken from left most trough only) and snapshots of $\phi = 0.5$ contours in the computational model. We observe similar qualitative behavior when compared to experiments i.e. a minor lag in initial recovery until the interface reaches the top right corner followed by a rapid recovery of oil. The model yields small oil pockets ($\tilde{t} = 0.5$) but the droplets merge into the downstream trough ($\tilde{t} = 1.14$), unlike experiments. This occurs due to absence of surfactant interactions in the model. The rapid recovery phase continues until the interface from top-right corner slides down ($\tilde{t} = 4.5$ for left most trough). Ca= 0.116, Re= 45, $\tilde{V}_i = 0.66$, $m = 0.2$, and $n = 4$.

the scope of this work. However, previous studies help us understand the pulsating mechanism of droplet generation *i.e.* surfactant convects and accumulates towards the tip of the droplet leading to a droplet breakup. Once the droplet breaks, the interface readjusts and the process repeats itself.

4.3.3 Effect of capillary number

We analyze the effect of Ca on the oil recovery process in Fig.4-10. We compare the final values of $\tilde{V}$, referred here as $\tilde{V}_f$, for different Ca (Fig.4-10 (a)). Both experiments and model show no oil recovery for Ca ≤ 0.025. This is consistent with expectation since interface isn't able to reach the top right corner, a necessary condition to start the second recovery phase. In fact, for Ca $= 0.0015$, we obtain a symmetric interface, in agreement with the understanding that for low Ca interface isn't perturbed by shear forces and minimizes its surface area (Fig.4-10 (b)). On the other hand, at Ca $= 0.025$, we find that the interface is asymmetric and has deformed due to shear forces. For both Ca $= 0.0375$ in model and Ca $= 0.075$ in experiments, we observe that interface just reaches the top right corner, releasing some oil. This is slightly

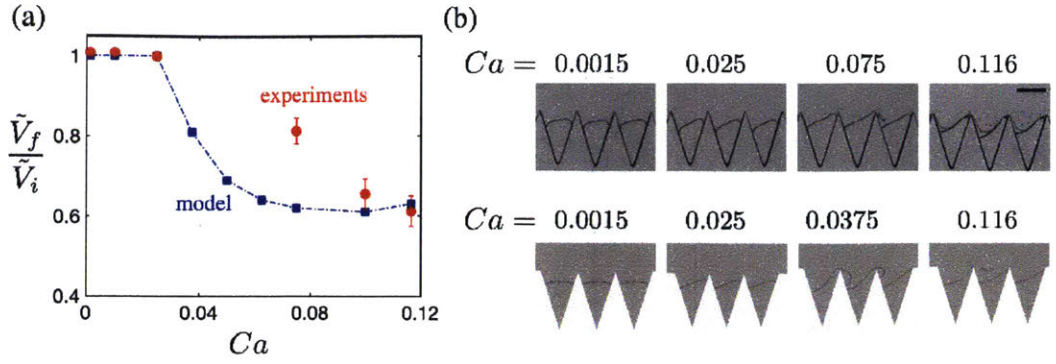

Figure 4-10: Effect of Ca. (a) Variation of final trapped oil volume with capillary number. (b) Representative snapshots of interface from experiments (top) and contours of $\phi = 0.5$ from model (bottom). We observe qualitative agreement between experiments and simulation. For $Ca \leq 0.025$, we do not observe any oil recovery. We note that there is some interface deformation at $Ca = 0.025$ but that is not sufficient for the interface to reach the top right corner. For $Ca = 0.075$ in experiments and $Ca = 0.375$ in model, we report moderate recovery where droplets are formed but not continuously. At $Ca = 0.116$, both experiments and model yield a continuous stream of oil release leading to appreciable recovery. We note that final trapped oil volume becomes relatively constant upon increase in Ca. Scale bar is 200 μm, $\tilde{V}_i = 0.66$, $m = 0.2$, and $n = 4$.

different than Ca = 0.116 where we see a more continuous stream of droplets. We note that the values of $\tilde{V}_f$ from experiments and model at large Ca values are in reasonable agreement. Moreover, for large Ca values, $\tilde{V}_f$ starts to become relatively constant, suggesting that the limiting value is governed by the geometry of the trough.

4.3.4 Effect of geometry

To explore the effect of geometry on $\tilde{V}_f$, we varied $\tilde{V}_i$ in our model, a parameter that cannot be controlled in experiments. The results are provided in Fig.4-11 (a). Oil recovery starts at smaller Ca for larger $\tilde{V}_i$ since lower deformation is required to move the interface towards top-right corner. However, at larger Ca, the final recovery is independent of initial condition. Therefore, it is clear that geometry plays an important role in determining the $\tilde{V}_f$ at large Ca, or $\tilde{V}_{f,\infty}$. We note that $1 - V_{f,\infty}$ is a measure of maximum oil recovery. As discussed previously, the critical condition for third phase of recovery is the downward movement of interface from the top right

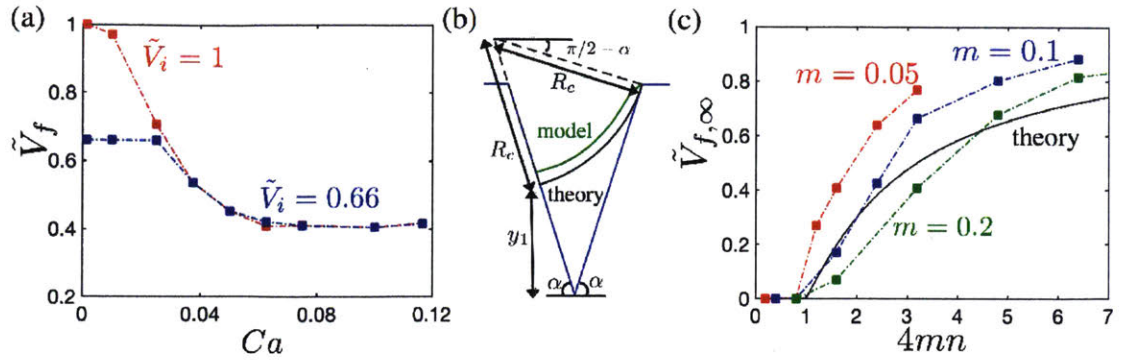

Figure 4-11: Effect of initial condition and geometry. (a) Variation of final trapped oil volume with Ca for different $\tilde{V}_i$. We find that irrespective of the initial condition, final volume at large Ca is same i.e. $V_{f,\infty}$. (b) A simple theoretical setup to predict dependence of $V_{f,\infty}$ on geometry. We approximate the interface just before it slides down the top right corner as a circular arc that touches the right triangular corner and is normal to the left edge. The calculations show reasonable agreement between the theoretically predicted arch and the contours of $\phi = 0.5$ (results shown for $m = 0.2$, $n = 4$). (c) Effect of geometry on $V_{f,\infty}$. We report that after a critical point, $V_{f,\infty}$ increases with $4mn$. Though the theory is able to capture the basic variation, it is unable to quantitatively capture the effect of confinement.

corner.

To provide an estimate of $\tilde{V}_{f,\infty}$, we assume a circular interface that is normal to the left edge of the triangle and that touches the top right corner. The assumption of circular interface isn't perfectly valid since shear forces are not negligible when compared to interfacial forces. However, since the velocity magnitudes in trough are smaller than the bulk of the microchannel, it is a reasonable first order approximation. In model, at the critical condition, the interface changes its curvature near the top right corner and becomes parallel to the flow direction. However, the change in curvature is currently ignored for sake of simplicity. We define the trough angle α through $\tan\alpha = 4mn$ (Fig.4-11 (b)). We can also write the following equations:

$$y_1 + R_c \sin\alpha = 2m + R_c \cos\alpha \tag{4.37}$$

$$R_c \cos\alpha + \frac{y_1}{\tan\alpha} + \frac{1}{2n} = R_c \sin\alpha \tag{4.38}$$

Upon simplification of Equation (4.37 - 4.38), we get:

$$y_1 = 2m \tan(\alpha - \pi/4) \tag{4.39}$$

Equation (4.39) shows that $y_1 \leq 0$ for $\alpha \leq \frac{\pi}{4}$. Thus there won't be any capture for $\tan\alpha = 4mn \leq 1$. To calculate the $\tilde{V}_{f,\infty}$ approximately, we can calculate the volume of the prism formed by the end of the arc, or:

$$\tilde{V}_{f,\infty} \approx \frac{\frac{1}{2} \times y_1 \times \frac{2m}{\sin\alpha} \times \sin(\pi - 2\alpha) \times HW^2}{m/n \times HW^2} \approx \sin\alpha \tan(\alpha - \pi/4) \tag{4.40}$$

We plot the results of Equation (4.40) in Fig.4-11 (c) and compare them with the results of the model. We find theoretical calculations yield a qualitatively similar trend where there is no oil trapped for $\tan\alpha = 4mn \leq 1$ and $\tilde{V}_{f,\infty}$ increases with increase in $4mn$. However, the model predicts a dependence on m whereas the theory predicts that confinement will not play a role. This discrepancy occurs because in our theory we neglect the effect of difference in flow patterns for different values of m. Our theoretical results are closer to values of $m = 0.1, 0.2$ from the model since the assumption of circular interface is more likely to be followed in deeper troughs where local Ca is lower. Nonetheless, Equation (4.40) provides a quick and easy way to predict the amount of oil recovery possible for different geometries. We emphasize that $1 - V_{f,\infty}$ is a measure of maximum oil recovery. For $\alpha = \frac{\pi}{3}$ and $\alpha = \frac{5\pi}{12}$, $1 - V_{f,\infty}$ is estimated to be 0.77 and 0.44 respectively. Therefore, a modest increase in α leads to a drastic reduction in oil recovery. We note that though the actual geometries might not be as simple as a triangular trough, a global slope of the geometry can be used as $\tan\alpha$ in Equation (4.40).

4.4 Summary

In this chapter, we discussed the process of liquid entrapment by sequential injection of immiscible liquids. We experimentally photopatterned triangular and sinusoidal

structures with different dimensionless amplitudes m and dimensionless frequencies n, and built a quasi-static model that predicts the process of entrapment by approximating the interface as a circular arc. Our experimental and theoretical results are in good agreement and our analysis highlights the importance of including the shape of the pattern in understanding the entrapment process. Specifically, we discuss using global slope mn, dimensionless amplitude m, and shape of pattern as design principles to control the entrapment process. Using this microfluidic platform, we also demonstrated oil recovery model study with surfactant solution flooding. We experimentally and theoretically investigated the release of trapped oil in triangular trough during a surfactant flood. Our experiments showed three stages of recovery where the second stage displayed the majority of oil recovery. Our computational method was able to capture the dominant physics but was unable to capture the intermittent droplet formation due to lack of surfactant transport. We reported that a critical capillary number is required for the oil to be recovered but at the same, oil recovery saturates at large capillary numbers. We believe this oil recovery model study with artificial dead-end pores can be studied further with respect to the effects of surfactant transport at the interface, the accumulation of surfactant molecules at the interface and the oil release, changes in oil solubility and wetting condition as the surfactant solution is gradually introduced to the oil-water system.

We believe our work can be useful for several applications. In oil recovery and soil remediation research, our platform can be used to quantitatively investigate the effect of shape of surface on enhanced oil recovery, and to rapidly screen chemicals that are successful in removing a trapped layer of oil. The effect of wetting in oil recovery can also be explored by combining experimental and theoretical research. Researchers interested in parallel experimentation for diagnostic research may also find this platform useful for creating several isolated aqueous pockets. Moreover, our platform can be easily adapted for large scale phtopatterning and advanced microscopy techniques that allow this platform to be used for existing material synthesis methods [122]. or applications in designing liquid infused surfaces, our results could provide design principles for successful entrapment of liquid layers. Understanding

the effect of surface shape and amplitude of pattern on entrapment can also help research in the areas of fiber coating and gravure printing processes where dynamic length scales are involved [108–110]. Lastly, we hope that our results will help the researchers building models for porous media flows using first principles to include the surface shape in their models [123, 124].

Chapter 5

Site-Selective In Situ Grown Calcium Carbonate Micromodels with Tunable Geometry, Porosity, and Wettability

Micromodels are artificial transparent porous media that provide direct visualization of a complex flow environment and can be modified to affect porosity, permeability, or wettability. Micromodels have been increasingly used to understand multiphase fluid behaviors and interactions among oil-water-rock phases in underground oil reservoirs. Researchers have recently developed synthetic micromodels through top-down and bottom-up approaches. Various fabrication methods combined with top-down etching or lithographic techniques can achieve geometric representation of the reservoir pores. There have also been significant improvements in post-treatment methods to modify wettability within micromodels to mimic the reservoir's wettability. Previous micromodels have mostly been made of glass, [26] silicon, [25, 61] and polymeric materials [21, 29, 31–33, 62, 63, 113] instead of real rock. [125, 126] As a result, they have limitations in studying geochemical fluid-rock interactions, such as acid fracturing to increase the oil production from carbonate reservoirs [127] or changes in wettability due to aging or adsorption of molecules added during simulated enhanced oil recovery. Features have been wet etched [125] and laser machined [126] directly into rock samples and then sealed to make micromodels. These top-down approaches

result in large ($\tilde{1}00$ μm) and relatively simple features. By comparison, microporosity (pore throats and channels < 10 μm) comprises up to 50% of the total porosity in the Ghawar Arab-D carbonate reservoir (the largest collection of carbonate reservoirs in the world) and critically affects the oil recovery. [57, 128] A simple and controllable method that enables creation of patterned, large-area real-rocks with smaller pore-length scales in the microfluidic channels is thus a desirable goal.

Bottom-up strategies inspired by biomineralization have received special attention as a key technology to understand formation mechanism of inorganic materials in nature and to prepare precipitations in synthetic systems. [129–132] There have been reports on the fabrication of complex carbonate structures via organic templates and a wide range of synthetic methods such as vapor [133–141] or double diffusions, [142] and Kitano methods. [143] Most bottom-up fabrication methods involve both homogeneous and heterogeneous nucleation, and growth processes in solutions and on templates, which result in inevitable problems of undesirable mineralization on channel walls and blocking of the channel. [144–146] For these reasons, the previous methods cannot be applied to fabricate carbonate micromodels with complex features. In addition, preparing the template fully covered with carbonate requires an additional nucleation process and long process time because negatively charged organic molecules (e.g., acidic polymers) of the template can act as inhibitors of mineral deposition. [147–149]

Simplified porous microfluidic systems are widely used to mimic the underground oil-reservoir environment for multi-phase flow studies, enhanced oil recovery, and reservoir network mapping. However, previous micromodels have been mostly made of polymeric materials, silicon, or glass. As a result, they have limitations in studying geochemical fluid-rock interactions, such as acid fracturing to increase the oil production from carbonate reservoirs or changes in wettability due to aging or adsorption of molecules added during simulated enhanced oil recovery. To overcome this limit, we developed a simple method to create micromodels composed of in situ grown carbonate rocks based on the previously developed photopatterning structuring technique. Carbonate seed particles/hydrogel composite microstructures were built in microflu-

idic channels by photopatterning, and carbonate rocks were selectively grown in situ from these microstructures by supplying Ca^{2+}, CO_3^{2-} rich, supersaturated solutions. This approach enables us to fabricate synthetic carbonate reservoir micromodels having dynamically tunable geometries with submicrometer pore-length scales with controlled wettability. Using this new method, we demonstrate acid stimulation and an immiscible fluid displacement process used in real oil field applications to visualize pore-scale fluid-carbonate interactions in real time.

Here a simple method is introduced to create calcium carbonate ($CaCO_3$) micromodels composed of in situ grown $CaCO_3$. To induce the selective and efficient growth of calcium carbonate within our templates, we eliminated the need for a nucleation step by blending carbonate seed crystals into the non-charged polymeric template. $CaCO_3$ nanoparticles/polymer composite microstructures are built in microfluidic channels by photopatterning, and $CaCO_3$ nanoparticles are selectively grown in situ from these microstructures by supplying Ca^{2+}, CO_3^{2-} ions rich, supersaturated solutions. This approach enables us to fabricate synthetic $CaCO_3$ reservoir micromodels having dynamically tunable geometries with submicrometer pore-length scales and controlled wettability. Using this new method, acid fracturing and an immiscible fluid displacement process are demonstrated used in real oil field applications to visualize pore-scale fluid-carbonate interactions in real time.

5.1 Photo-patterning $CaCO_3$ Nanoparticles/Polymer Composite Microstructures

Creating a micromodel with calcium carbonate/polymer composite microstructures can be largely divided into two parts (Fig.5-1 (a)). The first key part is microstructure synthesis in initially empty microfluidic channels using microscope-based photolithography. [78, 113] The surface of the glass microchannel was treated with 3-(trimethoxysilyl)propyl acrylate to fix the polymerized structures on the top and bottom surfaces of the microchannel. In parallel, we ultrasonicated aqueous precursor

solutions containing a crosslinker (poly(ethylene glycol) diacrylate), a photo-initiator, a porogen (poly(ethylene glycol)), and $CaCO_3$ (calcite) nanoparticles. A homogeneous dispersion was needed to reduce the light scattering during UV exposure, and the porogen was added to facilitate the fast diffusion of ions into the polymerized structure. Calcite nanoparticles were used as seed crystals because of their polymorphic stability and well-known growth mechanisms. [150] The well-dispersed precursor solutions were injected into the acrylate-functionalized microchannel, followed by UV photolithography using a photomask containing desired geometric shapes inserted into the field stop of an inverted microscope. After synthesizing microstructured posts, any uncured precursor solution was washed out of the microchannel with deionized water. The top-view optical microscopy image of the photopatterned posts showed homogeneous $CaCO_3$/polymer composite microstructures with sharp edges (Fig.5-1 (b)). In contrast, other procedures produced aggregated $CaCO_3$ seeds in the precursor solutions, resulting in diffuse edge features and larger diameter of the post due to light scattering during UV-polymerization.

5.2 Selective Growth of Photopatterned $CaCO_3$ with Ca^{2+}, CO_3^{2-} Ions Rich, Supersaturated Solutions

The selective $CaCO_3$ growth on the posts is based on the biological strategy using Ca^{2+}, CO_3^{2-} ions in a supersaturated solution. A key advance in extending this $CaCO_3$ growth technique to create high quality $CaCO_3$ micromodels is the sustenance of the solution stability by supplying fresh solutions with fixed ionic composition ratios and frequent replacement, providing uniform $CaCO_3$ growth only in and on the posts. After building microstructured posts, any uncured precursor solution was washed out of the microchannel with DI water. Ca^{2+}, CO_3^{2-} ions rich/supersaturated solutions were prepared by the dropwise addition of 100 mL of sodium bicarbonate solution (40 mM) to 100 mL of calcium chloride solution (1.6 mM). The solutions were injected

into the as prepared microchannel with the constant inlet pressure and alternate directions, which were replaced fresh ones every 30 min. The reaction was achieved under relatively high (40 °C) temperature, which was chosen based on experimental optimization. Spontaneous precipitation occurs when solutions are not replaced frequently, which leads to unwanted precipitation of $CaCO_3$ on the microchannel wall. The stability of the supersaturated solution was confirmed by measuring pH. These results indicate that the fast and selective growth of $CaCO_3$ required providing well-controlled supersaturated solutions.

Fig.5-1 (c) shows the top-view optical microscopy image of $CaCO_3$/polymer composite microstructures after $CaCO_3$ growth by using the optimized supersaturated solution for 1h. Changes in the color and size of each post indicate the both inner and outer growth of $CaCO_3$. In addition, the composite post shows axisymmetric shell structures as found by spatial scans with confocal Raman spectroscopic imaging (Fig.5-1 (d), (e)) revealing the distribution of $CaCO_3$, organic, and water. The intensity of $CaCO_3$ is higher at the edge than in the inner parts of the posts, irrespective of z-section planes, which is consistent with the selective growth of $CaCO_3$ on the composite posts. Scanning electron microscopy (SEM) images show the growth of the CaCO3 seed particles on the post surface (Fig.5-1 (f-h)). The initial $CaCO_3$ particles were locally exposed at the surface of the composite posts, but after growth for 1h, the post surfaces were fully covered with $CaCO_3$ particles. As the growth time increases, the size of the particles increases, which results in the increase in the diameter of the composite post. Crystals grown in our conditions have well-defined facets and smooth surface features, displaying equilibrium polyhedral (rhombohedral) morphologies. Also, the polymorph of CaCO3 was confirmed as calcite by X-ray diffraction (XRD) patterns and a Raman spectrum. (Fig.5-2) No characteristic peak from other phases of $CaCO_3$ is found, suggesting that the $CaCO_3$ is totally composed of calcite crystals throughout the growth period.

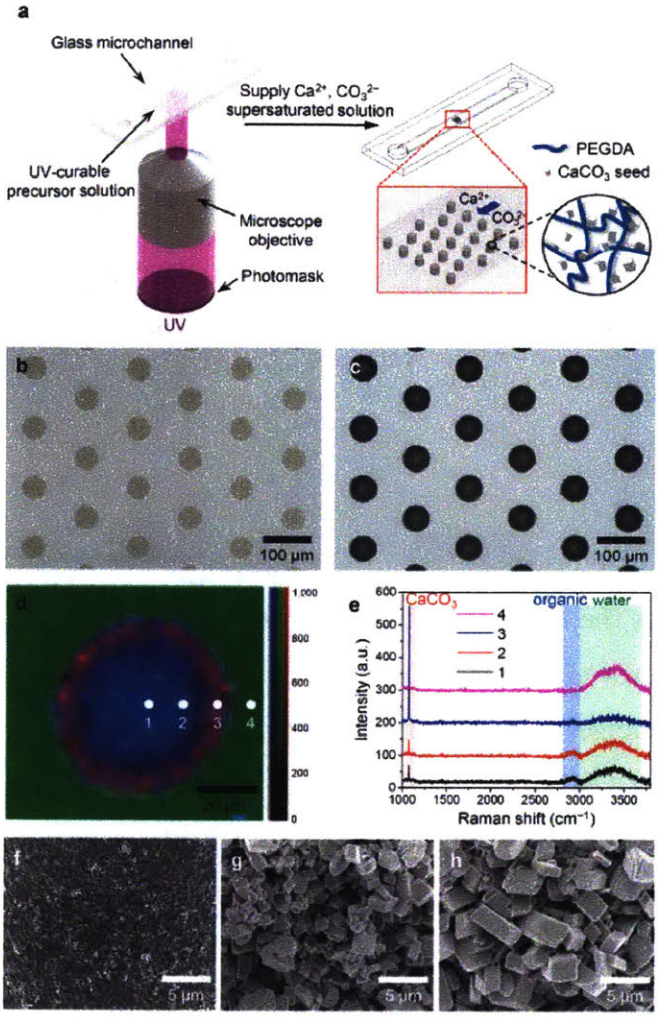

Figure 5-1: Design of mimicking rock micromodels. (a) Schematic illustration showing the photolithographic patterning and the subsequent in situ growth of the $CaCO_3$. (b,c) Top-view optical microscopy images of $CaCO_3$/polymer composite microstructures before (b) and after (c) growth of the $CaCO_3$ with supplying Ca^{2+}, CO_3^{2-} ions rich/supersaturated solutions. (d,e) Raman mapping (d) and spectrum (e) of the composite post of (c) with different positions (1-4) obtained by integrating over the wavenumber ranges of $CaCO_3$ (1,050-1,150 cm^{-1}, red), organic (2,800-3,000 cm^{-1}, blue), and water (3,000-3,700 cm^{-1}, green), respectively. Mapping data were normalized to the strongest intensity of the $CaCO_3$. At the position of 3, the intensity of $CaCO_3$ was maximized and the intensities of others were reduced by the growth of $CaCO_3$. (f-h) SEM images of the outer side surface of the composite posts with different growth time; (f), (g), and (h) indicate 0, 1, and 2 h, respectively. Reprinted with permission from Seung Goo Lee, Hyundo Lee, Ankur Gupta, Sehoon Chang, Patrick S. Doyle. "Site-Selective In Situ Grown Calcium Carbonate Micromodels with Tunable Geometry, Porosity, and Wettability." Advanced Functional Materials 26.27 (2016): 4896-4905. Copyright 1999-2017 John Wiley & Sons, Inc.

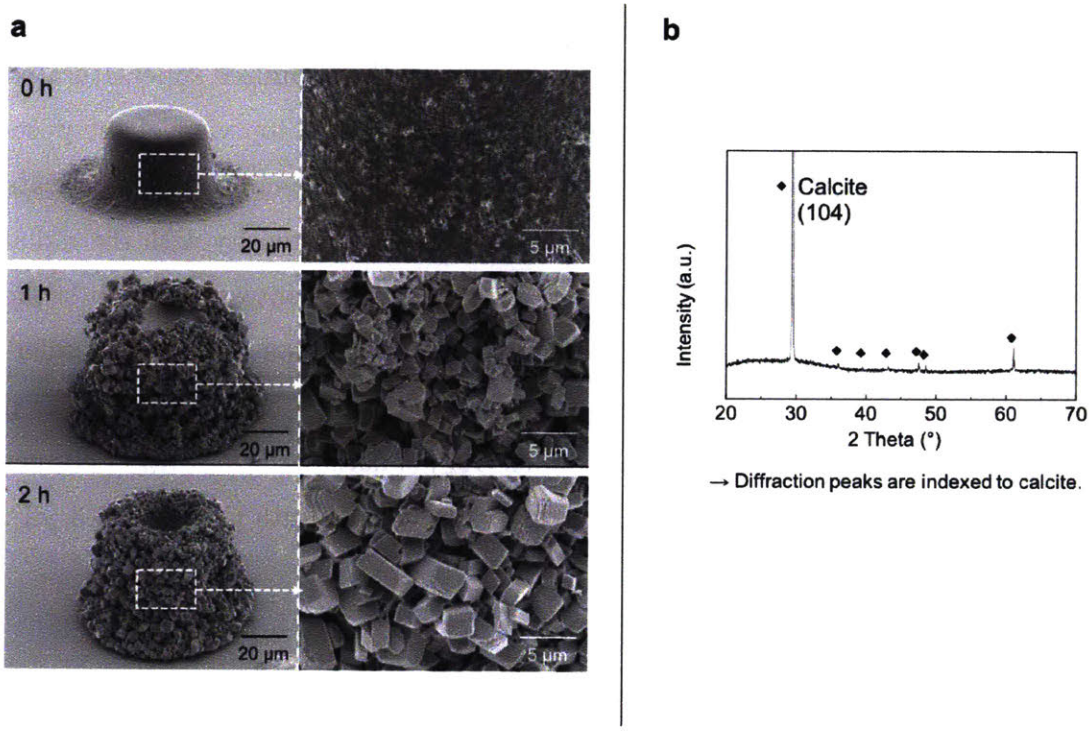

Figure 5-2: (a) Scanning electron microscopy (SEM) images of the outer surface of the composite posts. SEM images show the growth of the $CaCO_3$ seed particles on the post surface. The initial $CaCO_3$ particles were locally exposed at the surface of the composite posts, but after growth for 1h, the post surface was fully covered with $CaCO_3$ particles. As they were grown further, the size of the calcium carbonate particles increase, that results in the increase in the diameter of the composite post. (b) X-ray diffraction (XRD) spectra of the composite posts after growth. The polymorph of $CaCO_3$ was confirmed as calcite by XRD patterns.

5.3 Outward and Inward $CaCO_3$ Growth of the Composite Microposts

In addition to photopatterning, controlling the $CaCO_3$ growth of the composite microposts is important to tune the geometry of micromodels. To quantify the growth rate of the $CaCO_3$, we investigated the change in the dimension of two different sizes of single microposts as a function of the growth time using the optimized supersaturated solution. Inverse monochrome optical microscopy images from top view of the posts are shown in Fig.5-3 (a) where bright areas of the optical microscopy images indicate in situ grown $CaCO_3$. Fig.5-3 (b) shows the variation of the intensity with the radial distance where one can observe that there is inward as well as outward growth of the $CaCO_3$/polymer composite posts. We recognized that there is a mechanistic difference between the inward and the outward growth since though the distance between the initial post radius (R_0) and the inner radius (R_{in}) of dark part ($R_0 - R_{in}$) becomes constant very quickly, outer post radius (R_{out}) varies linearly with time (Fig.5-3 (c)).

5.3.1 Outward $CaCO_3$ Growth

The outward growth of $CaCO_3$ happens through the precipitation of fresh ions on the outer layer of the post. Therefore, the outward growth can be approximated as a surface reaction. Since convection, diffusion and reaction occur simultaneously in this process, it is important to understand the relative importance of these phenomena. For the sake of simplicity, we assumed that mass transfer coefficient is infinity or the concentration of ions on the post surface is the same as the fresh ion concentration *i.e.* $[Ca^{2+}]_0$ and $[CO_3^{2-}]_0$. With this assumption, we were able to predict the mass balance equation:

$$\frac{R_{out}}{dt} = \frac{k''([Ca^{2+}]_0[CO_3^{2-}]_0 - K_{SP}/f_D^2)}{\rho_{CaCO_3}} \tag{5.1}$$

where k'' is the surface reaction rate constant, ρ_{CaCO_3} is the molar density of

$CaCO_3$, K_{SP} is its solubility product constant, and f_D is the activity coefficient for divalent ions. This relationship predicts the growth rate of R_{out} for $CaCO_3$ as a function of $[Ca^{2+}]_0$ and $[CO_3^{2-}]_0$ concentrations, and allows us to quantitatively determine how the performance of the system depends on the supersaturated solutions. Upon substituting the known values of $k'' = 2.32 \times 10^{-4}\ m^4 mol^{-1} s^{-1}$, $[Ca^{2+}] = 0.57 \times 10^{-3}$ M, $[CO_3^{2-}] = 0.33 \times 10^{-3}$ M, $\rho_{CaCO_3} = 27.1\ molL^{-1}$, $K_{SP} = 3.14 \times 10^{-9}$ M^2 and $f_D = 0.561$, we obtain a theoretically predicted growth rate of 5.5 $\mu m/hr$. The predicted rate is very close to the experimentally observed value of 4.8 $\mu m/hr$. Also, experiments are consistent with the prediction of Equation (5.1) that growth rate remains the same regardless of post size (Fig.5-3 (c)).

5.3.2 Inward $CaCO_3$ Growth

Unlike the outward growth, the mechanism of the inward growth of CaCO3 can be quantitatively predicted by relating the reaction time scale to the diffusion time scale. Since the crystal seeds are distributed uniformly inside the posts, inward growth of $CaCO_3$ can be approximated as a volumetric reaction. Hence, we can define Dahmköhler number as:

$$Da = \frac{k'''[Ca^{2+}]_0 R_0^2}{D_{ion,post}} \tag{5.2}$$

where k''' the volumetric rate constant, $[Ca^{2+}]_0$ is the concentration of fresh calcium ions and $D_{ion,post}$ is the diffusivity of ions inside the post. The values of $k''' = 3.66 \times 10^5\ Lmol^{-1}$ and we assumed that diffusivity of ions in the post will be on the same order of magnitude as diffusivity of ions inside aqueous medium or D $10^{-9}\ m^2 s^{-1}$. Upon substituting the values of $k''' = 3.66 \times 10^5\ Lmol^{-1}$, $D \sim 10^{-9}$ $m^2 s^{-1}$, $[Ca^{2+}] = 0.57 \times 10^{-3}$ M, $R_0 = 25$ or 50 μm, we find that $Da \gg 1$ for both the small and large posts. Hence, reaction will dominate the process and ions will be present only in the boundary layer region with thickness given by $\delta \sim \frac{R_0}{\sqrt{Da}}$ or:

$$\delta \sim \sqrt{\frac{D_{ion,post}}{k'''[Ca^{2+}]_0}} \tag{5.3}$$

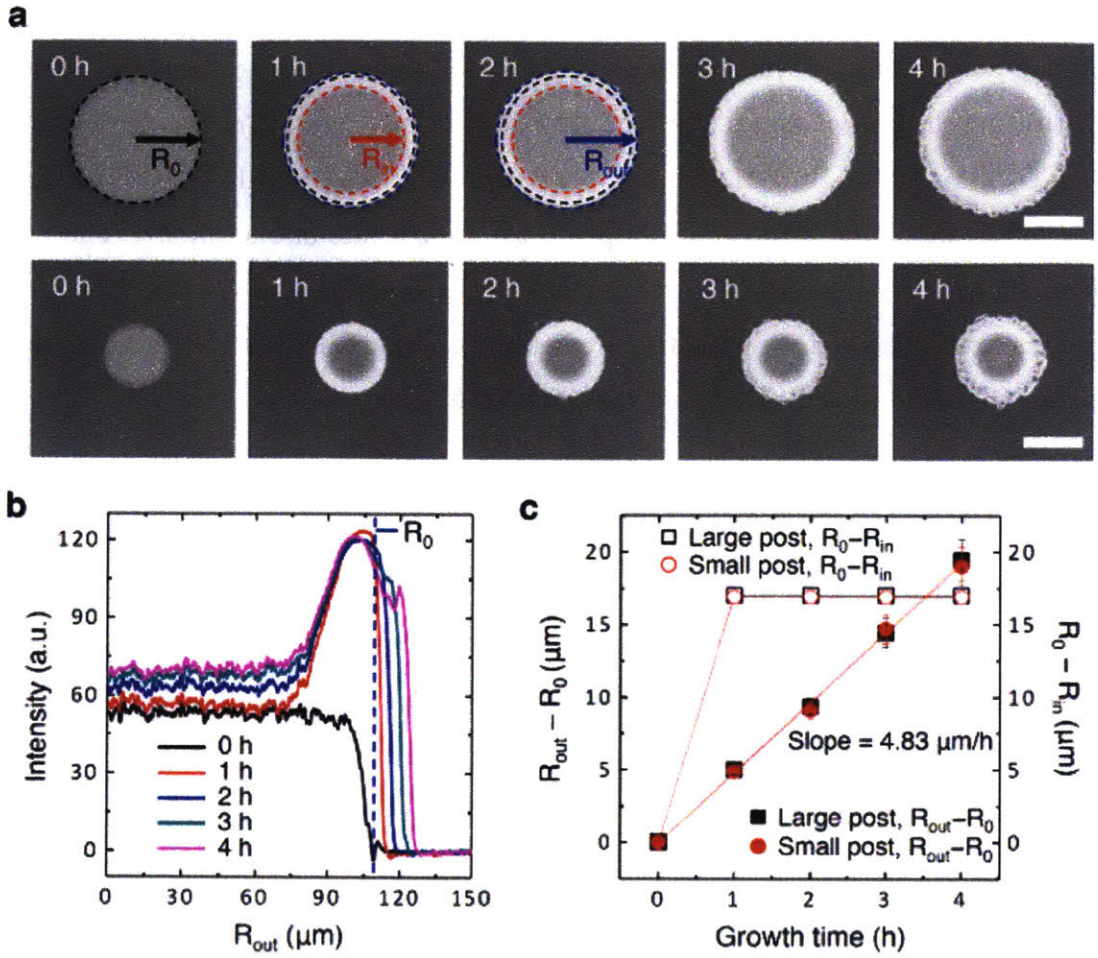

Figure 5-3: In situ growth of $CaCO_3$ posts. (a) In situ optical microscopy images of $CaCO_3$/polymer composite posts in the channel versus growth time. R_0, R_{in}, and R_{out} indicate the initial radius, the inner radius of the dark part, and the outer radius of the posts, respectively. All the scale bars are 100 μm. (b) Gray intensity profiles (a.u.= arbitrary units) taken across centered regions of the large post with the different growth time. The blue dashed line indicates R_0. (c) The changes in $R_{out} - R_0$ (black solid square: large post, red solid circle: small post) and $R_0 - R_{in}$ (black open square: large post, red open circle: small post) as a function of the growth time. Reprinted with permission from Seung Goo Lee, Hyundo Lee, Ankur Gupta, Sehoon Chang, Patrick S. Doyle. "Site-Selective In Situ Grown Calcium Carbonate Micromodels with Tunable Geometry, Porosity, and Wettability." Advanced Functional Materials 26.27 (2016): 4896-4905. Copyright 1999-2017 John Wiley & Sons, Inc.

This simple expression predicts $\delta \sim 2.2\ \mu m$ which is on the same order of magnitude as the experimentally observed value of $R_0 - R_{in}$ of 17 μm. Further, since the system is diffusion limited, the boundary layer thickness would be the same irrespective of the post size. This is also reflected in Equation (5.3) and also observed experimentally (Fig.5-3 (c)). Finally, the time scale for the boundary layer to develop is given by the diffusion time scale $t_D \sim \frac{R_0^2}{D_{ion,post}}$. Upon substitution, t_D is 10 s for large posts. Even if the post size is as long as the channel width (1 mm), t_D is no more than 5 min. Hence, we did not see a change in $R_0 - R_{in}$ as a function of time in Fig.5-3 (c).

We investigated the effect of $R_0 - R_{in}$ and the rate of change in $R_{out} - R_0$ with the concentration of supersaturated solutions related to the reaction rate (Fig.5-4). When we reduced the concentration of both $CaCl_2$ and $NaHCO_3$ solutions by half to 0.8 mM and 20 mM, $R_0 - R_{in}$ increased to 25 μm from 17 μm. This change occurs because when the ionic concentration is reduced to half, the boundary layer thickness increases by a factor of $\sqrt{2}$ (Equation (5.3)). Also, the rate of change in $R_{out} - R_0$ decreased four-fold to 1.2 $\mu m/h$ from 4.8 $\mu m/h$ as predicted by Equation (5.1). Hence, we demonstrate an ability to predict and control the inward and outward growth rates of $CaCO_3$ in a single post.

5.4 Sub-micrometer Scale Porosity Control Ability of the Method

Controlling geometries to submicrometer pore-length scales, particularly those with photolithography and etching, has proved difficult by using conventional methods for micromodels. Tuning porosity and permeability, which are sensitive to changes in micromodel geometry, notoriously requires restructuring of intricate topographical elements that are hard to change. Polymeric micromodels show more promise in terms of restructuring geometry by using additional lithographic process, notably, but they

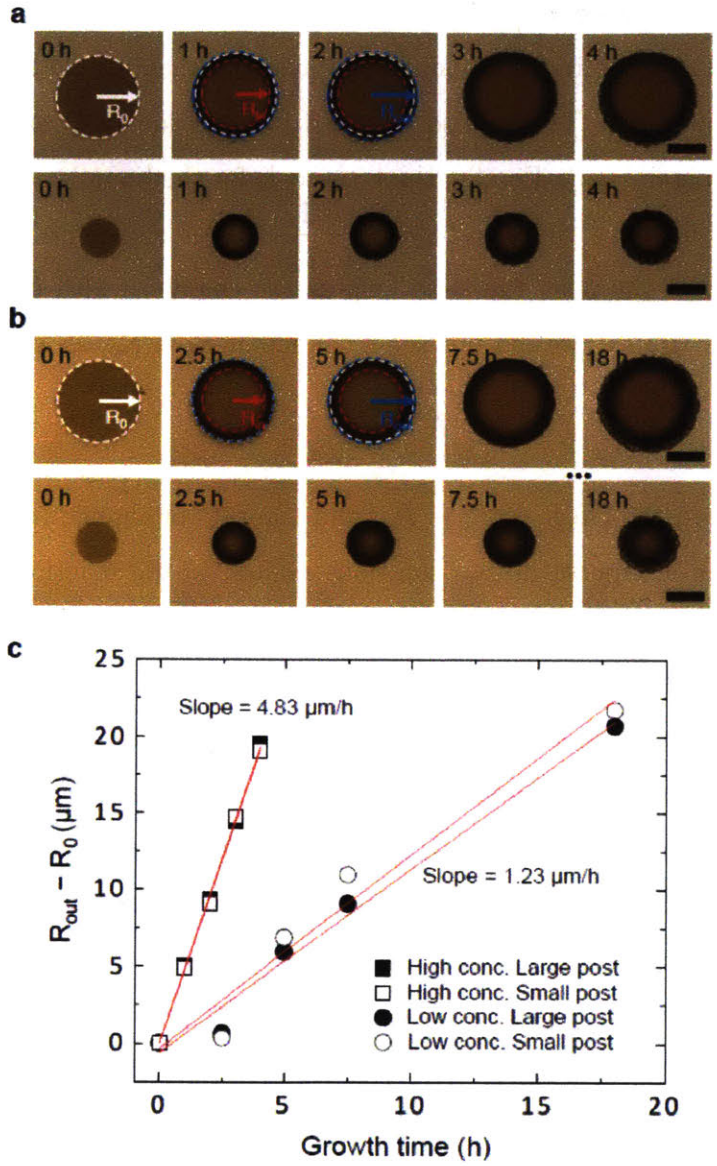

Figure 5-4: In situ growth of $CaCO_3$ posts. In situ optical microscopy images of $CaCO_3$/polymer composite posts in the channel versus growth time using different supersaturated solutions prepared by the addition of 100 mL of sodium bicarbonate solution (40 mM (a) and 20 mM (b)) to 100 mL of calcium chloride solution (1.6 mM (a) and 0.8 mM (b)). All the scale bars are 100 Îijm. c) The changes in $R_{out} - R_0$(squares: (a), circles: (b)) as a function of the growth time. Reprinted with permission from Seung Goo Lee, Hyundo Lee, Ankur Gupta, Sehoon Chang, Patrick S. Doyle. "Site-Selective In Situ Grown Calcium Carbonate Micromodels with Tunable Geometry, Porosity, and Wettability." Advanced Functional Materials 26.27 (2016): 4896-4905. Copyright 1999-2017 John Wiley & Sons, Inc.

still fail with the control of submicrometer scales. [113]

In our $CaCO_3$/polymer composite system, the photopatternable microposts serves as an artificial support that allows $CaCO_3$ to grow, and the growth of $CaCO_3$ enables the pores of the micromodel to be tuned dynamically, down to submicrometer gap widths between the posts. Fig.5-5 (a) demonstrates this ability for heterogeneous structures composed of two kinds of square posts arranged in a rectangular array with different dimensions in a single microchannel. The $CaCO_3$ grows rapidly on both posts for initial 4 h period, after that, it grows more slowly, and in the latter state comes into direct contact with the $CaCO_3$ of neighboring small posts in the vertical position. The minimum gap widths between the small posts in thc 3rd and 4th rows near the channel wall reduced from 40 μm (0 h) to μm (4 h), and to less than 1 μm (at 10 h the gap is not resolvable in our setup), presumably resulting in the nanochannels formed by merging some parts of two $CaCO_3$ posts.

The posts have position-dependent growth of $CaCO_3$ as a result of different boundary layer thickness around different posts. Fig.5-5 (b) and (c) show the changes in dimensions of each post with side lengths of 100 μm (large) and 50 μm (small), respectively, near and far from the channel wall as a function of growth time. As one observes from the experimental results, the behavior of $CaCO_3$ growth is quite different before and after 4 h.

First, we focus on growth behavior before 4 h. The growth rate of $CaCO_3$ on the post side in parallel (y-direction) with the flow direction is faster than that perpendicular to the flow direction (x-direction). Furthermore, we detected the growth rate of the posts in the 1st row near the channel wall is the slowest in both large and small posts, consistent with the slower tendency of x-direction growth than y-direction. Finally, the growth rate of smaller posts is faster than larger posts, an effect not observed in the case of single posts. To develop an understanding of these results, we developed a COMSOL model where we solved the momentum equation

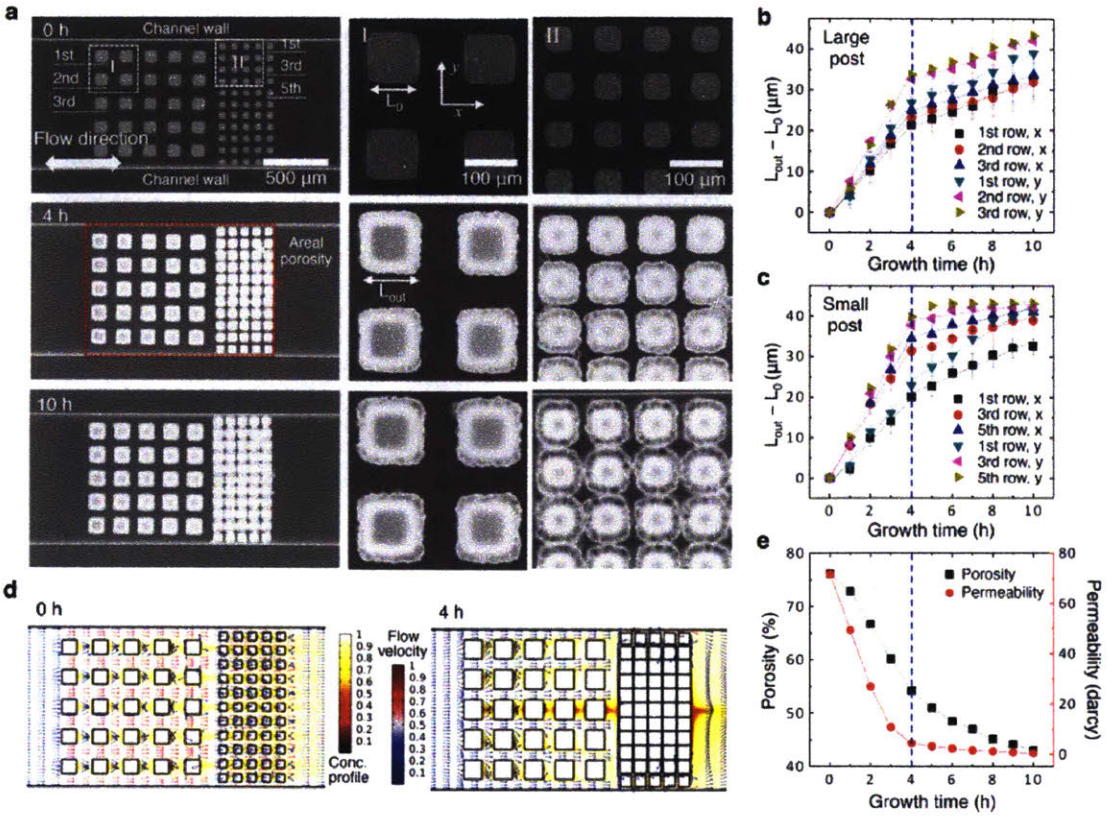

Figure 5-5: Growth of $CaCO_3$ posts with heterogeneous structures. (a) Optical microscopy images of the heterogeneous $CaCO_3$ posts (side lengths, 100 and 50 μm) with different growth time (0, 4, 10 h) using the supersaturated solution. The right images are magnified views of the white dotted boxes in the left images. The red dotted box indicates the area for the calculation of a void fraction (porosity). L_0 and L_{out} indicate the initial length and the outer length of the posts, respectively. (b,c) L_{out}-L_0 versus growth time of the large (b) and small (c) posts with different positions and directions. The blue dashed lines indicate the transition to slow $CaCO_3$ growth. (d) Simulation results of the dimensionless concentration $[Ca^{2+}]/[Ca^{2+}]_0$ (background colors) and dimensionless flow velocity u/u_{max} (arrow colors) of the supersaturated solution throughout the multiposts with different growth time (0 and 4 h). (e) Measured areal porosity of the red dotted area in (a) and computed permeability of the same region as a function of the growth time. Reprinted with permission from Seung Goo Lee, Hyundo Lee, Ankur Gupta, Sehoon Chang, Patrick S. Doyle. "Site-Selective In Situ Grown Calcium Carbonate Micromodels with Tunable Geometry, Porosity, and Wettability." Advanced Functional Materials 26.27 (2016): 4896-4905. Copyright 1999-2017 John Wiley & Sons, Inc.

coupled with species transport equation. The obtained results suggested that the dimensionless concentration $\frac{[Ca^{2+}]}{[Ca^{2+}]_0}$ is higher in the regions of higher dimensionless velocity $\frac{u}{u_{max}}$ (Fig.5-5 (d) at 0 h). This is expected since the mass transfer coefficient will be higher in the regions of higher velocity and the concentration would be closer to the fresh ionic concentration. Since the velocity is higher in the region of vertical gaps between the posts, the growth rate in y-direction is higher than the growth rate in x-direction. Moreover, because of higher velocities in the vertical gaps between smaller posts as compared to larger posts, the growth rate is higher for smaller posts. This effect is not observed for single posts since the velocity (and mass transfer coefficient) is practically independent of post size. Finally, the effect of slower growth rate of posts near the walls is not captured in our simulations. We believe that this happens because our simulations assume a very homogenous spatial distribution of posts whereas in experiments there is some heterogeneity in the spatial distribution.

At 4 h, the gap between small posts in the center of the channel reduces to a few micrometers. Thus we observe a reduction in flow rate to about 20% of the initial value (estimated through the COMSOL model) and a slower $CaCO_3$ growth for all posts (the blue dashed lines in Fig.5-5 (b) and (c) demarcate the onset of the slow growth period). Also, a higher flow resistance in the central part of the channel forces the flow to go through the region near walls (Fig.5-5 (d) at 4 h) and hence, after 4 h the growth rate is highest in the 1st row (Fig.5-5 (b) and (c)). These results show that the local differences in the flow velocity induced by geometry affect the regional growth of $CaCO_3$.

Two parameters that are often used to characterize porous media are porosity and permeability. Changes in the areal porosity with the growth time were calculated from the optical microscopy images of $CaCO_3$ posts (Fig.5-5 (e)). The porosity decreases continuously from 76% to 43% over the period of 10 h. There is spatial heterogeneity in local porosity due to the different post sizes (Fig.5-5 (a)). Our method allows us to create structures with a wide range of porosities simply by changing the lithographic

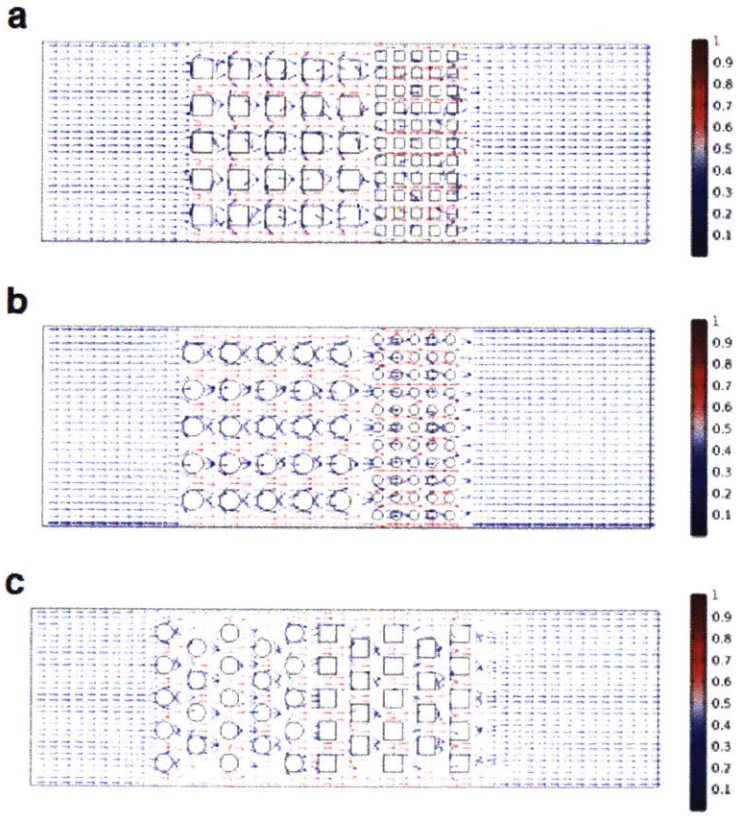

Figure 5-6: The simulation of the flow velocity $\frac{u}{u_{max}}$ in heterogeneous microstructures with different shapes and arrays. (a,b) Rectangular arrays of two different squares (a) and circles (b). (c) zigzag arrays of circles and squares Reprinted with permission from Seung Goo Lee, Hyundo Lee, Ankur Gupta, Sehoon Chang, Patrick S. Doyle. "Site-Selective In Situ Grown Calcium Carbonate Micromodels with Tunable Geometry, Porosity, and Wettability." Advanced Functional Materials 26.27 (2016): 4896-4905. Copyright 1999-2017 John Wiley & Sons, Inc.

mask and hence post size. Further, the method provides a simple way to control the porosity of a micromodel in time by varying the flow of the supersaturated solutions.

Due to well-known experimental challenges in measuring small flow rates in microfluidic channels, [151] we estimated the permeability in the region around posts (same area in which the areal porosity was measured) using a COMSOL model (Fig.5-5 (3)). Permeability calculations were performed through COMSOL simulations. To calculate permeability, we kept the dimension of the posts as a variable that can change with time. We performed 10 simulations (one for every hour) and changed the post-size based on experimental data of post sizes for every hour. In each simulation, we solved the Navier-Stoke's equation to obtain the velocity profiles in the system with pressure inlet and pressure outflow boundary conditions. The permeability was calculated over a region of 1.75 mm in length where the posts were present. Assuming Darcy's law is valid, permeability variation with time was computed using the following relation: $K = \frac{\mu_w u_{avg} L}{\Delta P}$, where u_{avg} is the calculated average velocity, L is the length of the region where permeability was calculated (1.75 mm), μ_w is the viscosity of water and ΔP is the pressure drop across the region (different for different time points). There is a rapid decrease in permeability in the first 4 h from 72 darcy to 4 darcy due to high $CaCO_3$ growth in the central region of the channel. After 4 h, almost the entire pressure drop in the channel is concentrated across the post region. A 10-fold reduction in the flow rate is observed from 4 h to 10 h due to continuous increase in the flow resistance associated with $CaCO_3$ growth. After 10 h, the permeability is estimated to be 0.4 darcy. The permeabilities we obtain during 4-10 h are within the reported permeability range for Arab-D reservoirs.

5.5 Demonstration of Acid Stimulation in a Heterogeneous Carbonate Micromodel

In the petroleum industry, acid stimulation is used to enhance the reservoir permeability during secondary and tertiary recovery. Acid stimulation of carbonate reservoirs

involves a reaction between an acid and calcite or dolomite, that is intended to enhance the flow of immobile oil in the reservoirs. As acid flooding has done, pore growth occurs as the carbonate rocks are dissolved by the acid. In spite of the importance of this practice, core-based methods and conventional micromodels have not been able to demonstrate the geochemical fluid-rock interaction due to their opaqueness or other material limitations. Carbonate micromodels are the only micromodels that can be used to understand the acid fracturing process. [125] Using our micromodel, flow-induced carbonate dissolution was observed and imaged over time as acidic brine flooded through the channel (Fig.5-7). A micromodel having two different sizes of squares was patterned, and calcium carbonate was grown from the template. The experiment was performed using acidic brine (1% hydrochloric acid, 1.81 M sodium chloride in DI water) under constant flow rate (0.5 mL/min). For oil-water displacement experiments, two immiscible fluids were serially introduced into the channel under constant flow rate (0.1 mL/min).

From the process of the demonstration, we can be inferred that the flow enhancement and the carbonate dissolution are correlated with each other. Acid flows first through the area of low flow resistance, then the acid dissolved calcium carbonates in that area, and it lowers flow resistance further. This cycle eventually accelerates the carbonate dissolution and the flow enhancement of the area. Fig.5-7 (a) shows the early-stage dissolution process of the heterogeneous micromodels over a period of two minutes. CO_2 bubbles were first observed around the large $CaCO_3$ post array, and then the small post array, as acidic brine flowed from left to right. The acidic brine flowed through the bottom section of the small post array (red dotted box in Fig.5-7 (a)), because this section had the lowest flow resistance. As a result, the dissolution of $CaCO_3$ posts propagated from the left wall to the right wall of the channel in the small post area (Fig.5-7 (b)). From this phenomenon, it can be inferred that flow and dissolution are correlated with each other. [125] Fig.5-7 (c), a graph representing the $CaCO_3$ fraction change in the fixed area over time, shows an exponential decay trend. This trend can be attributed to the initial fast decrease in the large post array,

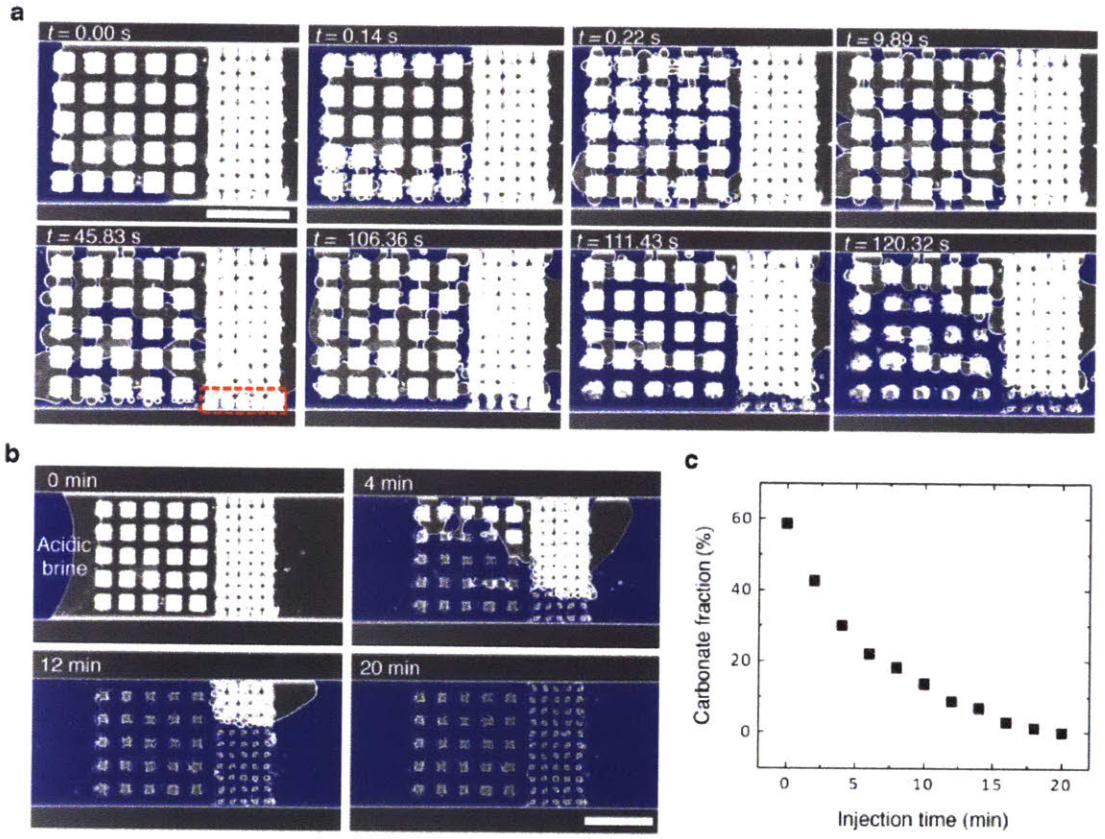

Figure 5-7: Acid fracturing of the heterogeneous $CaCO_3$ micromodel. (a,b) The sequential optical microscopy images showing the dissolution process of the $CaCO_3$ micromodel under acidic brine (1% HCl, 1.81 M NaCl in deionized water) injection (flow direction from left to right) (scale bar, 500 μ). The blue color highlights the region of the acidic brine. The red dotted box indicates the lowest flow resistance region in the small post array. (c) Areal fraction of $CaCO_3$ in the micromodel versus the injection time of the acidic brine. Reprinted with permission from Seung Goo Lee, Hyundo Lee, Ankur Gupta, Sehoon Chang, Patrick S. Doyle. "Site-Selective In Situ Grown Calcium Carbonate Micromodels with Tunable Geometry, Porosity, and Wettability." Advanced Functional Materials 26.27 (2016): 4896-4905. Copyright 1999-2017 John Wiley & Sons, Inc.

followed by the approximately linear decrease in the small post array (about 2.5 rows of posts every 4 min). To our knowledge, this study is the first demonstration of both $CaCO_3$ growth and dissolution in a single micromodel.

5.6 Large-Area Photo-patterning with Contact Flow Lithography and $CaCO_3$ Growth

An additional advantage of our route to produce synthetic micromodels is the large-area fabrication of multiple $CaCO_3$ posts in a microchannel. Compared to the conventional microscope-based lithography, a customized contact lithography system generates strong and homogeneous illumination, and thus allows a wide effective area maintaining excellent resolution. [122] Fig.5-8 (a) shows the $CaCO_3$ micromodels fabricated by the contact lithography with a specially designed chrome photomask. The size and overall shape of polymerized structures are in excellent agreement with the mask pattern, with sharp edges. The posts become dark and large as the growth time increases for 2 h. The round-shaped posts arranged in zigzag array also enable the regional growth to be more homogeneous than the square posts arranged in a rectangular array, which may be attributed to a decrease in the local difference of the flow velocity induced by geometry (Fig.5-6). To ensure that we have uniform supply of Ca^{2+} and CO_3^{2-} ions for all the posts in the large-area fabrication experiments, we injected the supersaturated solution into the channel from opposite directions every 30 minutes at a high flow rate.

5.7 Wettability Modification with Stearic Acid Treatment on the Composite Structure

In addition to geometry and porosity, tuning wettability of $CaCO_3$ micromodels makes it possible to understand fundamental fluid behavior and interactions among oil-water-rock phases. Although the $CaCO_3$ inherently shows water-wet behavior in the

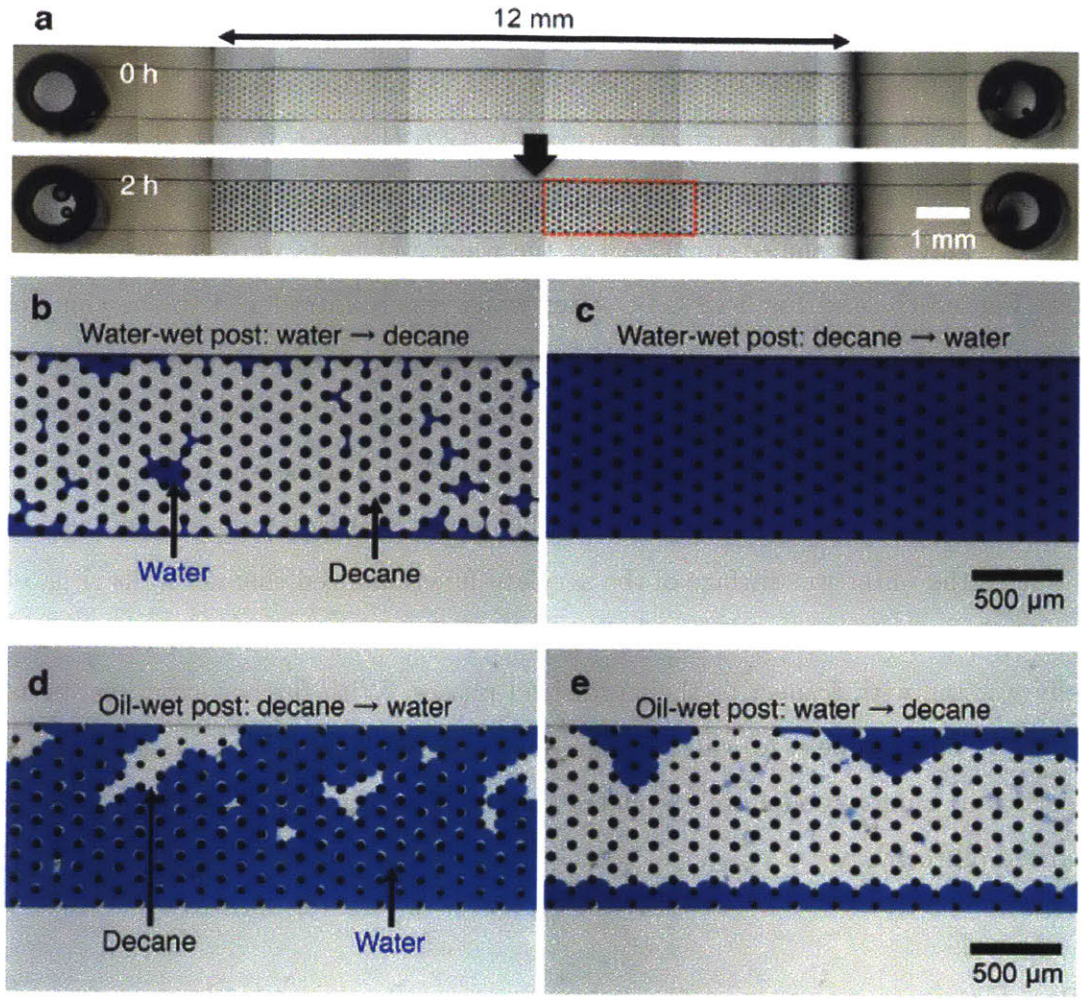

Figure 5-8: Multipost array oil-water displacement experiments. (a) Optical microscopy images of the $CaCO_3$ posts fabricated by a contact lithography. The posts were gradually grown through supplying the supersaturated solution from 0 to 2 h. The red dotted box indicates the area of (b-e). b,c) With this micromodel, water→decane→water flow experiment was conducted (flow direction from left to right). When decane displaced water (colored with methylene blue), water was selectively left in the water-wet posts (b). After water was re-introduced to the channel, decane in the channel was entirely washed away (c). (d,e) The micromodel was treated by a stearic acid. Thereafter, decane→water→decane flow experiment was conducted. When water displaced water, oil-wet posts held decane (d). After decane was re-introduced to the channel, water was replaced by decane, but water near side walls was left regionally (e). Reprinted with permission from Seung Goo Lee, Hyundo Lee, Ankur Gupta, Sehoon Chang, Patrick S. Doyle. "Site-Selective In Situ Grown Calcium Carbonate Micromodels with Tunable Geometry, Porosity, and Wettability." Advanced Functional Materials 26.27 (2016): 4896-4905. Copyright 1999-2017 John Wiley & Sons, Inc.

presence of oil and water (Fig.5-9), the surface wettability of $CaCO_3$ reservoirs is known to be mostly (84%) oil-wet. [58] Our $CaCO_3$ micromodel can be treated by stearic acid to decrease the surface energy of $CaCO_3$ (Fig.5-9 (b)). [152] Immiscible fluids were sequentially injected into the untreated $CaCO_3$ micromodel at constant pressures (water→decane→water). All of the water-wet posts were encapsulated by water (Fig.5-8 (b) and Fig.5-10 (a)). After water was re-introduced to the channel, decane in the channel was entirely washed away (Fig.5-8 (c)). In the opposite flow sequence (decane→water→decane), the oil-wet posts treated by stearic acid left decane at the posterior area (Fig.5-8 (d) and Fig.5-10 (a)). After decane was re-introduced to the channel, water was replaced by decane, but water near side walls was left regionally due to the water-wet surface of the acrylate-functionalized channel walls (Fig.5-8 (e)). These results show water-wet and oil-wet posts always had the same result of totally wetting with respect to their preferred phases. With further experiments using $CaCO_3$ micromodels, we can broaden our understanding of how the geochemical properties of a micromodel are correlated to and affect the displacement process for enhanced oil recovery.

5.8 Summary

Our $CaCO_3$ micromodel provides new capabilities for the design of mimicking rock microfluidic systems with dynamically tunable geometry, porosity, and wettability. By pairing photolithographic technique with site-selective mineralization, we can mimic real carbonate reservoir properties that encompass heterogeneous geometries containing a wide range of length scales, porosities, and permeabilities. Specifically, by flowing Ca^{2+} and CO_3^{2-} ions supersaturated solution we controlled $CaCO_3$ growth to dynamically adjust the geometry of structures. This allowed us to achieve small flow channels between the posts, falling within the length scales characteristic of microporous reservoirs (< 10 μm pores). Once the initial $CaCO_3$ structures have been created, their surface geochemistry can be altered by flowing fluids such as oil, water, CO_2 and acids, as demonstrated in the acid fracture experiment. The ability to

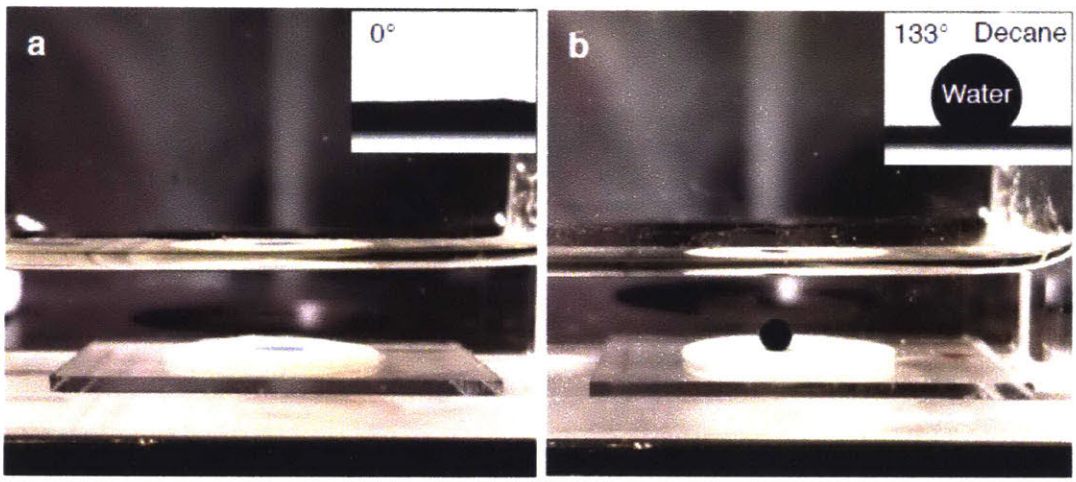

Figure 5-9: Water contact angles in decane. (a,b) Photographs showing water droplets on the substrates deposited with pristine $CaCO_3$ seed particles (a) and stearic acid-treated $CaCO_3$ seed particles (b). Insets show optical images of a static contact angle measurement for a water droplet in decane. Reprinted with permission from Seung Goo Lee, Hyundo Lee, Ankur Gupta, Sehoon Chang, Patrick S. Doyle. "Site-Selective In Situ Grown Calcium Carbonate Micromodels with Tunable Geometry, Porosity, and Wettability." Advanced Functional Materials 26.27 (2016): 4896-4905. Copyright 1999-2017 John Wiley & Sons, Inc.

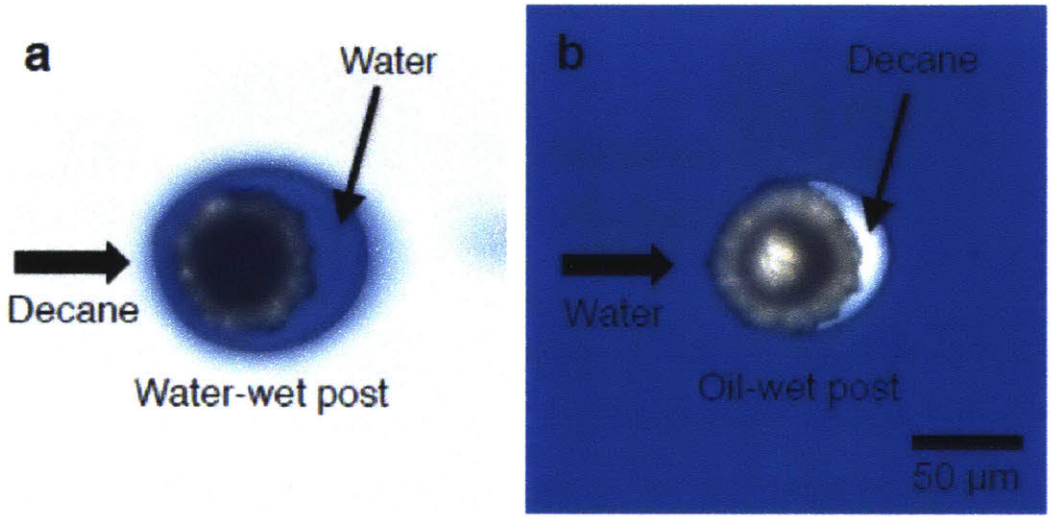

Figure 5-10: Single-post oil-water displacement experiments. (a) Microchannel was first filled with water, and then decane was introduced into the channel (flow direction from left to right). Water-wet $CaCO_3$ post was entirely surrounded by water. (b) Flow sequence was reversed relative to (a). The channel was filled with decane, and then water was displaced by decane. Oil-wet post was entirely surrounded by decane. Reprinted with permission from Seung Goo Lee, Hyundo Lee, Ankur Gupta, Sehoon Chang, Patrick S. Doyle. "Site-Selective In Situ Grown Calcium Carbonate Micromodels with Tunable Geometry, Porosity, and Wettability." Advanced Functional Materials 26.27 (2016): 4896-4905. Copyright 1999-2017 John Wiley & Sons, Inc.

tune the wettability of $CaCO_3$ and directly observe complex multiphase flows and geochemical fluid-$CaCO_3$ interactions makes this technique a very useful platform for studies in water flooding, CO_2 storage, CO_2-EOR, and chemical EOR [153,154]. The in situ grown $CaCO_3$ micromodels can be utilized for other applications in mineralogy, geology, and reservoir engineering. In our system, amorphous and metastable crystalline $CaCO_3$ can be used as seed nanoparticles to study the transformation mechanism of $CaCO_3$ polymorphs. Further, their transformation and stabilization can be controlled by various reaction parameters [155–157]. The approach can be extended to prepare magnesium(Mg)-bearing carbonate by using different anhydrous supersaturated Ca-Mg-CO_3 solutions [158], thereby facilitating the preparation of different types of synthetic carbonate reservoir micromodels. Our method also allows for precise control of mass transfer and can serve as a good model system to investigate crystal growth. Combining the micromodel with in situ spectroscopic imaging techniques, such as Raman or fluorescence, one can monitor the changes in polymorphs and morphologies which will reveal mechanisms of coprecipitation processes [159–161]. Advanced in situ spectroscopic techniques can also be used to visualize adsorption or desorption of chemical species on the carbonate rocks. Hence, this method can provide better understanding of chemical and physical features at oil/rock or water/rock interfaces as well as screening chemicals for EOR.

Chapter 6

Micelle-laden Hydrogels as Templates and Delivery Vehicles for Nanocrystals of Hydrophobic Drugs

Crystallization of active pharmaceutical ingredients (APIs) is a critical processing step of manufacturing drug products. While significant progress has been made in reducing crystal sizes, many processing techniques require high energy input and/or are still unable to produce crystals in the nanoscale regime. To optimize both manufacturing efficiency and bioavailability, we have developed a hydrogel material that serves as a template for nanocrystal formation and as a carrier for drug delivery. These templates contain micelle structures ligated onto a hydrogel matrix. The micelle size, which is determined by the chemistry of the surfactant, dictates the size of the crystal. Therefore, nanocrystals can be produced in high yield with precisely controlled sizes ranging from roughly 5 nm to 30 nm. Additionally, these hydrogels can serve as an effective delivery vehicle for enhanced uptake of hydrophobic drugs, as they simultaneously release drug with surfactant that increases the solubility in aqueous environments. These materials have the potential to dramatically enhance the efficiency of manufacturing and effectiveness of delivering pharmaceuticals.

6.1 Drugs in Nanocrystal Size

A major hurdle that modern drug discovery techniques have introduced is an increasingly large proportion of drug candidates that have either poor solubility (high lipophilicity) or permeability (numerous hydrogen bond acceptors) or both. [162,163] The mass flux of active pharmaceutical ingredient (API) through the cell wall (i.e., bioavailability) is directly proportional to both solubility and permeability. According to the biopharmaceutical classification system (BCS) employed by the FDA to classify active pharmaceutical ingredients (APIs), drugs with low aqueous solubility (i.e., hydrophobic drugs) that have high or low permeability are categorized into class II or class IV, respectively. Roughly 40% of small molecules that are commercially available and between 70% and 90% of those in commercial pipelines fall within these two classes of hydrophobic APIs. [164] While hydrophobic molecules may have high potency, their physico-chemical properties limit their clinical efficacy due to poor bioavailability. Therefore, enhancing both solubility and permeability of hydrophobic drugs could significantly expand the chemistry space of efficacious APIs.

Current methodologies to enhance the solubility of hydrophobic APIs include the formation of nanocrystals (nanonization), [165, 166] cyclodextrin complexation, [167] micelles and liposomes, [168] polymeric or lipid nanoparticles, self-emulsifying drug delivery systems (SEDDS), [169, 170] amorphous API particles, and drug co-crystallization (as salts, solvates, or hydrates). [164, 171] Combination technologies are also becoming more prevalent, in which multiple of these approaches are combined into a single formulation technique. However, many of these techniques have weaknesses that limit their application as effective drug delivery systems.

Of these options for hydrophobic API formulation, arguably the most prominent in academia and industry is the formulation of drug substances into nanocrystals. A drug in a nanocrystalline form has an enormous surface to volume ratio, which provides large driving force for higher solubility (Ostwald-Freundlich equation) and

correspondingly faster dissolution (Noyes-Whitney equation). The increased bioavailability of nanocrystal formulations may also allow for more potent individual doses that facilitate better patient compliance by simplifying oral dosage regimens. [172] An adverse effect of their larger surface area is that nanocrystals are susceptible to agglomeration and conversion between amorphous and crystalline (polymorph) forms. However, these issues can be readily resolved by adding surfactants as stabilizing excipients.

Within the category of nanonization, techniques are distinguished into top-down or bottom-up approaches depending on the size scale of intermediate products. In top-down nanocrystal production, the input is a micrometer (or larger) sized solid that is reduced by mechanical forces, such as through high pressure homogenization, spray drying, jet milling, and wet or dry ball milling. [166, 167, 173, 174] Bottom-up approaches build API nanocrystals from molecular inputs by controlling the time and/or length scale(s) of crystal growth. Examples of bottom-up techniques include precipitation by anti-solvent addition, super critical fluid solvents/anti-solvents, freeze drying, or conventional solvent removal. [173, 175] While many of these options are directed towards enhancing oral delivery, they are also applicable to parenteral, dermal, or pulmonary delivery forms since the benefits of enhanced bioavailability from nanoscale crystals still apply. [166, 175] These processes are capable of enhancing solubility, but many of these techniques require significant energy and material input as well as large time requirements both for production and quality control testing.

To fully optimize drug manufacturing, process requirements in the form of materials, energy, and time must be considered in addition to the chemical properties of the API. Hence, the delivery form chosen for a hydrophobic drug should enhance API efficacy (via properties such as polymorph control, crystal size, drug loading, solubility, and dissolution kinetics) and also be conducive to manufacturing in a cost-effective, efficient, high quality, and reproducible manner. Many research studies focus on API properties, but ignore the process conditions required to achieve them, which limit their translation to commercial scale production. An ideal solution to hydrophobic

API formulation would control all relevant drug properties, yet many developments only optimize a single quality.

Top-down approaches to nanocrystal formation are inherently less efficient than bottom-up processes due to the additional processing steps between initial micro-crystal synthesis and the desired final form of a nanocrystalline solid. The nanocrystals must then be purified/dried then recombined into the form of a suitable oral tablet. Producing a mechanically robust oral dosage form also introduces its own challenges for maintaining drug stability and loading while aiding dissolution and solubility. The minimization in crystal size is susceptible to morphology changes of the solid due to high energy input and introduces a source of manufacturing inefficiency due to the process itself and requiring additional quality control check-points.

The most widely-used nanocrystal manufacturing methods are wet ball milling, high pressure homogenization, and spray drying. However, the size of crystals generated using these top down approaches is limited to roughly 150 nm due to time requirements and physical limitations. [174, 175] Further, these techniques are typically time and energy intensive to yield a final drug crystal form/size. Despite the known benefits of nanocrystalline APIs, no current formulation method combines high drug loading, long-term stability, and fast release in an efficient manner (low cost and time).

6.2 Hydrogels as Templates for Nanocrystal Synthesis and as Carriers for Stable Drug Delivery

Hydrogels provide a platform for both synthesis and delivery of hydrophobic APIs by integrating ligands of hydrophobic chemistry into the matrix. [176] Not only do hydrogels offer a mechanically stable environment for handling and processing, they

do so will very small material quantity and porous microstructures to expedite mass transport. Hydrogels also offer the ability to control API crystallization by tuning the geometry and chemistry of the cross-linked matrix. [177, 178] Recent work has also combined hydrogel structures with nanoemulsions as templates for the formation of nanocrystals, which have shown promising results for generating nano-scale crystals with fast release. [179–181] However, as with other emulsion based formulation strategies, it is difficult to achieve high loading of nanocrystalline API using this approach. Further, hydrogels composed of ionic cross-links, such as sodium alginate, are susceptible to hydration induced degradation or instability of the API solid.

Our approach to incorporate nanocrystals in hydrogel particles is, we first make an empty hydrogel particles as a platform for crystallization of APIs, soak the particles with drug dissolved solution, and induce crystallization in the hydrogel particles by evaporating the solvent. And in addition to that, we devised a way to form hydrophobic compartments by incorporating acrylated micelles within hydrogel matrices (Fig.6-1).

6.3 Drugs Crystallization in Hydrogels: Soaking and Drying Method

In this work, fenofibrate (FEN) is used as a standard hydrophobic API for its availability and extensive prior study. In particular, recent work has quantified the relationship between crystalline FEN melting point and crystal size by using porous glass beads with varying pore sizes. [182, 183]

Fig.6-1 shows how hydrogel matrix can serve as a crystallization domain for the controlled synthesis of hydrophobic APIs. Hydrophobic APIs dissolved organic solvent can be infused by solvent exchange steps. APIs soaked in the hydrogel matrix are crystallized by evaporation of the solvent, and the solid form of drugs is left in

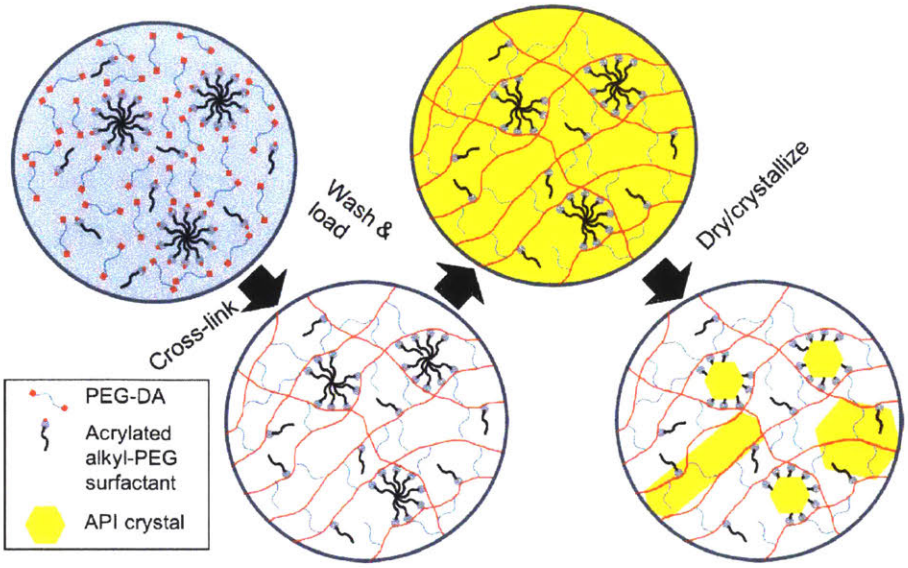

Figure 6-1: Schematic illustration showing the process of soaking hydrogel matrix with drug dissolved solutions and inducing nanocrystallization of the drugs by evaporation of the solvents.

the hydrogel. The hydrogel matrix stabilizes the nanocrystals from coalescence and degradation, and when ingested, the hydrogel is then hydrolyzed, releasing the APIs. The hydrogel will also release PEG and a mixture of linear and cross-linked polyacrylate that have previously been shown to be biocompatible. Further, polyacrylate may even aid in increasing permeability, which is beneficial for formulating class III and class IV drugs.

Fig.6-2 is a schematic of the process of how we make hydrogel particles and crystallize drugs in the hydrogel particles. We make hydrogel particles with a PDMS mold, exchange solvents to load drug dissolved solution in the particles, and dry particles for crystallization. Fig.6-3 is the actual images showing the process.

We confirmed the presence of fenofibrate crystals, that is our model drug, with X-ray powder diffraction (XRPD) analysis (Fig.6-4). To estimate the size of crystals, we used differential scanning calorimetry (DSC), and from melting point depressions, we could infer the sizes of fenofibrate crystals with different hydrogel particles having different crosslinker and porogen composition. [182, 183]

Fig.6-5 (a) shows a characteristic set of DSC (differential scanning calorimetry)

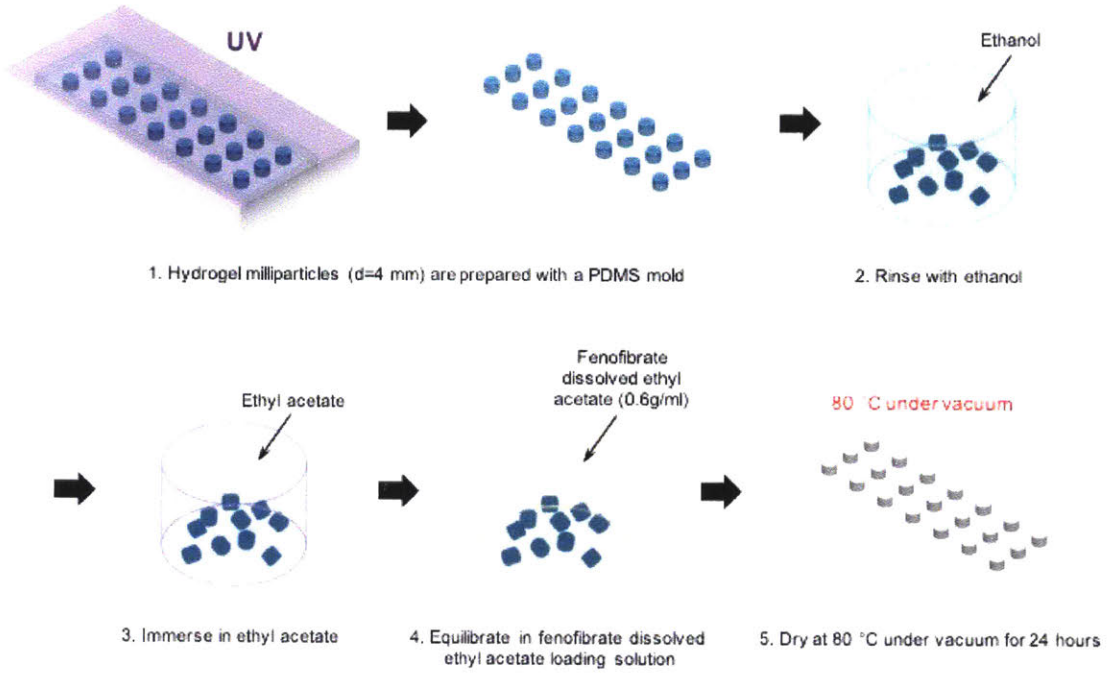

Figure 6-2: Schematic illustration showing the process of making drug-loaded hydrogel particles.

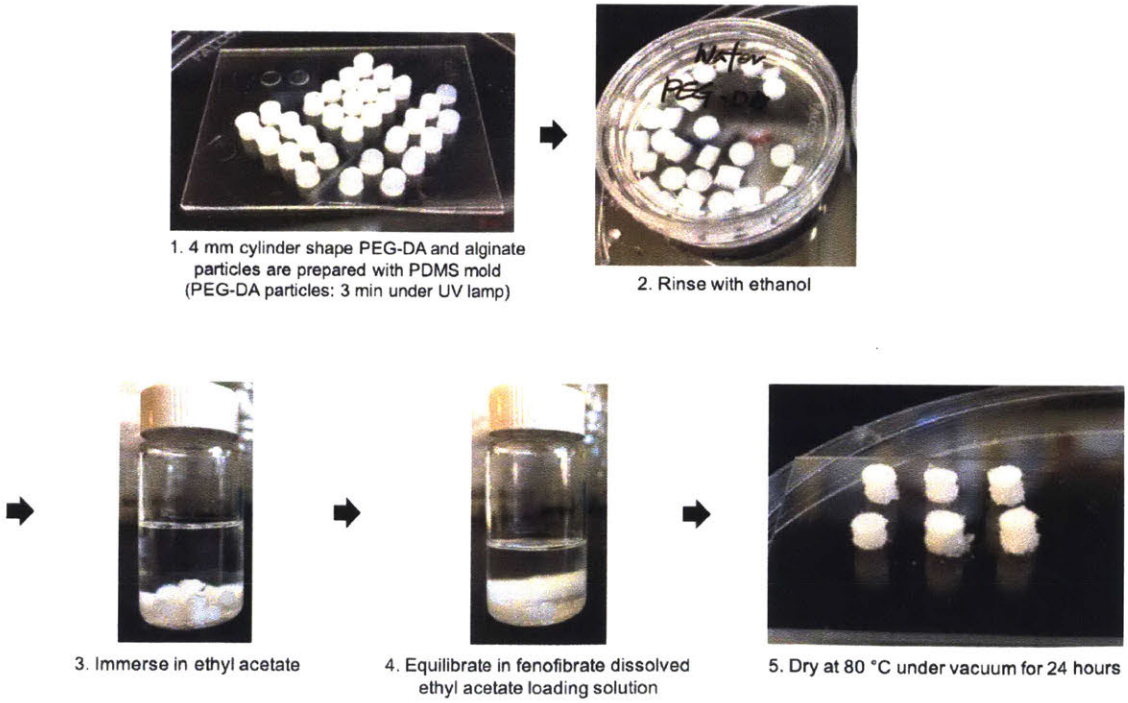

Figure 6-3: Images showing the process of making drug-loaded hydrogel particles.

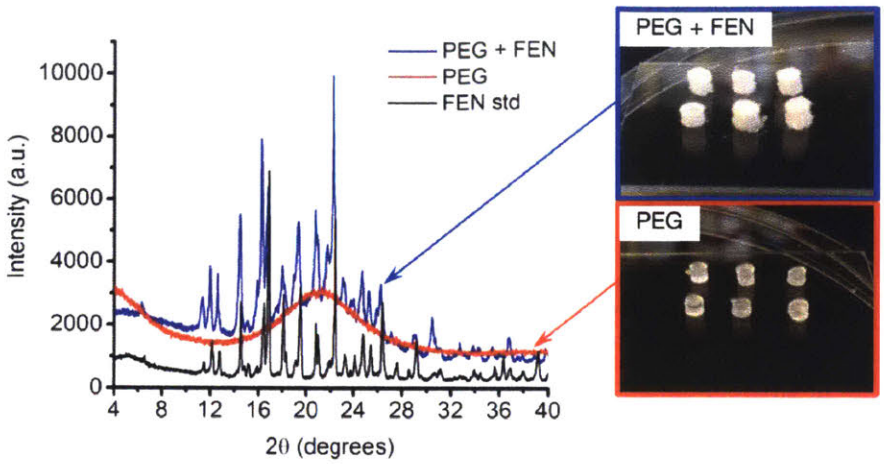

Figure 6-4: XRPD (X-ray powder diffraction) for the confirmation of fenofibrate (FEN) crystallization in hydrogel matrix. XRPD results demonstrating the integration of fenofibrate (FEN) crystals into PEGDA (poly(ethylene glycol) diacrylate) based matrices. The hydrogel (red line) shows only one broad peak corresponding to the disordered mesh while the FEN loaded hydrogel (blue line) shows both features of the hydrogel and the peaks corresponding to a crystalline fenofibrate standard (black line).

thermograms of plain PEGDA (poly(ethylene glycol) diacrylate) hydrogels with 20% PEGDA loaded with FEN compared with a bulk crystal standard. DSC results for other PEGDA concentrations are provided in the Supplementary Information. In all cases, the peaks are shifted to smaller temperatures relative to the bulk sample, indicative of crystal sizes below about 500 nm. As the mesh size increases with larger contents of PEG (poly(ethylene glycol)) porogen, multiple peaks appear as a result of a polydisperse distribution of crystal sizes. Interestingly, the most significant species (i.e., the largest peak) becomes the smallest crystal size (roughly 30 nm in diameter) when the mesh is largest (20% PEGDA, 40% PEG).

6.4 Acrylated-Micelles Incorporation for Even Smaller Crystals

The range of crystal sizes that can be formed in PEGDA based hydrogels indicates that these matrices can facilitate the formation of stable hydrophobic API nanocrys-

Table 6.1: Summary of chemical properties of the surfactants used in this study, including the HLB(Hydrophile-Lipophile Balance) value and chemical composition of the original surfactants and hydrodynamic diameter before (D_h) and after (aD_h) the acrylation reaction.

surfactant	M_w	HLB	# C/PPG	# PEG	D_h (nm)	σ_D (nm)	aD_h (nm)	σ_D (nm)
L10	627	13.6	12	10	8.43	0.5	10.5	0.3
C10	683	12.9	16	10			12.6	0.8
L23	1268	16.9	12	23	8.6	0.2	8.68	0.1
C20	1124	15.7	16	20	10.1	0.1	10.2	0.1
S20	1152	15.3	18	20	11.2	0.4	16	0.4
B25	1496	17.3	22	25			12.8	0.1
S100	4738	18.8	18	100	24.9	1.3	26.1	0.8
F68	8400	>24	30	80	7.07	0.2	12.5	0.4
F127	12700	22	70	106	8.86	0.9	9.42	0.4

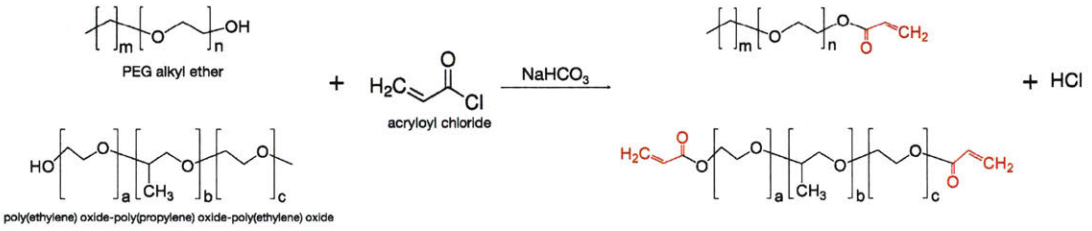

Figure 6-6: Acrylation of the surfactants âĂŞ surfactants having different alkyl chain (hydrophobic) and poly(ethylene glycol) (hydrophilic) lengths are tested

number of monomeric units. The two pluronic triblock surfactants studied are F68 and F127, which contain a polypropylene glycol (PPG) hydrophobic region rather than an alkyl chain. Due the folding necessary for pluronics to form micelles, the effective length of their hydrophobic region is half that of the PPG segment listed in Table 6.1. The surfactants are organized into three sub-sections distinguished by the size of the PEG region, which correspond to roughly 10, 20, and 100 PEG units. Thus, the influence of the size of the PEG segment and hydrophobic core of the micelle can be independently studied.

Integrating micelle templated hydrophobic domains into hydrogel matrices requires that the surfactants be capable of being chemically bonded into the polymer backbone. To become reactive and compatible with PEGDA based hydrogels, an acrylate functional group was attached to the end of the PEG segment of each surfactant except B25, which was purchased commercially in the acrylated form. Hydrodynamic

Table 6.1: Summary of chemical properties of the surfactants used in this study, including the HLB(Hydrophile-Lipophile Balance) value and chemical composition of the original surfactants and hydrodynamic diameter before (D_h) and after (aD_h) the acrylation reaction.

surfactant	M_w	HLB	# C/PPG	# PEG	D_h (nm)	σ_D (nm)	aD_h (nm)	σ_D (nm)
L10	627	13.6	12	10	8.43	0.5	10.5	0.3
C10	683	12.9	16	10			12.6	0.8
L23	1268	16.9	12	23	8.6	0.2	8.68	0.1
C20	1124	15.7	16	20	10.1	0.1	10.2	0.1
S20	1152	15.3	18	20	11.2	0.4	16	0.4
B25	1496	17.3	22	25			12.8	0.1
S100	4738	18.8	18	100	24.9	1.3	26.1	0.8
F68	8400	>24	30	80	7.07	0.2	12.5	0.4
F127	12700	22	70	106	8.86	0.9	9.42	0.4

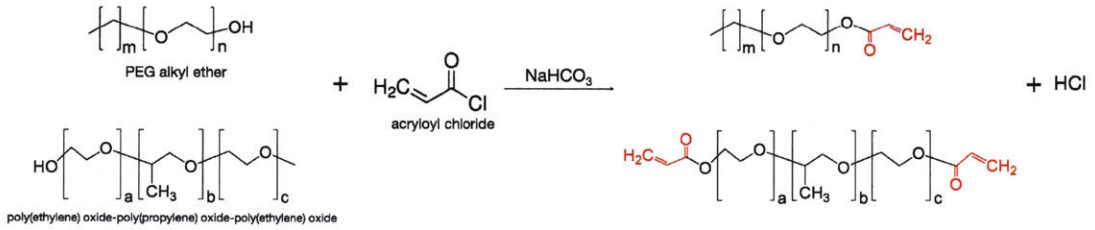

Figure 6-6: Acrylation of the surfactants âĂŞ surfactants having different alkyl chain (hydrophobic) and poly(ethylene glycol) (hydrophilic) lengths are tested

number of monomeric units. The two pluronic triblock surfactants studied are F68 and F127, which contain a polypropylene glycol (PPG) hydrophobic region rather than an alkyl chain. Due the folding necessary for pluronics to form micelles, the effective length of their hydrophobic region is half that of the PPG segment listed in Table 6.1. The surfactants are organized into three sub-sections distinguished by the size of the PEG region, which correspond to roughly 10, 20, and 100 PEG units. Thus, the influence of the size of the PEG segment and hydrophobic core of the micelle can be independently studied.

Integrating micelle templated hydrophobic domains into hydrogel matrices requires that the surfactants be capable of being chemically bonded into the polymer backbone. To become reactive and compatible with PEGDA based hydrogels, an acrylate functional group was attached to the end of the PEG segment of each surfactant except B25, which was purchased commercially in the acrylated form. Hydrodynamic

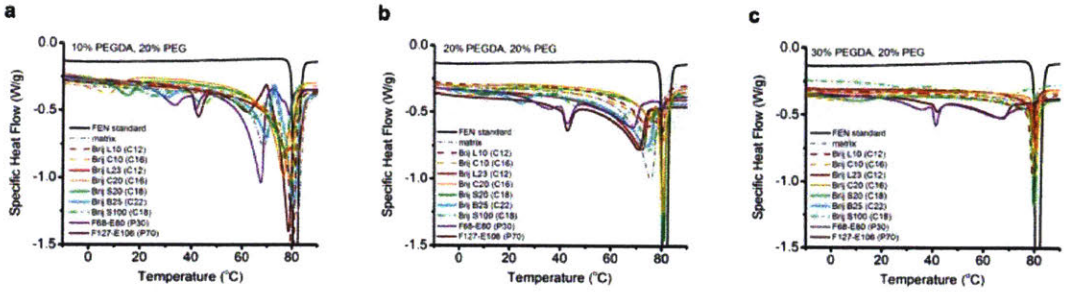

Figure 6-7: DSC thermograms of FEN loaded micelle laden hydrogels using the surfactants listed in Table 6.1 at a concentration of 8.4% (w/v) embedded in (a) P10G20, (b) P20G20, and (c) P30G20 matrices relative to a bulk FEN standard and the pure matrix.

diameters determined by DLS before (D_h) and after (aD_h) the reaction are provided in Table 6.1 and compared. In most cases, the addition of an acrylate group has no effect on the micelle size. For two surfactants (S20 and F68) the deviation in D_h is noticeable, but the increase in apparent hydrodynamic diameter after the reaction is likely the result of enhanced association between micelles rather than the formation of larger micelles.

To identify the chemical requirements for micelles to template the formation of sub 100 nm crystals, a wide range of surfactants are studied using three different matrix compositions. Each of the surfactants listed in Table 6.1 are formulated at a concentration of 8.4 %w/v with 10%, 20%, and 30% PEGDA with 20% PEG as a porogen. The resulting DSC thermograms are shown in Fig.6-7 for all matrix and surfactant combinations. For all three matrix compositions, all surfactants except L10 and L23 and C10 and C20 were able to form sub 10 nm crystals. Under all conditions where micelles appear to template nanocrystal formation, peaks still appear at higher temperatures comparable to those found without the presence of surfactant, but at a smaller magnitude.

Crystal sizes appear to correlate roughly with the hydrodynamic diameter of the micelle prior to integration into a hydrogel. Figure 6-8(a) shows a summary of the crystal sizes extracted from each of the peaks below 50 °C in the thermograms shown in Fig. 6-7. Crystal sizes close to those produced without surfactant present are not

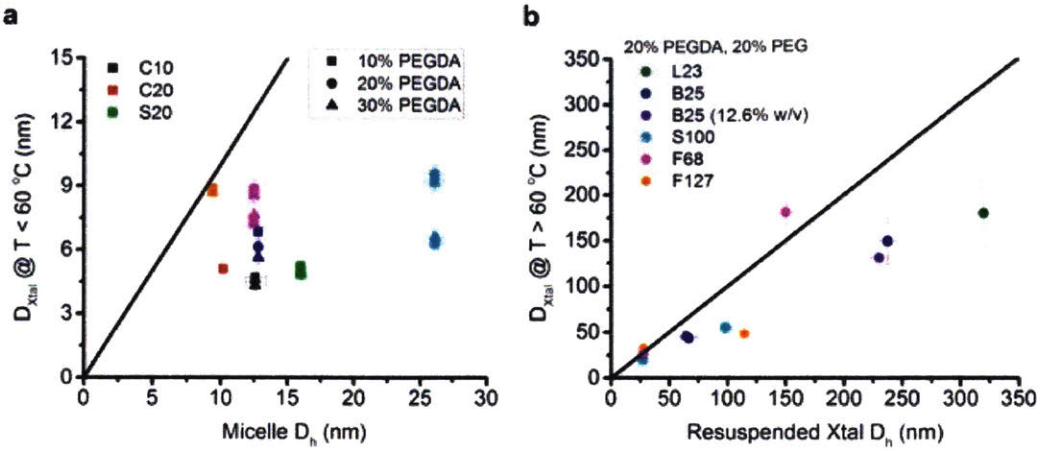

Figure 6-8: (a) Comparison of micelle hydrodynamic diameter, measured by DLS, with the smallest crystal sizes extracted from DSC thermograms ($T_melt < 60\,°C$). (b) Comparison of the effective hydrodynamic diameter after decomposing FEN loaded hydrogels (20% PEGDA) with the crystal sizes extracted from DSC thermograms at high temperatures ($T > 60\,°C$). The y = x line is shown is a guide to the eye.

included to highlight the effect of micelles. Under all conditions, the hydrodynamic diameter of the micelles sets an upper limit for nanocrystal size. That the final crystal size is typically smaller than the micelle reflects the fact that the internal hydrophobic corona is only a fraction of the total volume of the micelle. Further, the hydrogel matrix composition does not appear to influence the size of crystals formed within micelles if they are capable of inducing crystallization. The primary influence of matrix composition is on the size of crystals on the order of 50 nm to 200 nm (a melting temperature of roughly 70 °C). Depending on the combination of surfactant and mesh, the size and population of these intermediate nanocrystals will shift slightly.

In addition to the formation of 5 nm - 10 nm crystals by micelles ligated into hydrogels, the surfactant also serves as a means to enhance the solubility and possibly permeability during delivery. Smaller crystals have a larger local solubility and are more readily and consistently adsorbed through the cell wall. Therefore, if the initial nanoscale crystal size is maintained after release, the formulation will have a higher likelihood of enhancing the bioavailability of the API.

The final crystal size after release from the hydrogel is simulated through an

expedited decomposition process of hydrolysis in a 1.0M sodium hydroxide solution. The release of both drug and surfactant yield a suspension of stabilized crystals that would typically be impossible due to the poor solubility of fenofibrate in water. The crystal size is tested by DLS after filtering to remove impurities and large particles of residual cross-linked polyacrylate. The sizes of the resulting crystals stabilized in suspension after decomposition of several micelle laden hydrogels are shown in Fig. 6-8(b) relative to the largest crystal sizes identified by DSC. Under all conditions tested, two large nanocrystal peaks were present in DSC thermograms and yielded two decay modes in the DLS correlation function.

Two attributes of the surfactant included in the hydrogels are apparent from the results in Fig. 6-8(b). First, no crystals below 25 nm in size were observed by DLS. This could either result from the inability of DLS to resolve crystals of this size when larger crystals are also present given that the relative scattering intensity of particles in DLS is a strong function of size. However, the more likely cause is that the surfactant content is insufficient to stabilize the smallest crystal sizes observed by DSC (at least under the compositions that had originally induced their formation). Regardless, nanosuspensions of crystals between 25 nm and 250 nm still have large benefits on solubility and permeability. An additional trend is that larger surfactants are more capable of stabilizing smaller nanocrystals when released from decomposed hydrogels. Crystals released from the pluronic laden hydrogels remain below 100 nm while those stabilized by the smaller alkyl ethoxy surfactants have larger sizes. These results suggest that larger surfactants provide a route to the smallest nanocrystals stabilized in suspension and that the largest crystal sizes observed by DSC are indicative of the final crystal size after release from the hydrogel.

In addition to release, an important characteristic of API formulation is drug loading. Here, loading is quantified by thermal gravimetric analysis (TGA). The mass fractions of fenofibrate loaded in hydrogels laden with four different surfactant are plotted in Fig. 6-9 as a function of hydrogel matrix composition (all with 20% PEG). A characteristic TGA curve from which these values are extracted is provided in the Supporting Information. The results (symbols) show excellent agreement with

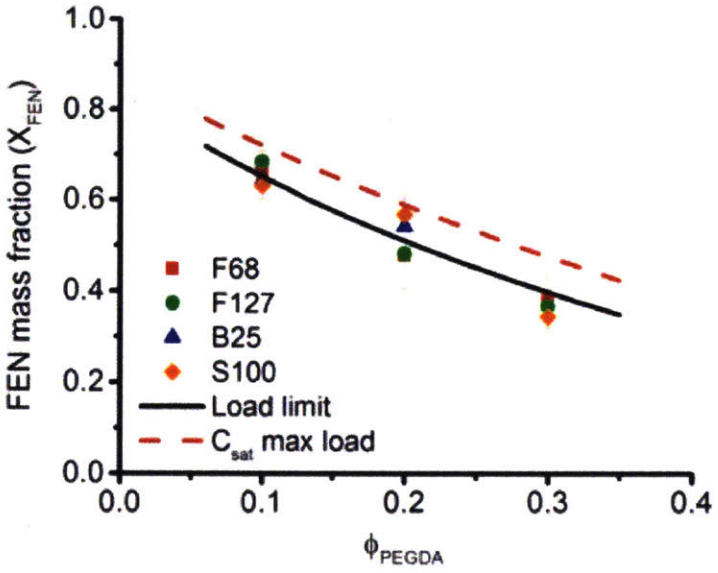

Figure 6-9: The fraction of FEN loaded in hydrogels as measured by the fraction of mass lost using TGA is plotted as a function of PEGDA content. All samples were loaded in a solution of 450 mg/mL fenofibrate in ethyl acetate with an upper limit of loading efficiency represented by the solid black line. The maximum possible loading with a saturated solution (620 mg/mL) is shown by the red dashed line.

a prediction (solid line) assuming a swelling ration of 1 and that all volume not consumed by the PEGDA or surfactant is filled by the organic solution used to load the API. Clearly, the mass of the hydrogel matrix is the limiting factor of API loading. Therefore, maximizing loading and minimizing crystal size is a matter of optimizing a balance of surfactant and PEGDA in the hydrogel composition. The model suggests that the maximum loading (by using a saturated solution of fenofibrate) can reach values approaching 80%, which is an enormous enhancement relative to other techniques currently used in industry.

6.5 Summary

In this chapter, we have demonstrated the ability to integrate acrylated surfactants into PEGDA based hydrogel scaffolds to serve as domains for the crystallization of nanocrstalline hydrophobic APIs. The model hydrophobic drug, fenofibrate, was used

for its available calibration curve comparing crystal size to melting temperature in order to identify the distribution of crystal sizes formed in micelle-laden hydrogels. Nanocrystals on the order of 50 nm to 200 nm were found to form in plain hydrogels without surfactant present, which was already an extensive reduction in crystal size compared to commonly used top-down micronization techniques. The addition of surfactant in the form of micelles provided hydrophobic domains that successfully templated the formation of nanocrystals smaller than 10 nm in size. An 18 carbon (stearyl) chain was found to be the minimum size of the hydrophobic segment of the surfactant to reliably induce crystallization of the hydrophobic API studied. Depending on the application, the composition of the hydrogel and surfactant can be tuned to produce a wide range of crystal size distributions. The loading of API in these micelle laden hydrogels can theoretically reach up to roughly 80% by mass, though the maximum loading reached here with fenofibrate was about 70%. Under all conditions, the presence of surfactant also stabilized nanocrystals between 25 nm and 250 nm after decomposition of the hydrogel. Therefore, these micelle-laden hydrogels serve as an effective framework to synthesize nanocrystals of hydrophobic APIs and enhance their release and solubility during delivery.

Chapter 7

Conclusion

Micromodels have broadened our understanding of multiphase flow in porous media and have provided solutions for practical engineering issues by visualizing phenomena occurring in subsurface oil reservoirs. However, multiphase flow mechanisms at the pore scale are still not clearly explainable, and newly developed practices or functional materials need repeated experiments before applying them at production sites. To understand the fundamental physics of underground flows, it is more desirable to start with a micromodel that has simple and prescribed structures, rather than injecting immiscible fluids into a black-box micromodel that has complex geometries and undefined wettability. New production practices and materials can be tested within well-defined micromodels that can represent various types of oil reservoirs.

In this thesis, we present two methods for fabricating reservoir micromodels with heterogeneous wetting and material properties. In Chapter 2, we introduce the first method where photopatterned, copolymerized microstructures are fabricated in a bottom-up manner. The use of rationally designed copolymers allow us to tailor the wetting behavior (oleophilic/phobic) of the structures without requiring additional surface modifications. Using this approach, two separate techniques of constructing microstructures and tailoring their wetting behavior are combined in a simple, single-step ultraviolet lithography process. This microstructuring method is fast, economical, and versatile compared with previous fabrication methods used for multiphase micromodel experiments.

In Chapter 3, we investigate and study the oil/water immiscible displacement process and oil pockets left behind obstacles as the consequence of displacements. When water reaches an obstacle, because of the preferential oil-wetting nature of the obstacle, the water/oil interface wraps around the obstacle, pinches off, and leaves an oil-pocket attached to the obstacle. We want to understand the underlying physics through a simple model and our theoretical model has an analytical solution. Because of the low capillary number of the water flow in our experiment, the water/oil interface can be approximated as a circular arc in the projected 2-D plane having specific contact angles with the two solid surfaces, the obstacle and the channel side wall. The low capillary number implies that the interface between oil and water is not affected by shear forces, and the pressure changes only across the interface. Through geometrical equations, we can obtain a set of equations that give an idea of how the interface evolves as it passes obstacles in microchannels. Our simple geometric model provides an analytic solution of interface evolution as it encloses the obstacles, and it can predict the trend of radius of the interface, final angular position on the obstacle at pinching off, and the amount of captured oil. We expand our model to two posts located parallel to the flow direction and predict critical distance that determines the formation of an oil bridge across two posts. Furthermore, we demonstrate controlled oil entrapment with different shapes, configurations of multiple obstacles, and oil entrapment , the reverse case, with hydrophilic structures.

In Chapter 4, we discuss liquid entrapment by sequential injection of immiscible liquids with periodic structures. We photopatterned triangular and sinusoidal structures with different dimensionless amplitudes m and dimensionless frequencies n, and built a quasi-static model that predicts the process of entrapment by approximating the interface as a circular arc in a similar approach as the previous chapter. Our experimental and theoretical results are in good agreement and our analysis highlights the importance of including the shape of the pattern in understanding the entrapment process. Specifically, we discuss using global slope mn, dimensionless amplitude m, and shape of pattern as design principles to control the entrapment process. Using the entrapped oil in the troughs, we also demonstrate a model study of the oil re-

covery process. We first trap oil in triangular patterned structures and examine the release of entrapped oil using a surfactant flood. We experimentally and theoretically investigate the release of trapped oil in triangular trough during a surfactant flood. Our experiments show three stages of recovery where the second stage displays the majority of oil recovery. Our computational model is able to capture the dominant physics but is unable to capture the intermittent droplet formation due to lack of surfactant transport. We report that a critical capillary number is required for the oil to be recovered, but oil recovery saturates at large capillary numbers. We also discuss the importance of geometry in oil recovery and provide a simple equation to approximately predict maximum oil recovery.

In Chapter 5, we introduce a method of building $CaCO_3$/hydrogel composite micromodels. This method provides new capabilities for the design of mimicking rock microfluidic systems with dynamically tunable geometry, porosity, and wettability. By pairing photolithographic techniques with site-selective mineralization, we can mimic real carbonate reservoir properties that encompass heterogeneous geometries containing a wide range of length scales, porosities and permeabilities. Specifically, by flowing Ca^{2+}, CO_3^{2-} ions rich/supersaturated solution we controlled $CaCO_3$ growth to dynamically adjust the structure's geometry. This allowed us to achieve small flow channels between the posts, falling within the length scales characteristic of microporous reservoirs (less than 10 μm pores). Once the initial $CaCO_3$ structures have been created, their surface geochemistry can be altered by flowing fluids like oil, water, CO_2 and acids, as demonstrated in the acid fracture experiment. The ability to tune the wettability of $CaCO_3$ and directly observe complex multiphase flows and geochemical fluid-$CaCO_3$ interactions, makes this technique a very useful platform for studies in water flooding, CO_2 storage, enhanced oil recovery (EOR) processes.

In Chapter 6, we present a method that has a hydrogel material that serves as a template for nanocrystal formation and as a carrier for drug delivery. Using this method, we are able to completely decouple the hydrogel particle synthesis from the drug loading process, and we can induce crystallization of nano-size model drugs in the hydrogel matrix. We also have developed a novel hydrogel precursor solution

that includes surfactants that form micelles and are polymerizable. As a result, once polymerization is initiated the cross-linked hydrogel matrix is formed while chemically integrating hydrophobic nano-domains templated by the initial micelle structures. Additionally, the products of the decomposed hydrogel material will enhance solubility (surfactant and polyethylene glycol, PEG) and may also help enhance permeability (PEG cross-linked polyacrylate or carbomer) and are therefore well suited for class II and class IV drugs.

This thesis work aims to introduce simple micromodel fabrication methods that can provide design flexibility with photopatterning, controlled wetting properties, and calcium carbonate growth in order to understand immiscible fluid displacement processes, and ultimately flows in underground reservoirs. Based on the developed micromodel fabrication methods and experiment, we propose a predictive model that can help us to have a fundamental understanding of oil/water displacement process from a relatively simple geometry to complex network design. By expanding the micromodel fabrication method, we are also able to make real-rock carbonate micromodels by incorporating calcium carbonate seed particles into microstructures and growing them with a supersaturated calcium carbonate solution. We believe our work can be useful for several applications. In oil recovery and soil remediation research, our platform can be used to quantitatively investigate the effect of surface shape on enhanced oil recovery, and to rapidly screen chemicals that are successful in recovering a trapped layer of oil. The effect of wetting in oil recovery can also be explored by combining experimental and theoretical research. Researchers interested in parallel experimentation for diagnostic research may also find this platform useful for creating several isolated aqueous pockets. Moreover, our platform can be easily adapted for large-scale phtopatterning and advanced microscopy techniques that allow this platform to be used for existing material synthesis methods. For applications in designing liquid infused surfaces, our results could provide design principles for successful entrapment of liquid layers. Understanding the effect of surface shape and amplitude of pattern on entrapment can also help research in the areas of fiber coating and gravure printing processes where dynamic length scales are involved. Lastly, we hope that

our results will help researchers building models for porous media flows using first principles to include the surface shape in their models.

Bibliography

[1] G.P. Willhite. *Waterflooding.* Society of Petroleum Engineers,Richardson, TX, Jan 1986.

[2] S Thomas. Enhanced oil recovery-an overview. *Oil & Gas Science and Technology-Revue de l'IFP*, 63(1):9–19, 2008.

[3] Calvin C Mattax, JR Kyte, et al. Imbibition oil recovery from fractured, water-drive reservoir. *Society of Petroleum Engineers Journal*, 2(02):177–184, 1962.

[4] AR Kovscek, H Wong, and CJ Radke. A pore-level scenario for the development of mixed wettability in oil reservoirs. *AIChE Journal*, 39(6):1072–1085, 1993.

[5] Jean-Christophe Perrin and Sally Benson. An experimental study on the influence of sub-core scale heterogeneities on co 2 distribution in reservoir rocks. *Transport in porous media*, 82(1):93–109, 2010.

[6] Marc Schneider, Florian Osselin, Ballard Andrews, Fadhel Rezgui, and Patrick Tabeling. Wettability determination of core samples through visual rock and fluid imaging during fluid injection. *Journal of Petroleum Science and Engineering*, 78(2):476–485, 2011.

[7] Can Ulas Hatiboglu and Tayfun Babadagli. Pore-scale studies of spontaneous imbibition into oil-saturated porous media. *Physical Review E*, 77(6):066311, 2008.

[8] Christophe Cottin, Hugues Bodiguel, and Annie Colin. Influence of wetting conditions on drainage in porous media: A microfluidic study. *Physical Review E*, 84(2):026311, 2011.

[9] N. K. Karadimitriou and S M Hassanizadeh. A Review of Micromodels and Their Use in Two-Phase Flow Studies. *Vadose Zo. J.*, September 2012.

[10] David Sinton. Energy: the microfluidic frontier. *Lab on a Chip*, 14(17):3127–3134, 2014.

[11] Benzhong Zhao, Christopher W MacMinn, and Ruben Juanes. Wettability control on multiphase flow in patterned microfluidics. *Proceedings of the National Academy of Sciences*, 113(37):10251–10256, 2016.

[12] Changyong Zhang, Mart Oostrom, Thomas W Wietsma, Jay W Grate, and Marvin G Warner. Influence of viscous and capillary forces on immiscible fluid displacement: Pore-scale experimental study in a water-wet micromodel demonstrating viscous and capillary fingering. *Energy & Fuels*, 25(8):3493–3505, 2011.

[13] Jerry Joseph, Naga Siva Kumar Gunda, and Sushanta K Mitra. On-chip porous media: Porosity and permeability measurements. *Chemical Engineering Science*, 99:274–283, 2013.

[14] Haihua Pei, Guicai Zhang, Jijiang Ge, Mingguang Tang, and Yufei Zheng. Comparative effectiveness of alkaline flooding and alkaline–surfactant flooding for improved heavy-oil recovery. *Energy & Fuels*, 26(5):2911–2919, 2012.

[15] A Kianinejad, MH Ghazanfari, R Kharrat, and D Rashtchian. An experimental investigation of surfactant flooding as a good candidate for enhancing oil recovery from fractured reservoirs using one-quarter five spot micromodels: the role of fracture geometrical properties. *Energy Sources, Part A: Recovery, Utilization, and Environmental Effects*, 35(20):1929–1938, 2013.

[16] Kai He, Liang Xu, Yuefeng Gao, Keith B Neeves, Xiaolong Yin, Baojun Bai, Yinfa Ma, Jonathan Smith, et al. Validating surfactant performance in the

eagle ford shale: A correlation between the reservoir-on-a-chip approach and enhanced well productivity. In *SPE Improved oil recovery symposium*. Society of Petroleum Engineers, 2014.

[17] Hamed H Al-Sharji, Carlos A Grattoni, Richard A Dawe, Robert W Zimmerman, et al. Pore-scale study of the flow of oil and water through polymer gels. In *SPE Annual Technical Conference and Exhibition*. Society of Petroleum Engineers, 1999.

[18] Ali Maghzi, Ali Mohebbi, Riyaz Kharrat, and Mohammad Hossein Ghazanfari. Pore-scale monitoring of wettability alteration by silica nanoparticles during polymer flooding to heavy oil in a five-spot glass micromodel. *Transport in porous media*, 87(3):653–664, 2011.

[19] Julien Beaumont, Hugues Bodiguel, and Annie Colin. Drainage in two-dimensional porous media with polymer solutions. *Soft Matter*, 9(42):10174–10185, 2013.

[20] David J Manlowe, Clayton J Radke, et al. A pore-level investigation of foam/oil interactions in porous media. *SPE reservoir engineering*, 5(04):495–502, 1990.

[21] Kun Ma, Rachel Liontas, Charles a. Conn, George J. Hirasaki, and Sibani Lisa Biswal. Visualization of improved sweep with foam in heterogeneous porous media using microfluidics. *Soft Matter*, 8(41):10669, 2012.

[22] Thomas W Haas, Hossein Fadaei, Uriel Guerrero, and David Sinton. Steam-on-a-chip for oil recovery: the role of alkaline additives in steam assisted gravity drainage. *Lab Chip*, 13(19):3832–3839, October 2013.

[23] Gautam C. Kini, Jie Yu, Lu Wang, Amy T. Kan, Sibani L. Biswal, James M. Tour, Mason B. Tomson, and Michael S. Wong. Salt- and temperature-stable quantum dot nanoparticles for porous media flow. *Colloids Surfaces A Physicochem. Eng. Asp.*, 443:492–500, February 2014.

[24] Christos Tsakiroglou, Olga Vizika-kavvadias, and R Lenormand. Use of Micromodels to Study Multiphase Flow in Porous Media. In *Int. Symp. Soc. Core Anal.*, pages 1–13, 2013.

[25] Naga Siva Kumar Gunda, Bijoyendra Bera, Nikolaos K Karadimitriou, Sushanta K Mitra, and S Majid Hassanizadeh. Reservoir-on-a-chip (ROC): a new paradigm in reservoir engineering. *Lab Chip*, 11(22):3785–3792, November 2011.

[26] Jay W Grate, Ryan T Kelly, Jonathan Suter, and Norm C Anheier. Silicon-on-glass pore network micromodels with oxygen-sensing fluorophore films for chemical imaging and defined spatial structure. *Lab Chip*, 12(22):4796–4801, November 2012.

[27] N. K. Karadimitriou, V Joekar-Niasar, S M Hassanizadeh, P J Kleingeld, and L J Pyrak-Nolte. A novel deep reactive ion etched (DRIE) glass micro-model for two-phase flow experiments. *Lab Chip*, 12(18):3413–3418, September 2012.

[28] Denis Bartolo, Guillaume Degré, Philippe Nghe, and Vincent Studer. Microfluidic stickers. *Lab Chip*, 8(2):274–279, February 2008.

[29] Viatcheslav Berejnov, Ned Djilali, and David Sinton. Lab-on-chip methodologies for the study of transport in porous media: energy applications. *Lab Chip*, 8(5):689–693, May 2008.

[30] Marc H. Schneider; and Patrick Tabeling. Lab-on-chip methodology in the energy industry: Wettability patterns and their impact on fluid displacement in oil reservoir models. *Am. J. Appl. Sci.*, 8(10):927–932, 2011.

[31] Elodie Sollier, Coleman Murray, Pietro Maoddi, and Dino Di Carlo. Rapid prototyping polymers for microfluidic devices and high pressure injections. *Lab Chip*, 11(22):3752–3765, November 2011.

[32] Mengjie Wu, Feng Xiao, Rebecca M Johnson-Paben, Scott T Retterer, Xiaolong Yin, and Keith B Neeves. Single- and two-phase flow in microfluidic porous media analogs based on Voronoi tessellation. *Lab Chip*, 12(2):253–261, 2012.

[33] Ki Wan Bong, Jingjing Xu, Jong-Ho Kim, Stephen C Chapin, Michael S Strano, Karen K Gleason, and Patrick S Doyle. Non-polydimethylsiloxane devices for oxygen-free flow lithography. *Nat. Commun.*, 3(May):805, January 2012.

[34] Pierre Horgue, Frédéric Augier, Paul Duru, Marc Prat, and Michel Quintard. Experimental and numerical study of two-phase flows in arrays of cylinders. *Chem. Eng. Sci.*, 102:335–345, October 2013.

[35] N. K. Karadimitriou, M. Musterd, P. J. Kleingeld, M. T. Kreutzer, S. M. Hassanizadeh, and V. Joekar-Niasar. On the fabrication of PDMS micromodels by rapid prototyping, and their use in two-phase flow studies. *Water Resour. Res.*, 49(4):2056–2067, April 2013.

[36] Qiulan Zhang, N K Karadimitriou, S M Hassanizadeh, P J Kleingeld, and a Imhof. Study of colloids transport during two-phase flow using a novel polydimethylsiloxane micro-model. *J. Colloid Interface Sci.*, 401:141–147, July 2013.

[37] Dhananjay Dendukuri, Daniel C Pregibon, Jesse Collins, T Alan Hatton, and Patrick S Doyle. Continuous-flow lithography for high-throughput microparticle synthesis. *Nat. Mater.*, 5(5):365–369, May 2006.

[38] Dhananjay Dendukuri, Shelley S Gu, Daniel C Pregibon, T Alan Hatton, and Patrick S Doyle. Stop-flow lithography in a microfluidic device. *Lab Chip*, 7(7):818–828, July 2007.

[39] Ki Wan Bong, Daniel C Pregibon, and Patrick S Doyle. Lock release lithography for 3D and composite microparticles. *Lab Chip*, 9(7):863–866, April 2009.

[40] Dhananjay Dendukuri, Priyadarshi Panda, Ramin Haghgooie, Ju Min Kim, T. Alan Hatton, and Patrick S. Doyle. Modeling of Oxygen-Inhibited Free

Radical Photopolymerization in a PDMS Microfluidic Device. *Macromolecules*, 41(22):8547–8556, November 2008.

[41] Rathi L Srinivas, Stephen D Johnson, and Patrick S Doyle. Oil-isolated hydrogel microstructures for sensitive bioassays on-chip. *Anal. Chem.*, 85(24):12099–12107, December 2013.

[42] Yong Chae Jung and Bharat Bhushan. Wetting behavior of water and oil droplets in three-phase interfaces for hydrophobicity/philicity and oleophobicity/philicity. *Langmuir*, 25(24):14165–14173, December 2009.

[43] C. C. Mattax and J. R. Kyte. Imbibition oil recovery from fractured water-drive reservoir. *Soc. Pet. Eng. J.*, 2(2):177–184, 1962.

[44] W. W. Owens and D. L. Archer. The effect of rock wettability on oil-water relative permeability relationships. *J. Pet. Technol.*, 23(7):873–878, 1971.

[45] R. A. Salathiel. Oil recovery by surface film drainage in mixed-wettability rocks. *J. Pet. Technol.*, 25(10):1216–1224, 1973.

[46] A. R. Kovscek, H. Wong, and C. J. Radke. A pore-level scenario for the development of mixed wettability in oil reservoirs. *AIChE J.*, 39(6):1072–1085, June 1993.

[47] Jean-Christophe Perrin and Sally Benson. An Experimental Study on the Influence of Sub-Core Scale Heterogeneities on CO2 Distribution in Reservoir Rocks. *Transp. Porous Media*, 82(1):93–109, June 2010.

[48] T. Austad, S. F. Shariatpanahi, S. Strand, C. J. J. Black, and K. J. Webb. Conditions for a Low-Salinity Enhanced Oil Recovery (EOR) Effect in Carbonate Oil Reservoirs. *Energy & Fuels*, 26(1):569–575, January 2012.

[49] Samuel C. M. Krevor, Ronny Pini, Lin Zuo, and Sally M. Benson. Relative permeability and trapping of CO 2 and water in sandstone rocks at reservoir conditions. *Water Resour. Res.*, February 2012.

[50] David Sinton. Energy: the microfluidic frontier. *Lab Chip*, 14(17):3127–34, September 2014.

[51] Can Ulas Hatiboglu and Tayfun Babadagli. Pore-scale studies of spontaneous imbibition into oil-saturated porous media. *Phys. Rev. E*, 77(6):066311, June 2008.

[52] Christophe Cottin, Hugues Bodiguel, and Annie Colin. Influence of wetting conditions on drainage in porous media: A microfluidic study. *Phys. Rev. E*, 84(2):026311, August 2011.

[53] Changyong Zhang, Mart Oostrom, Thomas W. Wietsma, Jay W. Grate, and Marvin G. Warner. Influence of Viscous and Capillary Forces on Immiscible Fluid Displacement: Pore-Scale Experimental Study in a Water-Wet Micromodel Demonstrating Viscous and Capillary Fingering. *Energy & Fuels*, 25(8):3493–3505, August 2011.

[54] Jerry Joseph, Naga Siva Kumar Gunda, and Sushanta K. Mitra. On-chip porous media: Porosity and permeability measurements. *Chem. Eng. Sci.*, 99:274–283, August 2013.

[55] Kai He, Liang Xu, Yuefeng Gao, Keith B. Neeves, Xiaolong Yin, Baojun Bai, Yinfa Ma, and Jonathan Smith. Validating Surfactant Performance in the Eagle Ford Shale: A Correlation between the Reservoir-on-a-Chip Approach and Enhanced Well Productivity. *Pap. SPE 169147*, pages 12–16, 2014.

[56] Charles A. Conn, Kun Ma, George J Hirasaki, and Sibani Lisa Biswal. Visualizing oil displacement with foam in a microfluidic device with permeability contrast. *Lab Chip*, 14(20):3968–3977, August 2014.

[57] Taha Moustafa Okasha, James Joseph Funk, and Hamid Nafeh Rashidi. Fifty Years of Wettability Measurements in the Arab-D Carbonate Reservoir. *SPE Middle East Oil Gas Show Conf.*, pages 1–10, 2007.

[58] L. E. Treiber and W. W. Owens. A laboratory evaluation of the wettability of fifty oil-producing reservoirs. *Society of Petroleum Engineers Journal*, 12(6):531–540, 1972.

[59] Meihua Jin, Jing Wang, Xi Yao, Mingyi Liao, Yong Zhao, and Lei Jiang. Underwater oil capture by a three-dimensional network architectured organosilane surface. *Adv. Mater.*, 23(25):2861–2864, July 2011.

[60] Arun K Kota, Gibum Kwon, Wonjae Choi, Joseph M Mabry, and Anish Tuteja. Hygro-responsive membranes for effective oil-water separation. *Nat. Commun.*, 3:1025, January 2012.

[61] Jay W. Grate, Marvin G. Warner, Jonathan W. Pittman, Karl J. Dehoff, Thomas W. Wietsma, Changyong Zhang, and Mart Oostrom. Silane modification of glass and silica surfaces to obtain equally oil-wet surfaces in glass-covered silicon micromodel applications. *Water Resour. Res.*, 49(8):4724–4729, August 2013.

[62] Bertrand Levaché, Ammar Azioune, Maurice Bourrel, Vincent Studer, and Denis Bartolo. Engineering the surface properties of microfluidic stickers. *Lab Chip*, 12(17):3028–3031, September 2012.

[63] Marc H Schneider, Hervé Willaime, Yvette Tran, Fadhel Rezgui, and Patrick Tabeling. Wettability patterning by UV-initiated graft polymerization of poly(acrylic acid) in closed microfluidic systems of complex geometry. *Anal. Chem.*, 82(21):8848–8855, 2010.

[64] Henrik Hillborg, Nikodem Tomczak, Attila Ola, Holger Scho, and G Julius Vancso. Nanoscale Hydrophobic Recovery : A Chemical Force Microscopy Study of UV / Ozone-Treated Cross-Linked Poly (dimethylsiloxane). *Langmuir*, 20(3):785–794, 2004.

[65] Attila Oláh, Henrik Hillborg, and G.Julius Vancso. Hydrophobic recovery of UV/ozone treated poly(dimethylsiloxane): adhesion studies by contact mechan-

ics and mechanism of surface modification. *Appl. Surf. Sci.*, 239(3-4):410–423, January 2005.

[66] H Yasuda, Ashok K Sharma, and Takeshi Yasuda. Effect of Orientation and Mobility of Polymer Molecules at Surfaces on Contact Angle and Its Hysteresis. *Polym. Phys. Ed.*, 19(9):1285–1291, 1981.

[67] Donald L Schmidt, Robert F Brady, Karen Lam, Dale C Schmidt, and Manoj K. Chaudhury. Contact Angle Hysteresis , Adhesion , and Marine Biofouling. *Langmuir*, 20(7):2830–2836, 2004.

[68] Jason C Yarbrough, Jason P Rolland, Joseph M Desimone, Maureen E Callow, John A Finlay, and James A Callow. Contact Angle Analysis , Surface Dynamics , and Biofouling Characteristics of Cross-Linkable , Random Perfluoropolyether-Based Graft Terpolymers. *Macromolecules*, 39(7):2521–2528, 2006.

[69] Seon Jeong Kim, Sang Jun Park, and Sun I Kim. Swelling behavior of interpenetrating polymer network hydrogels composed of poly (vinyl alcohol) and chitosan. *React. Funct. Polym.*, 55(1):53–59, 2003.

[70] Dae Kun Hwang, John Oakey, Mehmet Toner, Jeffrey A Arthur, Kristi S Anseth, Sunyoung Lee, Adam Zeiger, Krystyn J Van Vliet, and Patrick S Doyle. Stop-Flow Lithography for the Production of Shape-Evolving Degradable Microgel Particles. *J. Am. Chem. Soc.*, 131(12):4499–4504, 2009.

[71] Ying Diao, Kristen E Whaley, Matthew E Helgeson, Mahlet A Woldeyes, Patrick S Doyle, Allan S Myerson, T Alan Hatton, and Bernhardt L Trout. Gel-Induced Selective Crystallization of Polymorphs. *J. Am. Chem. Soc.*, 134(1):673–684, 2012.

[72] Hamed Amini, Elodie Sollier, Mahdokht Masaeli, Yu Xie, Baskar Ganapathysubramanian, Howard A Stone, and Dino Di Carlo. Engineering fluid flow using sequenced microstructures. *Nat. Commun.*, 4(May):1826, 2013.

[73] Scott S H Tsai, Jason S. Wexler, Jiandi Wan, and Howard A. Stone. Conformal coating of particles in microchannels by magnetic forcing. *Appl. Phys. Lett.*, 99(May):19–22, 2011.

[74] Myeongwoo Kang, Woohyun Park, Sangcheol Na, Sang-Min Paik, Hyunjae Lee, Jae Woo Park, Ho-Young Kim, and Noo Li Jeon. Capillarity Guided Patterning of Microliquids. *Small*, page DOI: 10.1002/smll.201403596, 2015.

[75] Jeongyun Kim, David Taylor, Nitin Agrawal, Han Wang, Hyunsoo Kim, Arum Han, Kaushal Rege, and Arul Jayaraman. A programmable microfluidic cell array for combinatorial drug screening. *Lab Chip*, 12(10):1813–1822, 2012.

[76] Amir M Foudeh, Tohid Fatanat Didar, Teodor Veres, and Maryam Tabrizian. Microfluidic designs and techniques using lab-on-a-chip devices for pathogen detection for point-of-care diagnostics. *Lab Chip*, 12(18):3249–3266, 2012.

[77] Jose L Garcia-Cordero and Sebastian J Maerkl. A 1024-sample serum analyzer chip for cancer diagnostics. *Lab Chip*, 14(15):2642–2650, 2014.

[78] Hyewon Lee, Rathi L Srinivas, Ankur Gupta, and Patrick S Doyle. Sensitive and multiplexed on-chip microrna profiling in oil-isolated hydrogel chambers. *Angew. Chem.*, 127(8):2507–2511, 2015.

[79] Burcu Gumuscu, Johan G Bomer, Albert van den Berg, and Jan CT Eijkel. Photopatterning of hydrogel microarrays in closed microchips. *Biomacromolecules*, 16(12):3802–3810, 2015.

[80] Seung Goo Lee, Hyundo Lee, Ankur Gupta, Sehoon Chang, and Patrick S Doyle. Site-selective in situ grown calcium carbonate micromodels with tunable geometry, porosity, and wettability. *Adv. Funct. Mater.*, 26:4896–4905, 2016.

[81] Bala Ambravaneswaran, Hariprasad J Subramani, Scott D Phillips, and Osman A Basaran. Dripping-jetting transitions in a dripping faucet. *Phys. Rev. Lett.*, 93(3):034501, 2004.

[82] Xingxun Li, Xianfeng Fan, and Stefano Brandani. Difference in pore contact angle and the contact angle measured on a flat surface and in an open space. *Chem. Eng. Sci.*, 117:137–145, 2014.

[83] David Quéré. Wetting and roughness. *Annu. Rev. Mater. Res.*, 38:71–99, 2008.

[84] 't Mannetje D. J. C. M. Eral, H. B. and J. M. Oh. Contact angle hysteresis: a review of fundamentals and applications. *Colloid Polym. Sci.*, 291(2):247–260, 2013.

[85] Pierre Guillot, Annie Colin, Andrew S Utada, and Armand Ajdari. Stability of a jet in confined pressure-driven biphasic flows at low reynolds numbers. *Phys. Rev. Lett.*, 99(10):104502, 2007.

[86] Pierre Guillot, Annie Colin, and Armand Ajdari. Stability of a jet in confined pressure-driven biphasic flows at low reynolds number in various geometries. *Phys. Rev. E*, 78(1):016307, 2008.

[87] Katherine J Humphry, Armand Ajdari, Alberto Fernández-Nieves, Howard A Stone, and David A Weitz. Suppression of instabilities in multiphase flow by geometric confinement. *PPhys. Rev. E*, 79(5):056310, 2009.

[88] Stefanie Utech, Radivoje Prodanovic, Angelo S Mao, Raluca Ostafe, David J Mooney, and David A Weitz. Microfluidic generation of monodisperse, structurally homogeneous alginate microgels for cell encapsulation and 3d cell culture. *Advanced healthcare materials*, 4(11):1628–1633, 2015.

[89] S Protiere, C Duprat, and HA Stone. Wetting on two parallel fibers: drop to column transitions. *Soft Matter*, 9(1):271–276, 2013.

[90] Alban Sauret, François Boulogne, David Cébron, Emilie Dressaire, and Howard A Stone. Wetting morphologies on an array of fibers of different radii. *Soft Matter*, 11(20):4034–4040, 2015.

[91] Scott SH Tsai, Jason S Wexler, Jiandi Wan, and Howard A Stone. Microfluidic ultralow interfacial tensiometry with magnetic particles. *Lab on a Chip*, 13(1):119–125, 2013.

[92] Byeong-Ui Moon, Navid Hakimi, Dae Kun Hwang, and Scott SH Tsai. Microfluidic conformal coating of non-spherical magnetic particles. *Biomicrofluidics*, 8(5):052103, 2014.

[93] Ali Afsharpoor, Kun Ma, Aurelien Duboin, Khalid Mateen, Stephane Jouenne, Philippe Cordelier, et al. Micro-scale experiment and cfd modeling of viscoelastic polymer; trapped oil displacement and deformation at the dead-end. In *SPE Improved Oil Recovery Symposium*. Society of Petroleum Engineers, 2014.

[94] Mathias Trojer, Michael L Szulczewski, and Ruben Juanes. Stabilizing fluid-fluid displacements in porous media through wettability alteration. *Physical Review Applied*, 3(5):054008, 2015.

[95] Michael Jung, Martin Brinkmann, Ralf Seemann, Thomas Hiller, Marta Sanchez de La Lama, and Stephan Herminghaus. Wettability controls slow immiscible displacement through local interfacial instabilities. *Physical Review Fluids*, 1(7):074202, 2016.

[96] Ansgar Huebner, Dan Bratton, Graeme Whyte, Min Yang, Chris Abell, Florian Hollfelder, et al. Static microdroplet arrays: a microfluidic device for droplet trapping, incubation and release for enzymatic and cell-based assays. *Lab on a Chip*, 9(5):692–698, 2009.

[97] Paul Abbyad, Rémi Dangla, Antigoni Alexandrou, and Charles N Baroud. Rails and anchors: guiding and trapping droplet microreactors in two dimensions. *Lab on a Chip*, 11(5):813–821, 2011.

[98] Meng Sun, Swastika S Bithi, and Siva A Vanapalli. Microfluidic static droplet arrays with tuneable gradients in material composition. *Lab on a Chip*, 11(23):3949–3952, 2011.

[99] Tak-Sing Wong, Sung Hoon Kang, Sindy KY Tang, Elizabeth J Smythe, Benjamin D Hatton, Alison Grinthal, and Joanna Aizenberg. Bioinspired self-repairing slippery surfaces with pressure-stable omniphobicity. *Nature*, 477(7365):443–447, 2011.

[100] A Lafuma and D Quéré. Slippery pre-suffused surfaces. *EPL (Europhysics Letters)*, 96(5):56001, 2011.

[101] J David Smith, Rajeev Dhiman, Sushant Anand, Ernesto Reza-Garduno, Robert E Cohen, Gareth H McKinley, and Kripa K Varanasi. Droplet mobility on lubricant-impregnated surfaces. *Soft Matter*, 9(6):1772–1780, 2013.

[102] Alexander K Epstein, Tak-Sing Wong, Rebecca A Belisle, Emily Marie Boggs, and Joanna Aizenberg. Liquid-infused structured surfaces with exceptional anti-biofouling performance. *Proceedings of the National Academy of Sciences*, 109(33):13182–13187, 2012.

[103] Jason S. Wexler, Abigail Grosskopf, Melissa Chow, Yuyang Fan, Ian Jacobi, and Howard A. Stone. Robust liquid-infused surfaces through patterned wettability. *Soft Matter*, 11(25):5023–5029, 2015.

[104] Jason S. Wexler, Ian Jacobi, and Howard A. Stone. Shear-driven failure of liquid-infused surfaces. *Physical Review Letters*, 114:168301, Apr 2015.

[105] I. Jacobi, J. S. Wexler, and H. A. Stone. Overflow cascades in liquid-infused substrates. *Physics of Fluids*, 27(8):082101, August 2015.

[106] Ying Liu, Jason S Wexler, Clarissa Schönecker, and Howard A Stone. Effect of viscosity ratio on the shear-driven failure of liquid-infused surfaces. *Physical Review Fluids*, 1(7):074003, 2016.

[107] Hyundo Lee, Ankur Gupta, T Alan Hatton, and Patrick S Doyle. Creating isolated liquid compartments using photopatterned obstacles in microfluidics. *Physical Review Applied*, 7(4):044013, 2017.

[108] R Patel and H Benkreira. Gravure roll coating of newtonian liquids. *Chemical engineering science*, 46(3):751–756, 1991.

[109] Changkwon Chung and Satish Kumar. Emptying of viscoelastic liquids from model gravure cells. *Journal of Non-Newtonian Fluid Mechanics*, 221:1–8, 2015.

[110] Chung-Hsuan Huang, Marcio S Carvalho, and Satish Kumar. Stretching liquid bridges with moving contact lines: comparison of liquid-transfer predictions and experiments. *Soft matter*, 12(36):7457–7469, 2016.

[111] Dhananjay Dendukuri, Daniel C Pregibon, Jesse Collins, T Alan Hatton, and Patrick S Doyle. Continuous-flow lithography for high-throughput microparticle synthesis. *Nature Materials*, 5(5):365–369, 2006.

[112] Dhananjay Dendukuri, Shelley S Gu, Daniel C Pregibon, T Alan Hatton, and Patrick S Doyle. Stop-flow lithography in a microfluidic device. *Lab on a Chip*, 7(7):818–828, 2007.

[113] Hyundo Lee, Seung Goo Lee, and Patrick S Doyle. Photopatterned oil-reservoir micromodels with tailored wetting properties. *Lab Chip*, 15(14):3047–3055, 2015.

[114] Ki Wan Bong, Ki Tae Bong, Daniel C Pregibon, and Patrick S Doyle. Hydrodynamic focusing lithography. *Angewandte Chemie International Edition*, 49(1):87–90, 2010.

[115] Stephen C Chapin, David C Appleyard, Daniel C Pregibon, and Patrick S Doyle. Rapid microrna profiling on encoded gel microparticles. *Angewandte Chemie International Edition*, 50(10):2289–2293, 2011.

[116] Weifeng Huang, Qiusheng Liu, and Yong Li. Capillary filling flows inside patterned-surface microchannels. *Chemical engineering & technology*, 29(6):716–723, 2006.

[117] Michiel Musterd, Volkert van Steijn, Chris R Kleijn, and Michiel T Kreutzer. Calculating the volume of elongated bubbles and droplets in microchannels from a top view image. *RSC Advances*, 5(21):16042–16049, 2015.

[118] Howard A Stone. Dynamics of drop deformation and breakup in viscous fluids. *Annual Review of Fluid Mechanics*, 26(1):65–102, 1994.

[119] Charles D Eggleton, Tse-Min Tsai, and Kathleen J Stebe. Tip streaming from a drop in the presence of surfactants. *Physical Review Letters*, 87(4):048302, 2001.

[120] HA Stone and LG Leal. The effects of surfactants on drop deformation and breakup. *Journal of Fluid Mechanics*, 220:161–186, 1990.

[121] Shelley Lynn Anna. Droplets and bubbles in microfluidic devices. *Annual Review of Fluid Mechanics*, 48:285–309, 2016.

[122] Gaelle C Le Goff, Jiseok Lee, Ankur Gupta, William Adam Hill, and Patrick S Doyle. High-throughput contact flow lithography. *Adv. Sci.*, 2(10), 2015.

[123] Luis Cueto-Felgueroso and Ruben Juanes. Macroscopic phase-field model of partial wetting: bubbles in a capillary tube. *Physical review letters*, 108(14):144502, 2012.

[124] Luis Cueto-Felgueroso and Ruben Juanes. A phase-field model of two-phase hele-shaw flow. *Journal of Fluid Mechanics*, 758:522–552, 2014.

[125] Wen Song, Thomas W. de Haas, Hossein Fadaei, and David Sinton. Chip-off-the-old-rock: The study of reservoir-relevant geological processes with real-rock micromodels. *Lab Chip*, 14:4382–4390, September 2014.

[126] Mark L Porter, Joaquín Jiménez-Martínez, Ricardo Martinez, Quinn McCulloch, J William Carey, and Hari S Viswanathan. Geo-material microfluidics at reservoir conditions for subsurface energy resource applications. *Lab Chip*, 15(20):4044–4053, 2015.

[127] Kirk M Bartko, Hisham A Nasr-El-Din, Zillur Rahim, Ghaithan A Al-Muntasheri, et al. Acid fracturing of a gas carbonate reservoir: the impact of acid type and lithology on fracture half length and width. In *SPE Annual Technical Conference and Exhibition*. Society of Petroleum Engineers, 2003.

[128] Dave L Cantrell and Royal M Hagerty. Microporosity in arab formation carbonates, saudi arabia. *GeoArabia*, 4(2):129–154, 1999.

[129] A Hetal Heuer, DJ Fink, et al. Innovative materials processing strategies: a biomimetic approach. *Science*, 255(5048):1098, 1992.

[130] Laurie B Gower. Biomimetic model systems for investigating the amorphous precursor pathway and its role in biomineralization. *Chemical reviews*, 108(11):4551–4627, 2008.

[131] Steve Weiner and Lia Addadi. Crystallization pathways in biomineralization. *Annual review of materials research*, 41:21–40, 2011.

[132] Emily Asenath-Smith, Hanying Li, Ellen C Keene, Zhi Wei Seh, and Lara A Estroff. Crystal growth of calcium carbonate in hydrogels as a model of biomineralization. *Adv. Funct. Mater.*, 22(14):2891–2914, 2012.

[133] Giuseppe Falini, Shira Albeck, Steve Weiner, and Lia Addadi. Control of aragonite or calcite polymorphism by mollusk shell macromolecules. *Science*, 271(5245):67, 1996.

[134] Joanna Aizenberg, Andrew J Black, and George M Whitesides. Control of crystal nucleation by patterned self-assembled monolayers. *Nature*, 398(6727):495–498, 1999.

[135] Joanna Aizenberg, David A Muller, John L Grazul, and DR Hamann. Direct fabrication of large micropatterned single crystals. *Science*, 299(5610):1205–1208, 2003.

[136] Xurong Xu, Joong Tark Han, and Kilwon Cho. Formation of amorphous calcium carbonate thin films and their role in biomineralization. *Chem. Mater.*, 16(9):1740–1746, 2004.

[137] Joong Tark Han, Xurong Xu, Do Hwan Kim, and Kilwon Cho. Mosaic, single-crystal caco3 thin films fabricated on modified polymer templates. *Adv. Funct. Mater.*, 15(3):475–480, 2005.

[138] Hanying Li, Huolin L Xin, David A Muller, and Lara A Estroff. Visualizing the 3d internal structure of calcite single crystals grown in agarose hydrogels. *Science*, 326(5957):1244–1247, 2009.

[139] Alexander Finnemore, Pedro Cunha, Tamaryn Shean, Silvia Vignolini, Stefan Guldin, Michelle Oyen, and Ullrich Steiner. Biomimetic layer-by-layer assembly of artificial nacre. *Nat. Commun.*, 3:966, 2012.

[140] Filipe Natalio, Tomas P Corrales, Martin Panthöfer, Dieter Schollmeyer, Ingo Lieberwirth, Werner EG Müller, Michael Kappl, Hans-Jürgen Butt, and Wolfgang Tremel. Flexible minerals: self-assembled calcite spicules with extreme bending strength. *Science*, 339(6125):1298–1302, 2013.

[141] Kyubock Lee, Wolfgang Wagermaier, Admir Masic, Krishna P Kommareddy, Mathieu Bennet, Inderchand Manjubala, Seung-Woo Lee, Seung B Park, Helmut Cölfen, and Peter Fratzl. Self-assembly of amorphous calcium carbonate microlens arrays. *Nat. Commun.*, 3:725, 2012.

[142] Olaf Grassmann, Gerd Müller, and Peer Löbmann. Organic- inorganic hybrid structure of calcite crystalline assemblies grown in a gelatin hydrogel matrix: relevance to biomineralization. *Chem. Mater.*, 14(11):4530–4535, 2002.

[143] Yasushi Kitano. The behavior of various inorganic ions in the separation of calcium carbonate from a bicarbonate solution. *Bull. Chem. Soc. Jpn*, 35(12):1973–1980, 1962.

[144] Alexandre M Tartakovsky, G Redden, Peter C Lichtner, Timothy D Scheibe, and Paul Meakin. Mixing-induced precipitation: Experimental study and multiscale numerical analysis. *Water Resour. Res.*, 44(6), 2008.

[145] Guy E Katz, Brian Berkowitz, Alberto Guadagnini, and Maarten W Saaltink. Experimental and modeling investigation of multicomponent reactive transport in porous media. *J. Contam. Hydrol.*, 120:27–44, 2011.

[146] Rajveer Singh, Hongkyu Yoon, Robert A Sanford, Lynn Katz, Bruce W Fouke, and Charles J Werth. Metabolism-induced caco3 biomineralization during reactive transport in a micromodel: Implications for porosity alteration. *Environ. Sci. Tech.*, 49(20):12094–12104, 2015.

[147] PA Raj, M Johnsson, Michael J Levine, and GH Nancollas. Salivary statherin. dependence on sequence, charge, hydrogen bonding potency, and helical conformation for adsorption to hydroxyapatite and inhibition of mineralization. *J. Biol. Chem.*, 267(9):5968–5976, 1992.

[148] RH Clark, AA Campbell, LA Klumb, CJ Long, and PS Stayton. Protein electrostatic surface distribution can determine whether calcium oxalate crystal growth is promoted or inhibited. *Calcif. Tissue Int.*, 64(6):516–521, 1999.

[149] M Kawashita, M Nakao, M Minoda, H-M Kim, T Beppu, T Miyamoto, T Kokubo, and T Nakamura. Apatite-forming ability of carboxyl group-containing polymer gels in a simulated body fluid. *Biomaterials*, 24(14):2477–2484, 2003.

[150] GH Nancollas and MM Reddy. The crystallization of calcium carbonate. ii. calcite growth mechanism. *J. Colloid Interface Sci.*, 37(4):824–830, 1971.

[151] David J Beebe, Glennys A Mensing, and Glenn M Walker. Physics and applications of microfluidics in biology. *Annu. Rev. Biomed. Eng.*, 4(1):261–286, 2002.

[152] Xuetao Shi, Roberto Rosa, and Andrea Lazzeri. On the coating of precipitated calcium carbonate with stearic acid in aqueous medium. *Langmuir*, 26(11):8474–8482, 2010.

[153] Richa Shukla, Pathegama Ranjith, Asadul Haque, and Xavier Choi. A review of studies on co 2 sequestration and caprock integrity. *Fuel*, 89(10):2651–2664, 2010.

[154] Ibrahim M Banat, Andrea Franzetti, Isabella Gandolfi, Giuseppina Bestetti, Maria G Martinotti, Letizia Fracchia, Thomas J Smyth, and Roger Marchant. Microbial biosurfactants production, applications and future potential. *Applied microbiology and biotechnology*, 87(2):427–444, 2010.

[155] Kiyoshi Sawada. The mechanisms of crystallization and transformation of calcium carbonates. *Pure and Applied Chemistry*, 69(5):921–928, 1997.

[156] Nobuyoshi Koga, YUZOU Nakagoe, and Haruhiko Tanaka. Crystallization of amorphous calcium carbonate. *Thermochimica Acta*, 318(1):239–244, 1998.

[157] Raymond SK Lam, John M Charnock, Alistair Lennie, and Fiona C Meldrum. Synthesis-dependant structural variations in amorphous calcium carbonate. *CrystEngComm*, 9(12):1226–1236, 2007.

[158] Jie Xu, Chao Yan, Fangfu Zhang, Hiromi Konishi, Huifang Xu, and H Henry Teng. Testing the cation-hydration effect on the crystallization of ca–mg–co3 systems. *Proceedings of the National Academy of Sciences*, 110(44):17750–17755, 2013.

[159] David C Green, Rebecca Boston, Stefan Glatzel, Martin R Lees, Stuart C Wimbush, Jason Potticary, Wataru Ogasawara, and Simon R Hall. On the mechanism of cuprate crystal growth: The role of mixed metal carbonates. *Advanced Functional Materials*, 25(29):4700–4707, 2015.

[160] Bettina Purgstaller, Vasileios Mavromatis, Adrian Immenhauser, and Martin Dietzel. Transformation of mg-bearing amorphous calcium carbonate to mg-

calcite–in situ monitoring. *Geochimica et Cosmochimica Acta*, 174:180–195, 2016.

[161] Kang Rae Cho, Yi-Yeoun Kim, Pengcheng Yang, Wei Cai, Haihua Pan, Alexander N Kulak, Jolene L Lau, Prashant Kulshreshtha, Steven P Armes, Fiona C Meldrum, et al. Direct observation of mineral–organic composite formation reveals occlusion mechanism. *Nature communications*, 7:10187, 2016.

[162] Nicholas A Meanwell. Improving drug candidates by design: a focus on physicochemical properties as a means of improving compound disposition and safety. *âĂŐChem. Res. Toxicol.*, 24(9):1420–1456, 2011.

[163] Christopher A Lipinski. Drug-like properties and the causes of poor solubility and poor permeability. *J Pharmacol Toxicol Methods*, 44(1):235–249, 2000.

[164] N Jagadeesh Babu and Ashwini Nangia. Solubility advantage of amorphous drugs and pharmaceutical cocrystals. *Crystal Growth & Design*, 11(7):2662–2679, 2011.

[165] JU Junghanns and Rainer H Müller. Nanocrystal technology, drug delivery and clinical applications. *Int. J. Nanomedicine*, 3(3):295–309, 2008.

[166] Ranjita Shegokar and Rainer H Müller. Nanocrystals: industrially feasible multifunctional formulation technology for poorly soluble actives. *Int. J. Pharm.*, 399(1):129–139, 2010.

[167] Prakash Khadka, Jieun Ro, Hyeongmin Kim, Iksoo Kim, Jeong Tae Kim, Hyunil Kim, Jae Min Cho, Gyiae Yun, and Jaehwi Lee. Pharmaceutical particle technologies: an approach to improve drug solubility, dissolution and bioavailability. *Asian J. Pharmacol.*, 9(6):304–316, 2014.

[168] Panayiotis P Constantinides. Lipid microemulsions for improving drug dissolution and oral absorption: physical and biopharmaceutical aspects. *Pharm. Res.*, 12(11):1561–1572, 1995.

[169] Tatyana Gershanik and Simon Benita. Self-dispersing lipid formulations for improving oral absorption of lipophilic drugs. *Eur. J. Pharm. Biopharm.*, 50(1):179–188, 2000.

[170] Bo Tang, Gang Cheng, Jian-Chun Gu, and Cai-Hong Xu. Development of solid self-emulsifying drug delivery systems: preparation techniques and dosage forms. *Drug Discov. Today.*, 13(13):606–612, 2008.

[171] Jie Chen, Bipul Sarma, James MB Evans, and Allan S Myerson. Pharmaceutical crystallization. *Crystal Growth & Design*, 11(4):887–895, 2011.

[172] Aliasgar Shahiwala. Formulation approaches in enhancement of patient compliance to oral drug therapy. *Expert Opin. Drug Deliv.*, 8(11):1521–1529, 2011.

[173] Lei Gao, Guiyang Liu, Jianli Ma, Xiaoqing Wang, Liang Zhou, and Xiang Li. Drug nanocrystals: in vivo performances. *J. Control. Release*, 160(3):418–430, 2012.

[174] Jan P Möschwitzer. Drug nanocrystals in the commercial pharmaceutical development process. *Int. J. Pharm.*, 453(1):142–156, 2013.

[175] Biswadip Sinha, Rainer H Müller, and Jan P Möschwitzer. Bottom-up approaches for preparing drug nanocrystals: formulations and factors affecting particle size. *Int. J. Pharm.*, 453(1):126–141, 2013.

[176] Todd R Hoare and Daniel S Kohane. Hydrogels in drug delivery: progress and challenges. *Polymer*, 49(8):1993–2007, 2008.

[177] Ying Diao, Matthew E Helgeson, Allan S Myerson, T Alan Hatton, Patrick S Doyle, and Bernhardt L Trout. Controlled nucleation from solution using polymer microgels. *J. Am. Chem. Soc.*, 133(11):3756–3759, 2011.

[178] Ying Diao, Matthew E Helgeson, Zeina A Siam, Patrick S Doyle, Allan S Myerson, T Alan Hatton, and Bernhardt L Trout. Nucleation under soft confinement:

Role of polymer–solute interactions. *Crystal Growth & Design*, 12(1):508–517, 2011.

[179] Huseyin Burak Eral, Vilmali Lopez-Mejias, Marcus O' Mahony, Bernhard L Trout, Allan S Myerson, and Patrick S Doyle. Biocompatible alginate microgel particles as heteronucleants and encapsulating vehicles for hydrophilic and hydrophobic drugs. *Crystal Growth & Design*, 14(4):2073–2082, 2014.

[180] Huseyin Burak Eral, Marcus O' Mahony, Robert Shaw, Bernhardt L Trout, Allan S Myerson, and Patrick S Doyle. Composite hydrogels laden with crystalline active pharmaceutical ingredients of controlled size and loading. *Chem. Mater.*, 26(21):6213–6220, 2014.

[181] Abu Zayed Md Badruddoza, P Douglas Godfrin, Allan S Myerson, Bernhardt L Trout, and Patrick S Doyle. Core–shell composite hydrogels for controlled nanocrystal formation and release of hydrophobic active pharmaceutical ingredients. *Adv. Healthcare Mater.*, 5(15):1960–1968, 2016.

[182] Steven Shimizu, Kumar Varoon Agrawal, Marcus O' Mahony, Lee W Drahushuk, Neha Manohar, Allan S Myerson, and Michael S Strano. Understanding and analyzing freezing-point transitions of confined fluids within nanopores. *Langmuir*, 31(37):10113–10118, 2015.

[183] LM Dwyer, VK Michaelis, M O' Mahony, RG Griffin, and AS Myerson. Confined crystallization of fenofibrate in nanoporous silica. *CrystEngComm*, 17(41):7922–7929, 2015.